UNIVERSITY OF GENOVA

POLYTECHNIC SCHOOL

DITEN- Electrical, Electronics and Telecommunication
Engineering and Naval Architecture Department

Ph.D. in Sciences and Technologies for Electrical Engineering and
Complex Systems for Mobility

Sensorless Passive Control Algorithms for Medium to High Power Synchronous Motor Drives

Supervisors: Prof. Mario Marchesoni
Prof. Mauro Carpita

Author: Massimiliano Passalacqua

To my sister Francesca

Acknowledgements

I would like to sincerely thank my supervisor, Prof. Mario Marchesoni, and Prof. Luis Vaccaro for the teachings they gave me during my Ph.D. and for the enthusiasm with which they welcome my ideas.

I would like equally to thanks my supervisor, Prof. Mauro Carpita, and all the IESE Team of HEIG-VD for the technical support and, especially, for the hospitality they showed me during my stay in Yverdon-les-Bains.

I finally thank Phase Motion Control S.p.A., Physis New Energy Technology S.r.l. and Nidec ASI S.p.A. for the support.

Abstract

This study is focused on the definition of sensorless algorithms for Surface-Mounted Permanent Magnet Synchronous Motors (SM-PMSM) and Electrically Excited Synchronous Motors (EESM). Even if these types of motors are rather different from a constructive point of view, they have some common issues regarding sensorless drives. Indeed, SM-PMSMs, which are usually used for low-medium power applications, have a low rotor anisotropy, therefore it is complicated to use sensorless active methods (which are based on high-frequency voltage injection), due to the low signal to noise ratio. On the other hand, active methods on high-power EESM have the drawback of high torque ripple.

For these reasons, both for SM-PMSM and EESM, it is interesting to define and use sensorless passive algorithms (i.e., based on observers and estimators). The drawback of such algorithms is that their performance deteriorates significantly in the low-speed region.

The aim of this thesis is to define a robust sensorless passive algorithm that could work in a wide speed region and that could start the motor from standstill even with a high load torque. The initial objective of the work is to find, among the various algorithms proposed in the technical literature, the most promising one. For this purpose, four different algorithms are selected. They are chosen considering the most recent articles presented in the technical literature on high reputable journals. Since many improvements are proposed in the literature for the different algorithms, the most recent ones are candidates for being the ones with higher performance.

Even if the experimental tests of the four different algorithms are shown in the literature, it is difficult to evaluate a priori which offers the best performance. As a matter of facts, for each algorithm different tests are carried out (e.g., different speed and torque profiles). In addition to that, motor sizing and features are different. Moreover, the test bench characteristics can significantly affect sensorless performance. As an example, inverter features and non-linearities (e.g., switching frequency, dead times, parasitic capacitance) and current measures (e.g., noise, linearity, bias) play a key role in the estimation of rotor position.

The added value of this thesis is to perform a fair comparison of the four algorithms, performing the same tests with the same test bench.

Additional tests are performed on the most performing algorithm. Even if this sensorless technique is already proposed in the technical literature, a methodology for observer gain tuning is not shown, which is proposed, instead, in this thesis.

Moreover, the algorithm is enhanced by adding a novel management of direct axis current, which ensures the stability during fast transient from medium-high speed to low speed.

The algorithm is tested with different test benches in order to verify the control effectiveness in various operating conditions.

As a matter of facts, it is tested at first in the University of Genoa PETRA Lab on two different test benches.

The first test bench is composed of two coupled motors, in which the braking motor could realize different torque profiles (linear torque, quadratic torque and constant torque), whereas in the second test bench the motor is coupled with an air compressor, which is a demanding load since high and irregular torque is applied at standstill.

After the test at the University of Genoa, the algorithm is implemented in Phase Motion Control and Physis drive and tested on a six-meter diameter fan.

Regarding the EESMs, for these type of motor is necessary to estimate the stator flux amplitude and angle. Indeed, the stator angle is usually used to perform the Park transformations in the FOC scheme and the stator flux amplitude is used to control the excitation current. In this study, the RFO is adapted for estimating the stator flux of an EESM.

Regarding the control for EESM, it is tested on a simulative model for high-power motors provided by NIDEC ASI and tested on a small-scale test bench at the University of Genoa.

Summary

Figure Index

Table Index

1 Introduction

In last decades, Permanent Magnet Synchronous Motors (PMSMs) have achieved an increasing role. Indeed, compared to induction motors, they have a high efficiency, high power density, high torque to inertia ratio, they require low maintenance and they are characterized by high reliability.

One of the main drawbacks of PMSM is that rotor position measure is necessary to realize a proper control. As a matter of facts, Field-Oriented-Control (FOC) is usually exploited and the position information is needed to realize Park transformations.

In PMSMs the absolute rotor angle is required. For this reason, resolvers, absolute encoders or effect Hall probes are usually used. Nevertheless, the use of such transducers implies several issues in terms of cost, sizing, reliability and noise immunity.

To solve these problems, a lot of studies focus on rotor position estimation. These techniques are known as sensorless algorithm and can be mainly divided in two categories[1]: active methods and passive methods. Both active methods and passive methods can be used, appropriately adapted, for Electrically-Excited Synchronous Motors (EESMs), as it will be shown in Section 1.3.

1.1 Sensorless active methods for PMSM

Sensorless active methods exploits rotor anisotropy to estimate the rotor position [2-33]. They are defined as "active" because they inject high frequency voltage in order to evaluate the rotor angle. Indeed, injecting a high frequency v_{dh} as shown in equation (1.1), one obtains the high frequency currents i_{dh} and i_{qh} shown in equation (1.2) and where I_p, I_n and $\Delta\theta$ are defined in equations (1.3) [34].

$$\begin{bmatrix} v_{dh} \\ v_{qh} \end{bmatrix} = V_c \begin{bmatrix} \cos\alpha \\ 0 \end{bmatrix}, \ \alpha = \omega_c t + \varphi \tag{1.1}$$

$$\begin{bmatrix} i_{dh} \\ i_{qh} \end{bmatrix} = \begin{bmatrix} I_p + I_n \cos(2\Delta\theta) \\ I_n \sin(2\Delta\theta) \end{bmatrix} \tag{1.2}$$

$$I_p = \frac{V_c}{\omega_c L_p}, \ I_n = \frac{V_c}{\omega_c L_n}, \ \Delta\theta = \theta_r - \theta_r^e \tag{1.3}$$

$$L_p = \frac{L_{dh} L_{qh}}{L_{sa}}, \ L_n = \frac{L_{dh} L_{qh}}{L_{sd}} \tag{1.4}$$

$$L_{sa} = \frac{L_{qh} + L_{dh}}{2}, \ L_{sd} = \frac{L_{qh} - L_{dh}}{2} \tag{1.5}$$

where V_c and α are the amplitude and the phase angle of the injected carrier voltage signal; ω_c and φ are the angular speed and the initial phase angle of the injected carrier voltage signal, θ_r and θ_r^e are the real and estimated rotor positions, respectively. $\Delta\theta$ is the estimated rotor position error. L_{dh} and L_{qh} are the incremental d- and q-axis inductances, respectively, which are related to L_p, L_n, L_{sa}, L_{sd} as shown in equations (1.4) and (1.5). From (1.2), it is clearly shown that the carrier current response is amplitude modulated by the rotor position information. The q-axis carrier current i_{qh} response is usually used to extract the rotor position information. Indeed, a proper control can be exploited to obtain $i_{qh}=0$, i.e., $\Delta\theta=0$ and From equations (1.3) , (1.4) and (1.5) it is easy to observe that the lower is the difference $L_{qh}-L_{dh}$ (i.e., low rotor anisotropy), the lower is I_n . For this reason this methods are particularly suitable for Reluctance Synchronous Motors (RSMs) and Interior-Mounted Permanent Magnet Synchronous Motors (IPMSMs), which are characterized by a high rotor anisotropy. On the contrary it is difficult to use active methods for Surface-Mounted Permanent Magnet Synchronous Motors (SPMSMs), since they are characterized by a low anisotropy and in order to have a sufficient signal-to-noise ratio it is necessary to inject a v_{dh} with a high amplitude.

The advantage of active methods is that they can estimate the rotor position even at very low speed or at standstill. However, the high-frequency injection is connected to load acoustic noise, additional losses and torque ripple.

1.2 Sensorless passive methods for PMSM

Sensorless passive methods, differently from active methods, do not need the injection of additional signal. They are based on observers and estimators of Back-Electromotive Force (BEMF) or Rotor Flux (RF) and they are known as model-based sensorless controls [35-60].

Since these methods do not require signal injection, they do not have the drawbacks of active methods. However, since the BEMF tends toward zero while speed approaches zero, their performance deteriorate significantly in the low speed region.

Some disturbance observers were developed for this purpose, both in the stationary reference frame [38], and in the rotating reference frame [36, 41]. Recently, a new type of disturbance observer called active disturbance rejection control (ADRC) was applied to sensorless Field-Oriented Control (FOC) schemes [61, 62]. Back-EMF estimation in stationary reference frame was also obtained in [63-66] by means of a reduced-order extended Kalman filter, which was then implemented on a FPGA-based sensorless control [67]. Another approach is represented by sliding-mode observers (SMO)[46, 68-78], first introduced by Yan et al. in [72]. A SMO is characterized by a high robustness to parameter variations, but it suffers from chattering problems due to the sliding-mode switching function (i.e., the signum function). This problem can be partially solved by replacing the signum function with a saturation function [73], a sigmoid function [74, 75], a supertwisting function [76], or by using a complex-coefficient filter [77]. Another class of passive methods includes flux observers that estimate the rotor flux angle directly. This is an advantageous approach at low-speed compared to back-EMF estimation, since the rotor flux does not vanish at standstill. Flux estimation was performed in the rotating reference frame in [79]. A nonlinear flux observer in stationary reference frame was proposed by Ortega et al. in [80], and its performance was evaluated experimentally in [49]. Bobtsov et al. introduced an observer in which a high-pass filter was applied to a linear regression form to eliminate the effect of unknown constants [81]. Choi et al. improved it adding a feedback loop to overcome the PM flux linkage constant uncertainty, obtaining a robust adaptive sensorless algorithm [50] which was then tested in several experimental conditions and with many different loads in [53-55]. They also developed another regression-based algorithm for IPMSMs in [82], that can be adapted for use with SPMSMs.

Since the use of active methods and passive methods is complementary, often active methods are used to start the motor and to work in the low speed region and the control switches to a passive method in the medium and high speed region [83-86]. If high-frequency injection could not be exploited, an option could be starting with an open-loop rotating current vector before switching to a model-based observer [87-90].

Please note that since the objective of this thesis are the passive methods, the mathematical description is carried out in detail in Section 2, whereas the mathematical description of active methods is analysed briefly in the introduction (Section 1.1).

1.3 Sensorless for EESM

Electrically-Excited Synchronous Motors (EESMs) are usually used for high-power applications, around few or tens of MW. In these applications, of course the additional cost of an encoder is negligible on the drive total cost. This is the main reason why only few studies were carried in the technical literature regarding sensorless on EESM [91-98].

However, in some applications, sensorless is a requirement even for high-power EESM. As a matter of facts, the use of an encoder reduces the drive reliability, thus sensorless is required in high-reliable drives.

Even if SPMSM and EESM are significantly different from a constructive point of view, they have some common issues regarding sensorless applications. Indeed, active methods are difficult to use in SPMSMs since they are characterized by a reduced anisotropy. As a consequence, high-frequency voltage with high amplitude should be injected in order to have a sufficient signal-to-noise ratio, with obvious problems in terms of loud acoustic noise and additional losses.

On the other hand, since high-power EESM drive are characterized by low switching frequency, the high-frequency voltage injection (which is however lower than the switching frequency) leads often to unsustainable torque ripple.

Even if for different reasons, SPMSM and EESM have in common the necessity of exploiting robust sensorless algorithms based on passive methods. Several algorithms proposed in the technical literature are based on high frequency injection [91-93, 97] and therefore are not suitable for high-power applications. Other algorithms analyse passive methods, however, their effectiveness was not evaluated with experimental results [44, 94, 95, 98].

1.4 Aim of the thesis

The aim of this thesis is to define a robust sensorless passive algorithm for SPMSM. As aforementioned, defining a passive method for surface-mounted PMSM is fundamental since the low rotor anisotropy causes difficulties to utilize active methods and, moreover, the loud acoustic noise is not acceptable in several applications.

The initial objective of the work was to find, among the many algorithms in the technical literature, the most promising one. For this purpose, four different algorithms were selected [50, 62, 77, 82]. They were chosen considering the most recent articles presented in the technical literature on high reputable journals. Since many improvements were proposed in the literature for the different algorithms, the most recent ones are candidates for being the ones with higher performance.

Moreover, algorithms which follow different approaches were considered. In particular, the following algorithms were evaluated:

- The new type of disturbance observer called "Enhanced Linear Active Disturbance Rejection Controller" (ELADRC), which works in the d-q reference frame and that was published in IEEE Transaction on Power Electronics in 2020 [62]. This algorithm will be referred as ELADRC.
- The sliding mode observer (SMO) with the adoption of a "Frequency-Adaptive Complex-Coefficient Filter" (FACCF), which work in the stationary reference frame and that was published in IEEE Transactions on Industry Applications in 2020 [77]. This algorithm will be referred as SMO-FACCF.
- The Rotor Flux Observer (RFO) based on the gradient descent method and working in the stationary reference frame, which was presented in IEEE Transactions on Power Electronics in 2017 [50]. This algorithm will be referred as RFO.
- The Rotor Flux Observer, similar to the RFO but which can work both for SPMSM and IPMSM, presented in IEEE Transactions of Power Electronics in 2019 [82]. This algorithm will be referred as Extended-RFO.

1.5 Novelty and contributions

Even if the experimental tests of the four different algorithms were shown in the literature, it is difficult to evaluate a priori which offers the best performance. As a matter of facts, for each algorithm different tests were carried out (e.g., different speed and torque profiles). In addition to that, motor sizing and feature were different. Moreover, the test bench characteristics can significantly affect sensorless performance. As an example, inverter features and non-linearities (e.g., switching frequency, dead times, parasitic capacitance) and current measures (e.g., noise, linearity, bias) play a key role in the estimation of rotor position.

The added value of this thesis is to perform a fair comparison of the four algorithms, performing the same tests with the same test bench.

As it will be shown in the thesis, the RFO algorithm was the most promising one. Therefore additional tests were performed on this algorithm. Even if this sensorless technique was proposed in [50, 81], none of these papers show a methodology for observer gain tuning, which is proposed in this thesis.

Moreover, the RFO algorithm was enhanced adding a novel management of direct axis current, which ensure the stability during fast transient from medium-high speed to low speed.

Regarding the EESMs, for these type of motor is necessary to estimate the stator flux amplitude and angle. Indeed, the stator angle is usually used to perform the Park transformations in the FOC scheme and the stator flux amplitude is used to control the excitation current. In this study, the RFO was adapted for estimating the stator flux of a EESM.

1.6 Methodology and procedure

All these tests were performed implementing the control in the platform for Rapid Control Prototyping (RCP) Dspace MicroLabBox. The RFO was then implemented in an industrial inverter developed by Phase Motion Control S.p.A (from this point referred as PMC). Finally the algorithm was tested in an industrial application were the PMC inverter supplied a PMSM designed and produced by Physis New Energy Technology S.r.l. (from this point referred as PNET). The motor was coupled with a 6 meter diameter fan.

The algorithm for EESM was tested on a MATLAB/Simulink model of a 14 MW machine. The model was provided by Nidec ASI S.p.A (from this point referred as Nidec ASI). It was then tested on a small-scale prototype in the PETRA Lab, in the University of Genoa.

2 Sensorless passive algorithms for SPMSM

2.1 PMSM model

Before describing the structure and equations of each algorithm, the PMSM model is introduced both in stationary α-β reference frame and synchronously rotating d-q reference frame, according to [36, 82].

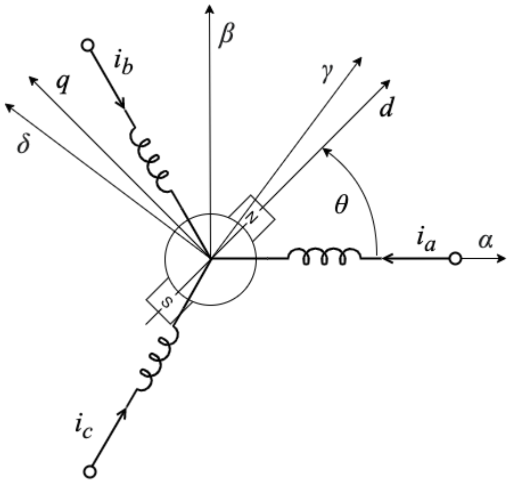

Fig. 1 PMSM scheme

A schematic diagram of a PMSM is shown in Fig. 1, where α-β axes indicate the stationary reference frame and d-q axes indicate the synchronous reference frame. Also, an estimated synchronous γ-δ frame is shown, as it is used in the derivation of the ELADRC observer.

The electrical equations of a generic PMSM in the stationary frame can be expressed as in equation (2.1):

$$\begin{bmatrix} v_\alpha \\ v_\beta \end{bmatrix} = R_s \begin{bmatrix} i_\alpha \\ i_\beta \end{bmatrix} + p\left(\begin{bmatrix} L_s + \frac{\Delta L}{2}\cos 2\theta & \frac{\Delta L}{2}\sin 2\theta \\ \frac{\Delta L}{2}\sin 2\theta & L_s - \frac{\Delta L}{2}\cos 2\theta \end{bmatrix}\begin{bmatrix} i_\alpha \\ i_\beta \end{bmatrix}\right) + \begin{bmatrix} e_\alpha \\ e_\beta \end{bmatrix} \tag{2.1}$$

where p is the differential operator, $\theta \in [0, 2\pi)$ is the rotor flux angle, $v_{\alpha\beta} = [v_\alpha, v_\beta]^T$ are the stator voltages, $i_{\alpha\beta} = [i_\alpha, i_\beta]^T$ are the stator currents, $e_{\alpha\beta} = [e_\alpha, e_\beta]^T$ are the back EMFs, R_s is the stator resistance, L_d and L_q are the d-q axis inductances, $L_s = (L_d + L_q)/2$ and $\Delta L = (L_d - L_q)$.

The back EMFs can be written as in equation (2.2).

$$\begin{bmatrix} e_\alpha \\ e_\beta \end{bmatrix} = p\left(\varphi_m \begin{bmatrix} \cos\theta \\ \sin\theta \end{bmatrix}\right) = \omega\varphi_m \begin{bmatrix} -\sin\theta \\ \cos\theta \end{bmatrix} \tag{2.2}$$

where φ_m is the flux linkage and ω is the rotor electric angular speed.

In case of SPMSM, $L_d = L_q = L_s$, $\Delta L = 0$ and the equations can be simplified as follows in equation (2.3).

$$\begin{bmatrix} v_\alpha \\ v_\beta \end{bmatrix} = \begin{bmatrix} R_s + pL_s & 0 \\ 0 & R_s + pL_s \end{bmatrix}\begin{bmatrix} i_\alpha \\ i_\beta \end{bmatrix} + \begin{bmatrix} e_\alpha \\ e_\beta \end{bmatrix} \tag{2.3}$$

The electrical equations of a generic PMSM in the synchronously rotating frame can be expressed as in equation (2.4).

$$\begin{bmatrix} v_d \\ v_q \end{bmatrix} = \begin{bmatrix} R_s + pL_d & -\omega L_q \\ \omega L_d & R_s + pL_q \end{bmatrix} \begin{bmatrix} i_d \\ i_q \end{bmatrix} + \begin{bmatrix} 0 \\ \omega\varphi_m \end{bmatrix} \tag{2.4}$$

where $v_{dq} = [v_d , v_q]^T$ are the stator voltages, and $i_{dq} = [i_d , i_q]^T$ are the stator currents. Also in this case, for a SPMSM the assumption $L_d = L_q = L_s$ is valid.

2.2 ELADRC Algorithm

An enhanced linear disturbance rejection controller was proposed by Qu et al. in [62] for PMSM.

Starting from the motor equations in the d-q reference frame, the back EMF based PMSM model is expressed in an estimated synchronously rotating γ-δ frame as follows, in equation (2.5).

$$\begin{bmatrix} v_\gamma \\ v_\delta \end{bmatrix} = \begin{bmatrix} R_s + pL_d & -\hat{\omega} L_q \\ \hat{\omega} L_q & R_s + pL_d \end{bmatrix} \begin{bmatrix} i_\gamma \\ i_\delta \end{bmatrix} + \begin{bmatrix} e_\gamma \\ e_\delta \end{bmatrix} \tag{2.5}$$

where e_γ and e_δ are the γ and δ axis extended back EMF components and $\hat{\omega}$ is the estimated rotor speed.

The position estimation error is defined as in equation (2.6).

$$\Delta\theta = \theta^r - \theta^e \tag{2.6}$$

where $\hat{\theta}$ is the estimated rotor position on which the γ-δ frame is oriented.

Then, if the estimated rotor speed $\hat{\omega}$ is almost equal to ω, the back EMFs can be approximated as in equation (2.7).

$$\begin{bmatrix} e_\gamma \\ e_\delta \end{bmatrix} = \left(\omega\varphi_m + \Delta L\left(\omega i_d - p i_q\right)\right) \begin{bmatrix} -\sin\Delta\theta \\ \cos\Delta\theta \end{bmatrix} \tag{2.7}$$

In the algorithm the back-EMFs are treated as unknown external disturbances, as they contain the information about the position estimation error. Two linear extended state observers (LESO1 and LESO2) are introduced in [62]: LESO1 is designed to estimate the back EMFs, while LESO2 estimates the internal disturbances represented by the uncertainty of the parameters and the current regulation quality variation of the drive.

LESO1 equations can be expressed as follows in equations (2.8).

$$\begin{cases} p\hat{i}_\gamma = v_\gamma / L_d + f_\gamma + \hat{f}_{e\gamma} - L_{\gamma 1}\varepsilon_\gamma \\ p\hat{f}_{e\gamma} = -L_{\gamma 2}\varepsilon_\gamma \\ p\hat{i}_\delta = v_\delta / L_d + f_\delta + \hat{f}_{e\delta} - L_{\delta 1}\varepsilon_\delta \\ p\hat{f}_{e\delta} = -L_{\delta 2}\varepsilon_\delta \end{cases} \tag{2.8}$$

where $\hat{\mathrm{i}}_\gamma$ and $\hat{\mathrm{i}}_\delta$ are the estimated γ-δ axis stator currents, $\varepsilon_\gamma = \hat{\mathrm{i}}_\gamma - \mathrm{i}_\gamma$ and $\varepsilon_\delta = \hat{\mathrm{i}}_\delta - \mathrm{i}_\delta$ are the current estimation errors, $\mathrm{f}_\gamma = \hat{\omega} \cdot \mathrm{L_q} \cdot \hat{\mathrm{i}}_\delta / \mathrm{L_d} - \mathrm{R_s} \cdot \hat{\mathrm{i}}_\gamma / \mathrm{L_d}$ and $\mathrm{f}_\delta = -\hat{\omega} \cdot \mathrm{L_q} \cdot \hat{\mathrm{i}}_\gamma / \mathrm{L_d} - \mathrm{R_s} \cdot \hat{\mathrm{i}}_\delta / \mathrm{L_d}$ represent the known model information, $\hat{\mathrm{f}}_{\mathrm{e}\gamma} = -\,\mathrm{e}_\gamma / \mathrm{L_d}$ and $\hat{\mathrm{f}}_{\mathrm{e}\delta} = -\,\mathrm{e}_\delta / \mathrm{L_d}$ are the unknown external disturbances, and $\mathrm{L}_{\gamma 1}$, $\mathrm{L}_{\delta 1}$, $\mathrm{L}_{\gamma 2}$, $\mathrm{L}_{\delta 2}$ are the gains of the LESO1.

LESO2 is designed as in equations (2.9)

$$\begin{cases} \mathrm{p}\hat{\mathrm{i}}_{\mathrm{m}\gamma} = \mathrm{v}_\gamma / \mathrm{L_d} + \mathrm{f}_\gamma + \hat{\mathrm{f}}_{\mathrm{e}\gamma} + \hat{\mathrm{f}}_{\mathrm{id}\gamma} - \mathrm{L}_{\gamma 3}\varepsilon_{\mathrm{m}\gamma} \\ \mathrm{p}\hat{\mathrm{f}}_{\mathrm{id}\gamma} = -\mathrm{L}_{\gamma 4}\varepsilon_{\mathrm{m}\gamma} \\ \mathrm{p}\hat{\mathrm{i}}_{\mathrm{m}\delta} = \mathrm{v}_\delta / \mathrm{L_d} + \mathrm{f}_\delta + \hat{\mathrm{f}}_{\mathrm{e}\delta} + \hat{\mathrm{f}}_{\mathrm{id}\delta} - \mathrm{L}_{\delta 3}\varepsilon_{\mathrm{m}\delta} \\ \mathrm{p}\hat{\mathrm{f}}_{\mathrm{id}\delta} = -\mathrm{L}_{\delta 4}\varepsilon_{\mathrm{m}\delta} \end{cases} \tag{2.9}$$

where $\hat{\mathrm{i}}_{\mathrm{m}\gamma}$ and $\hat{\mathrm{i}}_{\mathrm{m}\delta}$ are the estimated γ-δ axis stator currents, $\varepsilon_\gamma = \hat{\mathrm{i}}_{\mathrm{m}\gamma} - \mathrm{i}_\gamma$ and $\varepsilon_\delta = \hat{\mathrm{i}}_{\mathrm{m}\delta} - \mathrm{i}_\delta$ are the current estimation errors, $\hat{\mathrm{f}}_{\mathrm{id}\gamma}$ and $\hat{\mathrm{f}}_{\mathrm{id}\delta}$ are the unknown internal disturbances, and $\mathrm{L}_{\gamma 3}$, $\mathrm{L}_{\delta 3}$, $\mathrm{L}_{\gamma 4}$, $\mathrm{L}_{\delta 4}$ are the gains of the LESO2.

The two LESOs are integrated in the control plant as follows:

- $\hat{\mathrm{f}}_{\mathrm{e}\gamma}$ and $\hat{\mathrm{f}}_{\mathrm{e}\delta}$ are sent to a normalized phase-locked loop (PLL), which regulates $\hat{\mathrm{f}}_{\mathrm{e}\gamma}$ to be zero using a PI regulator and generates the estimated rotor position and speed as outputs.
- a signal which represents the total disturbance (internal and external) is injected as a feedforward compensation term for the input of the plant, adding it to the output of the current controllers. The γ-δ components of the feedforward signal are expressed as in equations (2.10).

$$\begin{cases} \mathrm{v}_{\gamma\mathrm{ff}} = -\mathrm{L_d}\left(\mathrm{f}_\gamma + \hat{\mathrm{f}}_{\mathrm{e}\gamma} + \hat{\mathrm{f}}_{\mathrm{id}\gamma}\right) \\ \mathrm{v}_{\delta\mathrm{ff}} = -\mathrm{L_d}\left(\mathrm{f}_\delta + \hat{\mathrm{f}}_{\mathrm{e}\delta} + \hat{\mathrm{f}}_{\mathrm{id}\delta}\right) \end{cases} \tag{2.10}$$

In addition to that, the PI controllers used in the FOC scheme are replaced by simple proportional regulators, as the plant combined with the two LESOs is equivalent to an integrator 1/s (the proof of this can be found in [8]). Therefore, the FOC diagram has to be slightly modified to implement the ELADRC algorithm. Of course, also in this case $\mathrm{L_d} = \mathrm{L_q} = \mathrm{L_s}$ was assumed.

The LESO1 and LESO2 schemes and integration in the plant are reported in Fig. 2, whereas the PLL is shown in Fig. 3. Please note that in the Fig. 2 $x = \gamma$ *and* δ.

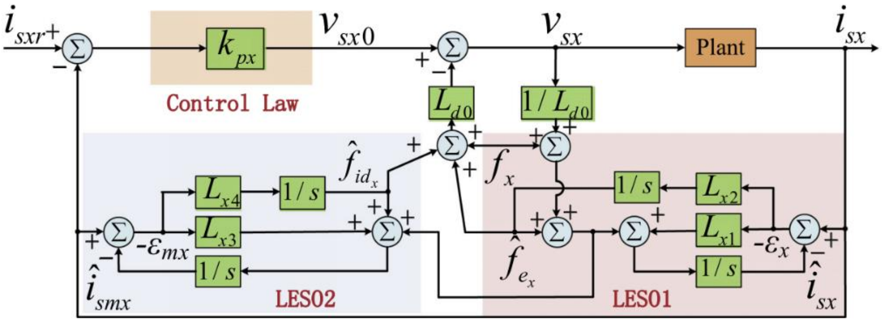

Fig. 2 LESO1 and LESO2 integration in the plant

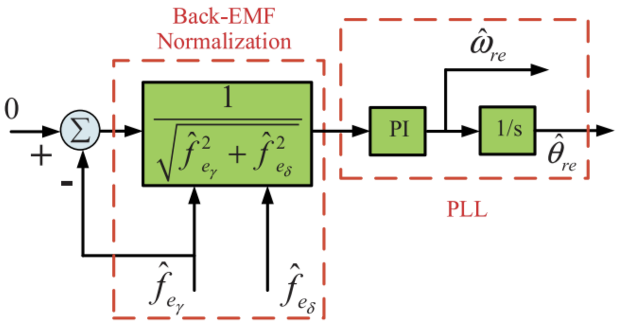

Fig. 3 PLL used for LESO observers

2.3 SMO-FACCF algorithm

An Enhanced Sliding Mode Observer is presented by An et al. in [77]. They improved a well-known sliding-mode algorithm [72-75] adding a frequency-adaptive complex-coefficient filter (FACCF) to it.

According to [77], the SMO can be expressed by the following equation (2.11).

$$p\begin{bmatrix}\hat{i}_\alpha\\ \hat{i}_\beta\end{bmatrix}=-\frac{R_s}{L_s}\begin{bmatrix}\hat{i}_\alpha\\ \hat{i}_\beta\end{bmatrix}+\frac{1}{L_s}\begin{bmatrix}v_\alpha-z_\alpha\\ v_\beta-z_\beta\end{bmatrix} \tag{2.11}$$

where $\hat{i}_\alpha$ and $\hat{i}_\beta$ are the estimated stator currents and z_α , z_β are the sliding mode control functions, which can be expressed as in equation (2.12).

$$\begin{bmatrix}z_\alpha\\ z_\beta\end{bmatrix}=k\begin{bmatrix}\mathrm{sgn}(\hat{i}_\alpha-i_\alpha)\\ \mathrm{sgn}(\hat{i}_\beta-i_\beta)\end{bmatrix} \tag{2.12}$$

where k is the gain parameter.

When the system operates in sliding mode, it can be proved that z_α and z_β contain the back EMFs e_α and e_β and therefore the rotor position information. However, the raw z_α and z_β signals cannot be used for position estimation directly, because they are affected by the chattering due to sliding mode switching function. To overcome this, a sigmoid function is used instead of the signum function. Since this is not enough, the authors constructed a FACCF filter to obtain the estimated back EMFs as in equation (2.13).

$$\begin{bmatrix}\hat{e}_\alpha\\ \hat{e}_\beta\end{bmatrix}=\frac{\omega_c}{s-j\hat{\omega}+\omega_c}\begin{bmatrix}z_\alpha\\ z_\beta\end{bmatrix} \tag{2.13}$$

As they demonstrate, the FACCF behaves like a band-pass filter, whose central frequency is $\hat{\omega}$ and ω_c is the cutoff frequency, generally set to be 0.5 ÷ 10 times the central frequency. If the FACCF is centered on the estimated rotor speed, it filters out the high-frequency components from the sliding mode functions, leaving the back EMFs. At this point, the estimated rotor position and speed can be obtained using a normalized PLL, similarly to the algorithm described before this.

Since the filter scheme involves multiplications by the estimated angular speed, it cannot work if $\hat{\omega}$ is zero, because no output is generated in this condition. For this reason, a switch logic has to be implemented in the algorithm, in order to add a small offset term to $\hat{\omega}$ at zero speed only.

2.4 RFO Algorithm

As it will be shown in section 3.2, the RFO algorithm showed the best results. For this reason, the theoretic description of this algorithm will be carried out more deeply.

2.4.1 Mathematical modelling

If one considers the model of a SPMSM (equations (2.3) and (2.4)) the stator flux derivative ($\dot{\lambda}_{\alpha\beta}=[\dot{\lambda}_{\alpha},\dot{\lambda}_{\beta}]^T$) can be defined as in equation (2.14) and the stator flux ($\lambda_{\alpha\beta}=[\lambda_{\alpha},\lambda_{\beta}]^T$) as in equation (2.15), being φ_m the Permanent Magnet flux linkage constant and $C_{\alpha\beta}(\theta)=[\cos\theta,\sin\theta]^T$.

$$\dot{\lambda}_{\alpha\beta}=v_{\alpha\beta}-Ri_{\alpha\beta} \tag{2.14}$$

$$\lambda_{\alpha\beta}=Li_{\alpha\beta}+\varphi_m C_{\alpha\beta}(\theta) \tag{2.15}$$

The rotor flux ($x_{\alpha\beta}=[x_{\alpha},x_{\beta}]^T$) of a SPMSM can be given by equation (2.16). If one differentiates both sides of (2.16), one obtains equation (2.17), where J is given by equation (2.18) and $p\equiv\frac{d}{dt}$.

$$x_{\alpha\beta}\equiv\lambda_{\alpha\beta}-Li_{\alpha\beta}=\varphi_m C_{\alpha\beta}(\theta) \tag{2.16}$$

$$\dot{x}_{\alpha\beta}=v_{\alpha\beta}-Ri_{\alpha\beta}-Lpi_{\alpha\beta}=-\varphi_m\omega JC_{\alpha\beta}(\theta) \tag{2.17}$$

$$J=\begin{bmatrix}0 & 1\\ -1 & 0\end{bmatrix} \tag{2.18}$$

Since the aim of the sensorless algorithm is to estimate the rotor position, one can calculate such a quantities taking into account equation (2.19).

$$\theta=\tan^{-1}\left(\frac{\hat{x}_{\beta}}{\hat{x}_{\alpha}}\right) \tag{2.19}$$

In [81] an observer with zero initial value was proposed; the state observer $q_{\alpha\beta}$ was defined as in equation (2.20)

$$\dot{q}_{\alpha\beta}(t)=v_{\alpha\beta}-Ri_{\alpha\beta}-Lpi_{\alpha\beta},\quad q(0)=[0,\,0]^T \tag{2.20}$$

Please note that $q_{\alpha\beta}$ and $x_{\alpha\beta}$ have same dynamics, but different initial conditions. If one defines $\xi_{\alpha\beta}=\lambda_{\alpha\beta}(0)-Li_{\alpha\beta}(0)$, if follows equation (2.21).

$$x_{\alpha\beta}(t) = q_{\alpha\beta}(t) + \xi_{\alpha\beta} \tag{2.21}$$

Since $\left\| q_{\alpha\beta} + \xi_{\alpha\beta} \right\|^2 = \left\| x_{\alpha\beta} \right\|^2$ and $\left\| x_{\alpha\beta} \right\|^2 = \varphi_m^2$, one can obtain from equation (2.21) the relation in equation (2.22)

$$-\left\| q_{\alpha\beta} \right\|^2 = 2 q_{\alpha\beta}^T \xi_{\alpha\beta} + \left\| \xi_{\alpha\beta} \right\|^2 - \varphi_m^2 \tag{2.22}$$

In order to obtain a linear regression form, it is necessary to derivate equation (2.22). However, a pure derivative is always associate to noise amplification in real applications, therefore an high-pass filter $\frac{\alpha p}{p+\alpha}$ can be applied to both side of equation (2.22). Indeed, $\frac{\alpha p}{p+\alpha} = p \cdot \frac{\alpha}{p+\alpha}$, i.e., it is a derivative for low-frequencies but with a low-pass filter forms. Applying the high-pass filter to equation (2.22) one obtains equation (2.23), where $y(q_{\alpha\beta})$ and $\Omega_{\alpha\beta}(q_{\alpha\beta})$ are defined in equations (2.24) and (2.25).

$$y(q_{\alpha\beta}) = \Omega_{\alpha\beta}(q_{\alpha\beta})^T \xi_{\alpha\beta} + \varepsilon(t) \tag{2.23}$$

$$y(q_{\alpha\beta}) = \frac{-\alpha p}{p+\alpha}\left(\left\| q_{\alpha\beta} \right\|^2 \right) \tag{2.24}$$

$$\Omega_{\alpha\beta}(q_{\alpha\beta}) = \frac{2\alpha p}{p+\alpha}(q_{\alpha\beta}) \tag{2.25}$$

Since $\left\| \xi \right\|^2 - \varphi_m^2$ is a constant, one obtains equation (2.26) for some C>0.

$$\varepsilon(t) = \frac{p\alpha}{p+\alpha}\left(\left\| \xi \right\|^2 - \varphi_m^2 \right) = \alpha C e^{-\alpha t} \tag{2.26}$$

Equation (2.23) represent a linear regression equation with an unknown parameter ξ. Indeed, it is a product of a known vector $\Omega_{\alpha\beta}(q_{\alpha\beta})$, by $\xi_{\alpha\beta}$. Therefore a parameter estimator can be derived using the descent gradient method, obtaining equation (2.27) and equation (2.28), where Γ is a gain matrix. The derived sensorless control is shown in Fig. 4.

$$\dot{\xi}_{\alpha\beta} = \Gamma \Omega_{\alpha\beta}(q_{\alpha\beta})(y(q_{\alpha\beta}) - \Omega_{\alpha\beta}(q_{\alpha\beta})^T \xi_{\alpha\beta}), \quad \xi_{\alpha\beta}(0) \in \Re^2 \tag{2.27}$$

$$\xi_{\alpha\beta}(0) = \varphi_m \left[\cos(\theta_0); \sin(\theta_0) \right] \tag{2.28}$$

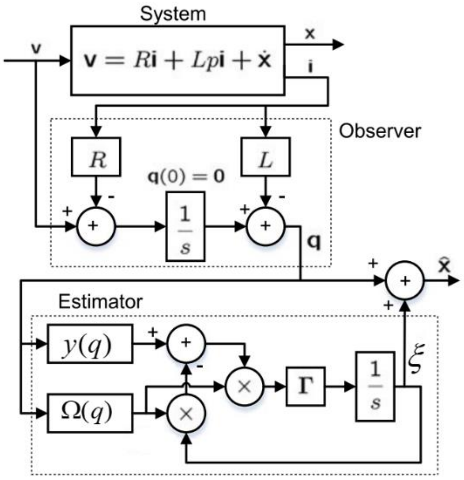

Fig. 4 Observer and parameter estimator proposed in [81]

2.4.2 Simulation results

In order to understand more easily the working principle of the scheme in Fig. 4, some simulation results carried out in study are shown in this section.

Since $q_{\alpha\beta}$ is initialized at zero, the two vector components are affected by a bias error. This bias is related to the real initial rotor angle. For simplicity, one can consider the case in which $\theta_0 = -90°$ and $\xi_{\alpha\beta}$ is initialized correctly, i.e. as in equations (2.29). In this condition, $q_{\alpha\beta}$ is given by equations (2.30) and $x_{\alpha\beta}$ is given by equations (2.31). Indeed, the bias of q_β is corrected by ξ_β, as shown in Fig. 5, where simulation results of this particular condition are shown. In this case, the bias is corrected from the beginning because $\xi_{\alpha\beta}$ is initialized correctly; if $\xi_{\alpha\beta}$ is not initialized correctly, the estimator loop provides the correct bias correction. Please note that the bias of q_β is intrinsic in observer definition; indeed both equations (2.29), (2.30), (2.31) and simulation results of Fig. 5 are obtained in ideal conditions.

$$\begin{cases} \xi_\alpha = \varphi_m \cos(\theta_0) = 0 \\ \xi_\beta = \varphi_m \sin(\theta_0) = -\varphi_m \end{cases} \tag{2.29}$$

$$\begin{cases} q_\alpha = \int v_\alpha - Ri_\alpha = \varphi_m \cos(\theta) \\ q_\beta = \int v_\beta - Ri_\beta = \varphi_m + \varphi_m \sin(\theta) \end{cases} \tag{2.30}$$

$$\begin{cases} x_\alpha = \varphi_m \cos(\theta) \\ x_\beta = \varphi_m \sin(\theta) \end{cases} \tag{2.31}$$

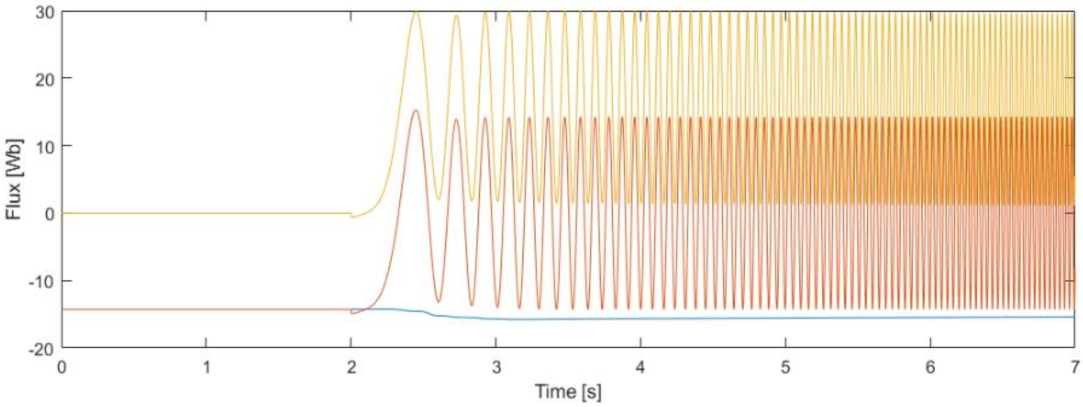

Fig. 5 q_β *(yellow),* ξ_β *(blue) and* x_β *(red) when* $\theta_0=0$*, estimator shown in [81],* φ_m *=14Wb.*

The observer proposed in [81] is straightforward and simple. However, it is sensible to DC disturbances. As an example, one can consider the previous case, with a negative dc error on i_α measure. In this case q_α is given by equation (2.32) and therefore it diverges. The simulation results for this case are shown in Fig. 6. Please note that the observer diverges even if $\xi_{\alpha\beta}$ is correctly initialized, as it can be shown more easily in the simulation plot with time enlargement in Fig. 7.

$$q_\alpha = \int v_\alpha - R(i_\alpha - i_{\alpha DC}) = \varphi_m \cos(\theta) + \int R i_{\alpha DC} \tag{2.32}$$

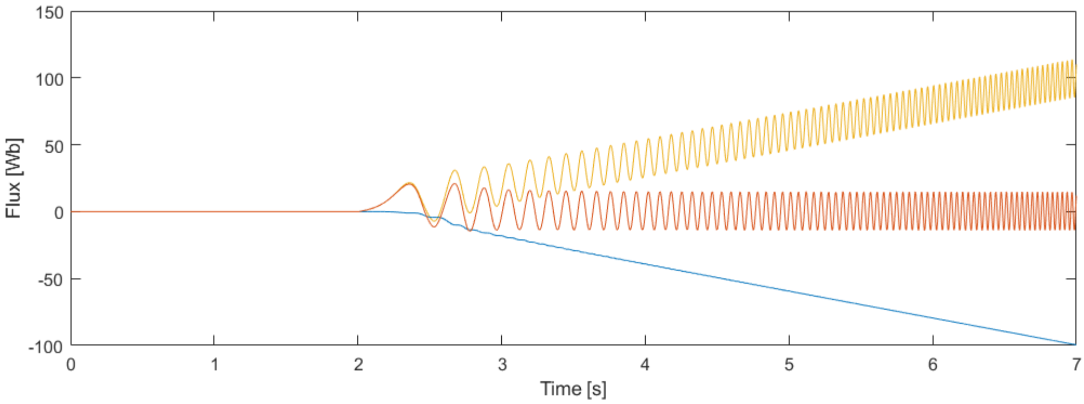

Fig. 6 q_α *(yellow),* ξ_α *(blue) and* x_α *(red) when* $\theta_0=0$ *and with* i_α *negative dc error, estimator shown in [45,]* φ_m *=14Wb.*

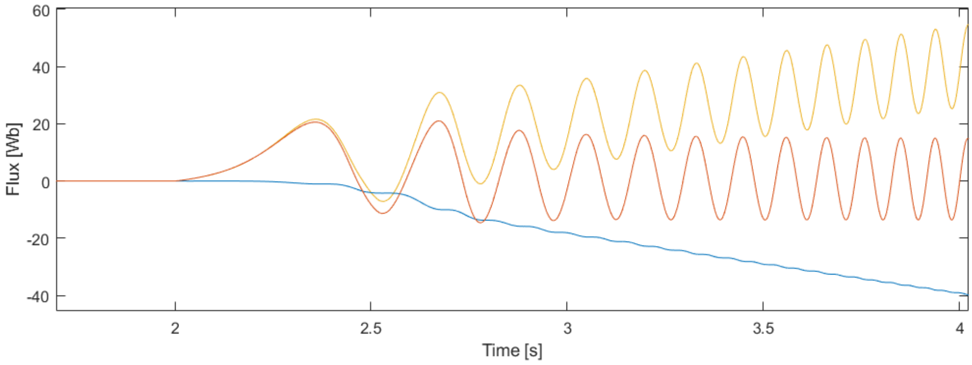

Fig. 7 q_α (yellow), ξ_α (blue) and x_α (red) when $\theta_0=0$ and with i_α negative dc error, estimator shown in [45], time axis enlargement, $\varphi_m=14Wb$.

2.4.3 Feedback addition to avoid dc disturbances

In order to avoid the problem connected to DC disturbances, in [50] a feedback loop was added, as highlighted in blue in Fig. 8.

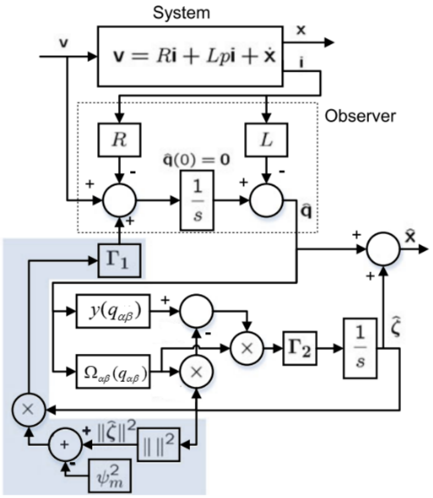

Fig. 8 Observer and parameter estimator proposed in [50]

Adding the feedback containing Γ_1 gain, one obtains the observer defined by equations (2.33).

The simulation with i_α dc disturbance was carried out with the sensorless algorithm defined in equations (2.33) and the results are shown in Fig. 9. One can note that with the addition of the feedback containing Γ_1 gain x_α has null average value and q_α do not diverge anymore.

$$\begin{cases} \dot{q}_{\alpha\beta} = v_{\alpha\beta} - Ri_{\alpha\beta} - Lpi_{\alpha\beta} + \Gamma_1\left(\left\|\xi_{\alpha\beta}\right\|^2 - \varphi_m^2\right), & q_{\alpha\beta}(0) = [0,\ 0]^T \\ \dot{\xi}_{\alpha\beta} = \Gamma_2\Omega(q_{\alpha\beta})\left(y(q_{\alpha\beta}) - \Omega_{\alpha\beta}(q_{\alpha\beta})^T\xi_{\alpha\beta}\right), & \xi_{\alpha\beta}(0) \in \Re^2 \\ y(q_{\alpha\beta}) = \dfrac{-\alpha p}{p+\alpha}\|q\|^2, & y(0) = 0 \\ \Omega_{\alpha\beta}(q_{\alpha\beta}) = \dfrac{\alpha p}{p+\alpha}2q_{\alpha\beta}, & \Omega_{\alpha\beta}(0) = [0,0]^T \\ x_{\alpha\beta} = q_{\alpha\beta} + \xi_{\alpha\beta} \\ \hat{\theta} = atan2\left(\dfrac{x_\beta}{x_\alpha}\right) \end{cases} \tag{2.33}$$

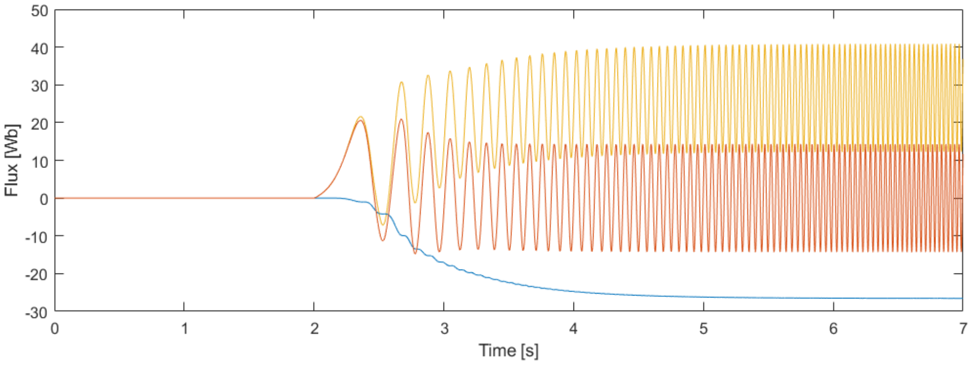

Fig. 9 q_α (yellow), ξ_α (blue) and x_α (red) when θ_0=0 and with i_α negative dc error, estimator shown in [50]

2.4.4 Definition of Γ_2 gain

From the results shown in the previous section, one can note that the feedback loop containing Γ_1 gain aims at avoiding $q_{\alpha\beta}$ divergence. Since it does not intervene directly in the estimator inner loop (containing Γ_2 gain), its influence on the estimator dynamic is limited. On the contrary, the estimator loop containing Γ_2 gain is the core of the RFO observer, and therefore an appropriate tuning of such a parameter is fundamental in order to achieve a good drive dynamic.

Even if this sensorless technique was proposed in [50, 81], none of these papers show a methodology for Γ_2 tuning, which is proposed in this thesis. If one considers the loop shown in Fig. 10, the inputs of the loop are $u_1 = y(q_{\alpha\beta})$ and $u_2 = \Omega_{\alpha\beta}(q_{\alpha\beta})$.

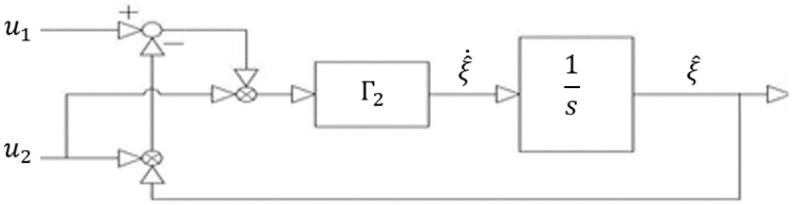

Fig. 10 Γ_2 loop of estimator proposed in [50, 81]

$\dot{\xi}_{\alpha\beta}$ is defined in equation (2.34). Please note that for notation simplicity, the αβ subscripts are omitted in the following equations and complex number notation is exploited. Since the function f_1 is non-linear, a linearization process should be carried out, as shown in equation (2.35). Moreover, since motor drives are discrete systems, equation (2.35) is linearized as in equation (2.36), obtaining, after the algebraic simplifications of equations (2.37) and (2.38), the linearized and discretized equation of the loop in (2.39). Evaluating the eigenvalue as in equation (2.40), one obtains the eigenvalue in (2.41), where Tc is the sampling time.

$$\dot{\xi} = f_1 = \Gamma_2 u_2 (u_1 - u_2 \xi) \tag{2.34}$$

$$\dot{\xi} = \left[\frac{\partial f_1}{\partial \xi}\right][\xi] + \left[\frac{\partial f_1}{\partial u_1}\ \frac{\partial f_1}{\partial u_2}\right]\begin{bmatrix} u_1 \\ u_2 \end{bmatrix} \tag{2.35}$$

$$\frac{\xi(k+1)-\xi(k)}{T_C} = \frac{\partial f_1}{\partial \xi}\xi(k) + \left[\frac{\partial f_1}{\partial u_1}\ \ \frac{\partial f_1}{\partial u_2}\right]\begin{bmatrix} u_1(k) \\ u_2(k) \end{bmatrix} \tag{2.36}$$

$$\xi(k+1) = \frac{\partial f_1}{\partial \xi}\xi(k) T_C + \xi(k) + \left[\frac{\partial f_1}{\partial u_1}\ \ \frac{\partial f_1}{\partial u_2}\right]\begin{bmatrix} u_1(k) \\ u_2(k) \end{bmatrix} T_C \tag{2.37}$$

$$\xi(k+1) = \left[\frac{\partial f_1}{\partial \xi} T_C + 1\right]\xi(k) + \left[\frac{\partial f_1}{\partial u_1} T_C\ \ \frac{\partial f_1}{\partial u_2} T_C\right]\begin{bmatrix} u_1(k) \\ u_2(k) \end{bmatrix} \tag{2.38}$$

$$\xi(k+1) = A\xi(k) + B\begin{bmatrix} u_1(k) \\ u_2(k) \end{bmatrix}, \qquad A = -\Gamma_2 u_2^2 T_C + 1 \tag{2.39}$$

$$A - \lambda = -\Gamma_2 u_2^2 T_C + 1 - \lambda \tag{2.40}$$

$$\lambda = -\Gamma_2 u_2^2 T_C + 1 \tag{2.41}$$

If one approximates the output of the observer as a sinusoidal function, as in equation (2.42) and neglects the low-pass filter of $\Omega_{\alpha\beta}(q_{\alpha\beta})$ function, one obtains equation (2.43). Neglecting the stator resistance and the stator inductance, i.e., considering $\|\psi\omega\| = \|v\|$, one can define the eigenvalue as in equation (2.44).

$$q_{\alpha\beta} = [\varphi_m \cos(\omega t),\ \varphi_m \sin(\omega t)]^T \tag{2.42}$$

$$u_2 = 2pq = [-2\varphi\omega \sin(\omega t),\ 2\varphi\omega\cos(\omega t)]^T \tag{2.43}$$

$$\lambda = -4\Gamma_2 v^2 T_C + 1 \tag{2.44}$$

Since a discrete system is stable if the eigenvalues are inside the circle with centre in the axis origin and having unitary radius, it follows that the loop of Fig. 10 is stable if condition in equation (2.45) is verified. Imposing null eigenvalue, the gain Γ_2 can be defined as in equation (2.46)

$$-2 < -4\Gamma_2 v^2 T_C < 0 \tag{2.45}$$

$$\lambda = 0 \;\; \rightarrow \Gamma_2 = \frac{1}{4v^2 T_C} \tag{2.46}$$

In equation (2.42) the low pass filter is neglected, i.e., the condition in equation (2.47) is imposed. Indeed the high-pass filter can be seen as a combination of a low-pass filter with the derivative operation, as specified in equation (2.48). It is interesting to note that when the frequency of the stator voltage is higher than the cut-off frequency of the filter, the eigenvalue is defined as in equation (2.49). Since in this condition inequation (2.50) is verified, it follows that, from stability point of view, neglecting the low-pass filter is a conservative hypothesis.

$$u_2 = \frac{p\alpha}{p+\alpha} 2q \cong 2pq \tag{2.47}$$

$$\frac{s\alpha}{s+\alpha} = s\frac{\alpha}{s+\alpha} \tag{2.48}$$

$$\omega \gg \alpha \rightarrow \lambda = -4\Gamma_2 (\psi\alpha)^2 T_C + 1 \tag{2.49}$$

$$4\Gamma_2 (\psi\alpha)^2 T_C < 4\Gamma_2 v^2 T_C \tag{2.50}$$

2.5 Extended-RFO Algorithm

A different type of nonlinear observer was developed by Choi et al. in [82].
First, they defined the active flux as in equation (2.51).

$$x = \left(\Delta L \begin{bmatrix} i_\alpha & i_\beta \end{bmatrix} \begin{bmatrix} \cos\theta \\ \sin\theta \end{bmatrix} + \varphi_m\right) \begin{bmatrix} \cos\theta \\ \sin\theta \end{bmatrix} \tag{2.51}$$

Then, $\|x\|^2$ is converted into a new linear regression form, to which a high-pass filter $\left(\frac{\alpha p}{p+\alpha}\right)$ is applied to minimize the effect of constant terms, similarly to the previous algorithm.
The resulting observer is summarized as in equations (2.52).

$$\begin{cases} \dot{\hat{\lambda}} = v_{\alpha\beta} - R_s i_{\alpha\beta} + \gamma\Omega_2\left(y - \Omega_2{}^T\hat{x}\right), \qquad \hat{\lambda}(0) \in \mathbb{R}^2 \\ \hat{x} = \hat{\lambda} - L_q i_{\alpha\beta} \\ \Omega_1 = \dfrac{\alpha}{p+\alpha}\left(v_{\alpha\beta} - R_s i_{\alpha\beta} + \alpha L_q i_{\alpha\beta}\right) - \alpha L_q i_{\alpha\beta} \\ \Omega_2 = \dfrac{\alpha}{p+\alpha}\left(v_{\alpha\beta} - R_s i_{\alpha\beta} + \alpha L_d i_{\alpha\beta}\right) - \alpha L_d i_{\alpha\beta} \\ y = \dfrac{1}{p+\alpha}\Omega_1{}^T\Omega_2 + \dfrac{1}{2}\left(\dfrac{1}{\alpha} - \dfrac{1}{p+\alpha}\right)\|\Omega_1\|^2 + \Delta L\Omega_1{}^T\left(\dfrac{\alpha}{p+\alpha} i_{\alpha\beta}\right) \end{cases} \tag{2.52}$$

where γ is the observer gain and α affects the bandwidth of the high-pass filter.
Finally, the estimated rotor position can be calculated as in equation (2.53).

$$\hat{\theta} = \tan^{-1}\left(\frac{\hat{x}_\beta}{\hat{x}_\alpha}\right) \tag{2.53}$$

Note that the regression model-based algorithm was developed for an IPMSM, as demonstrated by the fact that ΔL appears in the equations. However, the model can be adapted to a SPMSM, as the authors themselves state, simply assuming $L_d = L_q = L_s$ and $\Delta L = 0$. In this case, $\Omega_1 = \Omega_2$ and the equations are simplified as in equations (2.54).

$$\begin{cases} \dot{\hat{\lambda}} = v_{\alpha\beta} - R_s i_{\alpha\beta} + \gamma\Omega(y - \Omega^T\hat{x}), \qquad \hat{\lambda}(0) \in \mathbb{R}^2 \\ \hat{x} = \hat{\lambda} - L_s i_{\alpha\beta} \\ \Omega = \dfrac{\alpha}{p+\alpha}\left(v_{\alpha\beta} - R_s i_{\alpha\beta} + \alpha L_s i_{\alpha\beta}\right) - \alpha L_s i_{\alpha\beta} \\ y = \dfrac{1}{2}\left(\dfrac{1}{\alpha} + \dfrac{1}{p+\alpha}\right)\|\Omega\|^2 \end{cases} \tag{2.54}$$

Another aspect should be mentioned: this algorithm needs the flux linkage value only to compute the initial condition of state variable x.

2.6 Direct axis current (Id) reference management

A novel management of direct axis current (Id) reference is proposed in this thesis and tested on the RFO algorithm.

x_α and x_β derivatives (equations (2.33)) tend to zero at low speed, as a matter of fact x_α and x_β are quasi-sinusoidal quantities with almost constant peak values and frequency equal to motor electric frequency. Taking into account inverter nonlinearities, which are reported in Fig. 11 [54], when currents approach zero, the inverter voltage drops change rapidly, therefore nonlinearities compensation is less precise; if also voltage tends to zero (i.e. low speed), the influence of voltage drop on voltage estimation becomes significant and the estimation worsen. This condition is particularly critical during transition from medium-high speed to low speed; indeed, voltages and currents approach rapidly zero, starting from high values. An heuristic method was implemented to improve algorithm performance during transients [53]. Id reference ($\overline{Id}$), which is normally zero in order to minimize losses, is set to a positive value during transients. In this way, the current is different from zero and the inverter works in the region where the voltage drop is almost constant and therefore nonlinearities compensation is more efficient. This aspect is confirmed by the fact that the current amplitude which should be injected is almost independent from motor sizing but depends on inverter features (dead times, parasitic capacitance etc.). In SPMSM $Ld \cong Lq$ and therefore electromagnetic torque is almost directly proportional to Iq; for this reason the injection of a constant d-axis current does not produce electromagnetic torque. In addition to that, defining Id_{real} and Iq_{real} as the d-axis and q-axis current in the real synchronous reference (reference with θ_r), the relation between currents and estimated angle error $\Delta\theta$ (defined in equation

(2.55)) is given by equations (2.56) and (2.57), where Iq_{ref} is the Iq reference value. Therefore, the torque produced by Iq_{real} contributes to $\Delta\theta$ reduction (since the additional term to Iq_{ref} accelerates the motor if the estimated angle is lower than the real angle and vice versa). Id reference management flowchart is shown in Fig. 12, whereas parameter values are reported in Table 1. Please note that $\omega_{\lim}$ has to be considered as speed absolute value; indeed the algorithm works both with positive and negative speed. The values in Table 1 and Fig. 12 were evaluated experimentally; $\overline{Id}$ and $\omega_{\lim}$ are the lower values that guarantee a proper behaviour of the sensorless control.

$$\Delta\theta = \theta_r - \theta_r^e \tag{2.55}$$

$$Id_{real} = \overline{Id} \cdot \cos(\Delta\theta) \tag{2.56}$$

$$Iq_{real} = Iq_{ref} + \overline{Id} \cdot \sin(\Delta\theta) \tag{2.57}$$

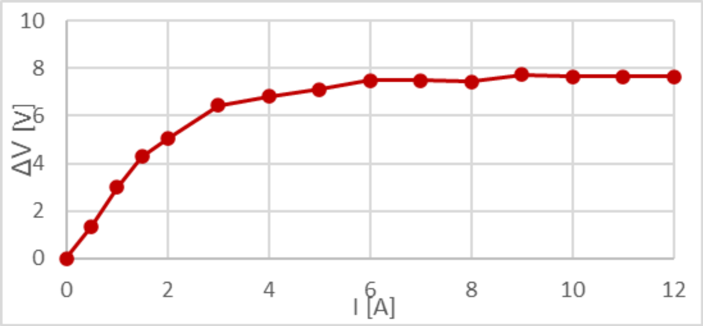

Fig. 11 Inverter voltage drop (ΔV) as a function of motor current (I)

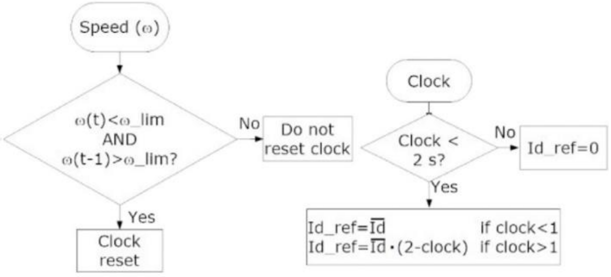

Fig. 12 Id reference management during transient

Table 1 Id reference management parameters

Symbol	29 Nm PMSM	2 Nm PMSM	9.5 Nm PMSM
$\omega_{\lim}$	50 rad/s	50 rad/s	50 rad/s
$\overline{Id}$	2 A	2 A	2 A

2.7 FOC scheme

All the algorithms have been implemented on the same FOC scheme, shown in Fig. 13

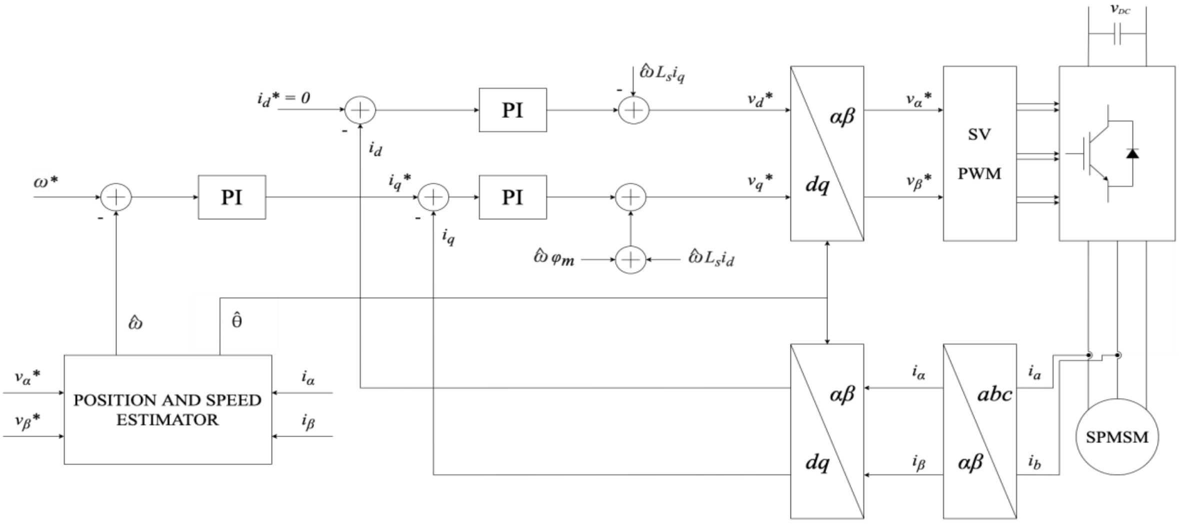

Fig. 13 FOC scheme

The estimated rotor speed was obtained sending the position estimation to a PLL shown in Fig. 14. This made it possible to avoid deriving the estimated angle, which would lead to amplify the high-frequency content of the signal.

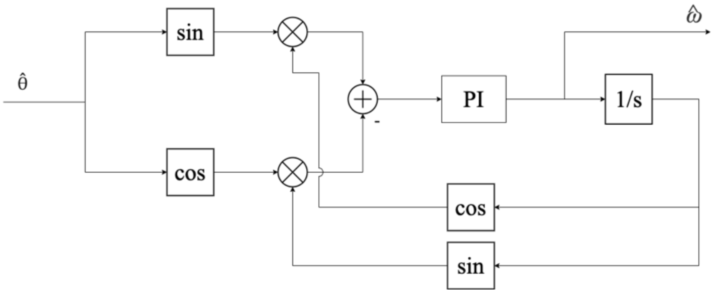

Fig. 14 PLL scheme

The gains of the PLL PI can be evaluated considering the transfer function in equation (2.58), which is the combination of an integrator and a delay. Considering a Tc equal to 200 us (5 kHz of frequency) and in order to obtain a phase margin higher than 60°, $k_{pPLL} = 800, k_{iPLL} = 10000$ can be chosen.

$$G_{PLL}(s) = \frac{1}{s} \frac{1}{sT_c + 1} \qquad (2.58)$$

3 Test bench and experimental result on SPMSM

3.1 Test bench

The algorithms were tested at first in the PETRA Lab of the Electrical, Electronics and Telecommunication Engineering and Naval Architecture Department (DITEN) in the University of Genoa.

The control was implemented in the platform for Rapid Control Prototyping (RCP) Dspace MicroLabBox.

The digital single-ended signals to control the PWM are sent to a board that converts them to fiber-optic signals, which are sent to the inverter, as shown in Fig. 15. Two analog inputs for current measurements and a resolver interface (which is used to compare the estimated angle with the real angle) are also used.

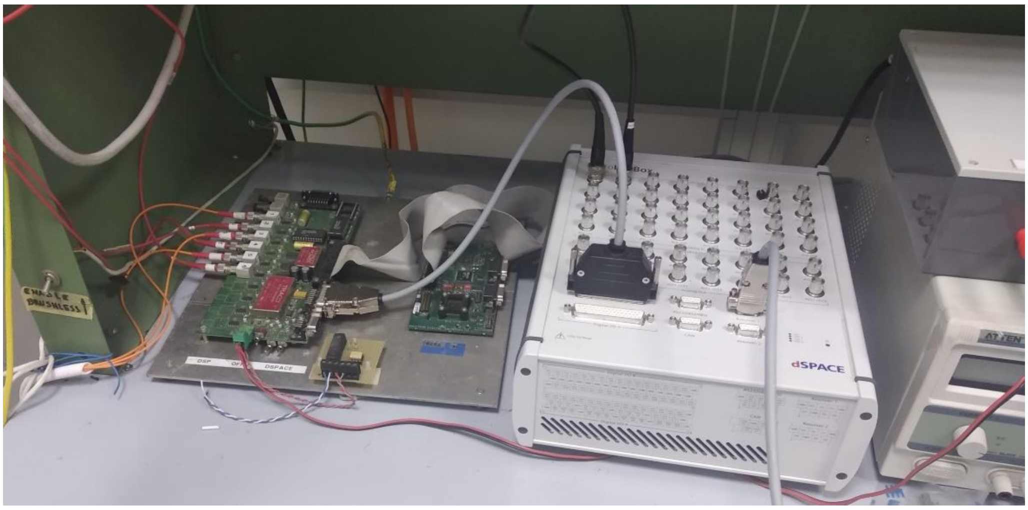

Fig. 15 Dspace MicroLabBox and board to convert single-ended signals to fiber-optic signals

The inverter used to supply the motor is a prototype inverter which has three fiber-optic signals as input and that has a dedicated board to add the dead times to the PWM commands and to implement the inverter protections. The inverter is shown in Fig. 16 and inverter parameters are reported in Table 2.

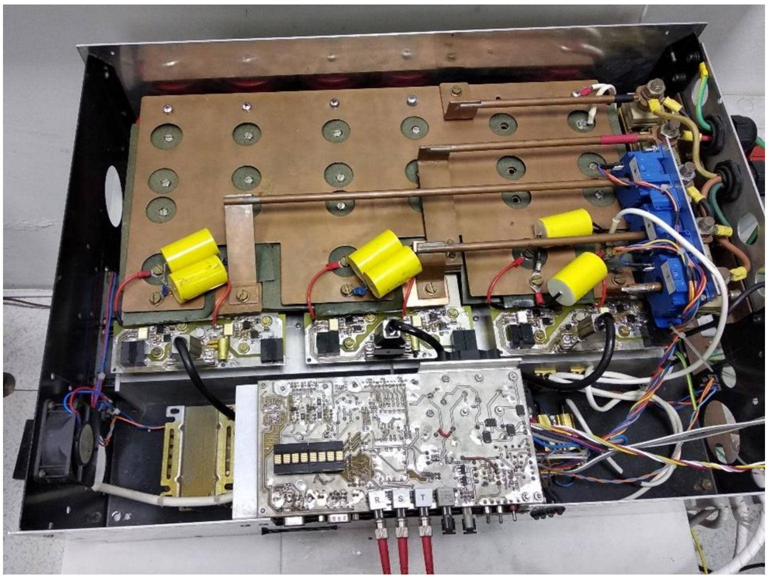

Fig. 16 Prototype inverter

Table 2 Prototype inverter parameters

Parameter	**Value**
Rated current	300 A
DC link voltage	550 V
Dead time	4 µs
PWM switching frequency	5 kHz
Sampling frequency	5 kHz

Regarding the motor test bench, different configurations were proposed in order to test the algorithms.

The first test bench consisted of two coupled motor, as shown in Fig. 17. One motor simulates the load, it is a 29 Nm one equipped with an absolute encoder, so that a sensored FOC can be implemented and the different load profiles can be generated precisely. A 29 Nm motor and a 2 Nm motor can be coupled to the load-motor. Each motor is equipped with a resolver, which is used to compare the estimated angle with the measured angle. Only the estimated angle is used in the sensorless FOC.

Another test bench was proposed, which consist in a 9.5 Nm motor coupled with an air compressor. The compressor is a particularly demanding load since it is characterized by high torque at standstill and, moreover, the torque is highly intermittent. The air compressor test bench is shown in Fig. 18.

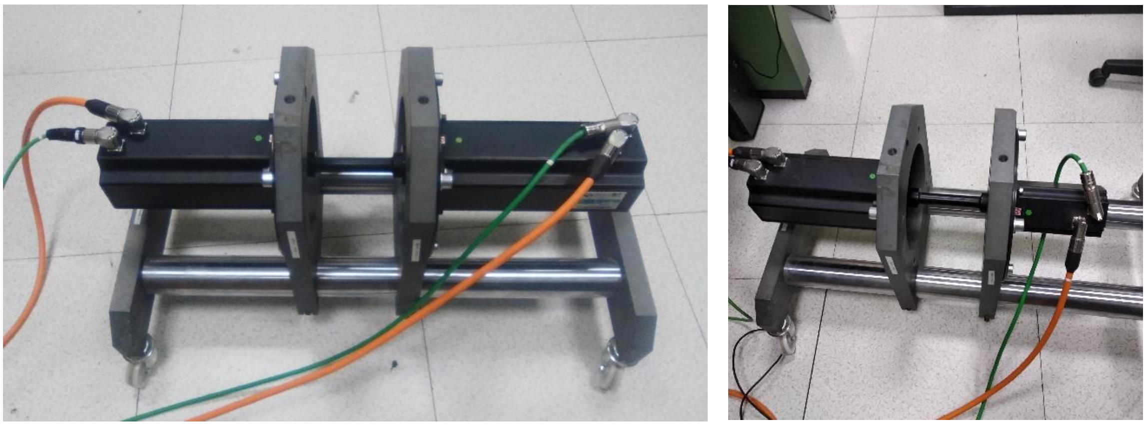

Fig. 17 (left) 29 Nm motor test bench (right) 2 Nm motor test bench

Fig. 18 Air compressor test bench, 9.5 Nm

The characteristics of the three different motors are reported in Table 3.

LEM hall effect probes are used to measure two phase currents and, since the motor is a 3-wire system, the third current is calculated as the opposite of the two current sum.

Table 3 Motor parameters

	29 Nm	2 Nm	9.5 Nm
Voltage	350 V	376 V	370 V
Current	11.9 A	2.2 A	8.9 A
Mechanical speed	209 rad/s	520 rad/s	419 rad/s
Torque	29 Nm	2 Nm	9.5 Nm
Pole pairs	4	4	4
Winding resistance	0.83 Ω	1.75 Ω	0.5 Ω
Winding inductance	4.8 mH	5.75 mH	2.3 mH
Flux linkage constant	0.342	0.147	0.18

3.2 Sensorless passive algorithm comparison: ELADRC, SMO-FACCF, RFO and Extended-RFO

The test bench with the load-motor coupled with the 2 Nm motor, Fig. 17 (right), was used to perform the comparative tests for the four different algorithms.

Since the low-speed region is the critical operating area, the test were performed in these working conditions considering different torque profiles. In particular, motor starting with rated torque at standstill was tested. Indeed, this test is of primary importance in order to understand if the sensorless algorithm can work from standstill or if it is necessary to start the motor with other methods (e.g., active methods or I-F) and then switching to the passive algorithm at a certain speed. Moreover, since the passive algorithms are based on the motor model, algorithm robustness towards parameter variations (in particular, stator inductance and flux linkage) should be analysed.

In particular, the following test were carried out:

- **Test 1.** The reference speed value was changed, in no-load conditions, from 0 to 20% of nominal speed in three consecutive steps: first it was set to 15.6 rad/s, which corresponds to 3% of the rated speed, then to 52 rad/s (10% of rated speed) and finally to 104 rad/s (20% of rated speed). Then, a rated load torque step was applied at 104 rad/s.

- **Test 2.** The motor was started from zero speed with constant rated torque applied, setting the reference speed to 3% of rated speed.

- **Test 3.** A load step from 0 to 50% of the rated torque was applied when the motor was running at 52 rad/s (10% of rated speed). Then, full torque was applied, and reduced to 50% again. When possible, full load torque was applied and removed directly.

- **Test 4.** An error in the stator inductance parameter was introduced at 52 rad/s with full load torque applied if possible. The inductance value was changed from 5.7 mH (its real value) to 3.0 mH, then to its real value again, and finally to 9.0 mH.

- **Test 5 (only RFO and Extended-RFO).** An error in the flux linkage constant was introduced at 52 rad/s with full load torque applied. First it was changed from 0.147 Wb (rated flux) to 0.1 Wb, then to 0.147 Wb again and finally to 0.2 Wb.

- **Test 6 (only RFO and Extended-RFO).** A no-load starting was performed with the flux parameter set to 0.1 Wb (68% of its real value), setting the reference speed to 3% of rated speed. If successful, a full-load starting test was then carried out.

Please note that during the tests with constant rated torque, the torque T_L was managed to be proportional to the rotor speed in the operating region close to standstill, and then limited to the rated value T_N for immediately higher speed values, as expressed by equation (3.1).

$$T_L[Nm] = 2 \cdot T_N[Nm] \cdot \omega[rad/s], \quad |T_L| \le T_N \tag{3.1}$$

3.2.1 Test 1

The reference speed value was set to 3%-10%-20% of rated speed, consecutively, starting from standstill, in no-load conditions; then a full load step was applied. The ELADRC was faster to start the motor than the others (Fig. 19 left), but the error peak-to-peak amplitude was higher (0.4 rad). Extended-RFO had the lowest average error (Fig. 20 right). RFO showed stable performances at all the speed levels, having a generally low estimation error mean value and fluctuation (Fig. 20 left). Note that ELADRC and FACCF-SMO were not able to withstand the full load torque step at all (Fig. 19). Position estimation results are summarized in Table 4.

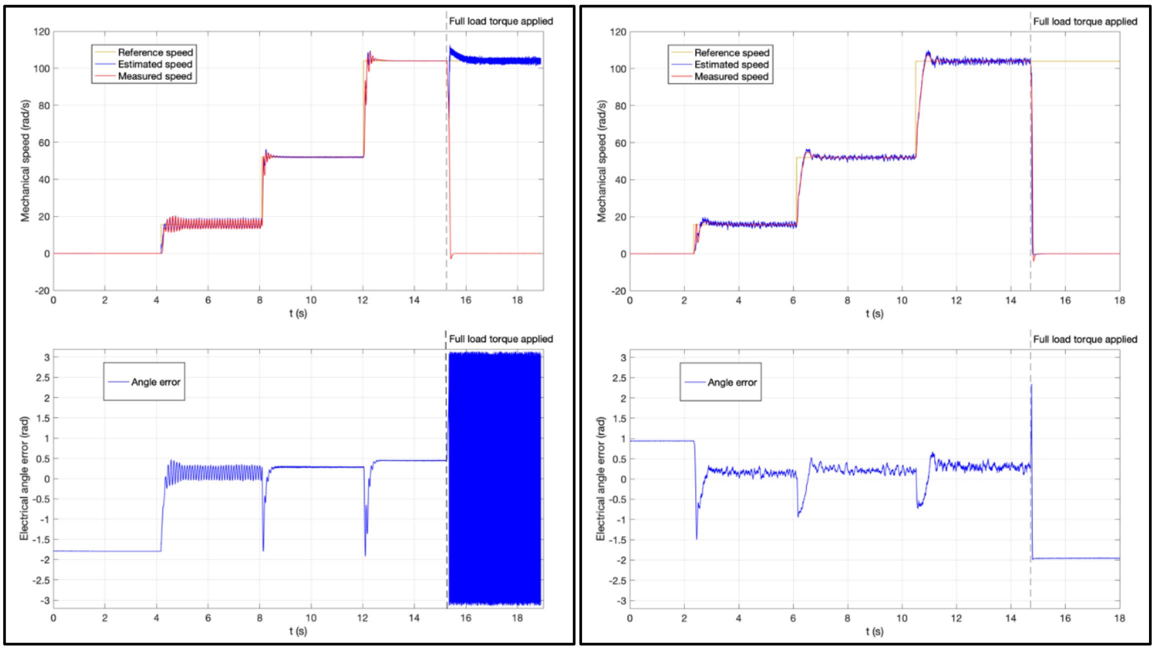

Fig. 19 (left) ELADRC (right) SMO-FACCF. Speed and angle error when reference speed is set to 3%, 10%, 20% of rated speed in no-load conditions and after full load step is applied at 20% of rated speed (Test1).

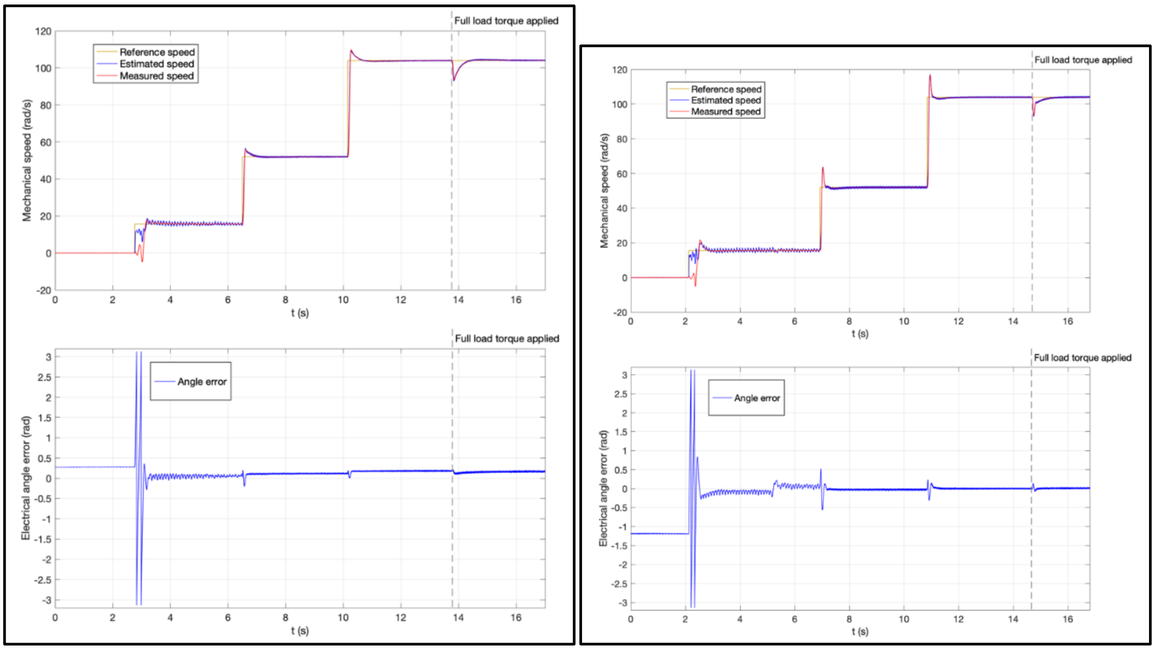

Fig. 20 (left) RFO (right) Extended-RFO. Speed and angle error when reference speed is set to 3%, 10%, 20% of rated speed in no-load conditions and after full load step is applied at 20% of rated speed (Test1).

Table 4 Position estimation errors during Test 1

Algorithm	Angle estimation error ε_θ (rad) Mean value / Peak-to peak amplitude				Starting time 0-3% ω_N
	3% ω_N	10% ω_N	20% ω_N	Full load applied	
ELADRC	0.15/ 0.4	0.28/ 0.03	0.45/ 0.02	Not successful	0.2 s
SMO-FACCF	0.15/ 0.3	0.2/ 0.3	0.3/ 0.25	Not successful	0.3 s
RFO	0.05/ 0.14	0.12/ 0.04	0.18/ 0.04	0.16/ 0.05	0.4 s
Extended-RFO	-0.1/0.12	-0.03/ 0.05	0.0/ 0.04	0.01/ 0.05	0.4 s

3.2.2 Test 2

Only the RFO was able to start the motor with constant full load torque applied (Fig. 22 left). The behaviour of the other algorithms is reported in Fig. 21 and Fig. 22. Since starting process at 3% of rated speed was successful in that case, also 10% and 20% speed steps were applied and the algorithm showed good performances, as Fig. 22(left) reports. The motor did not start with the other observers, as summarized in Table 5.

Please note that, even if the no-load motor starting with the RFO is longer than the starting with the other methods (as shown in Test1) the RFO is the only algorithm that is able to start the motor with full torque.

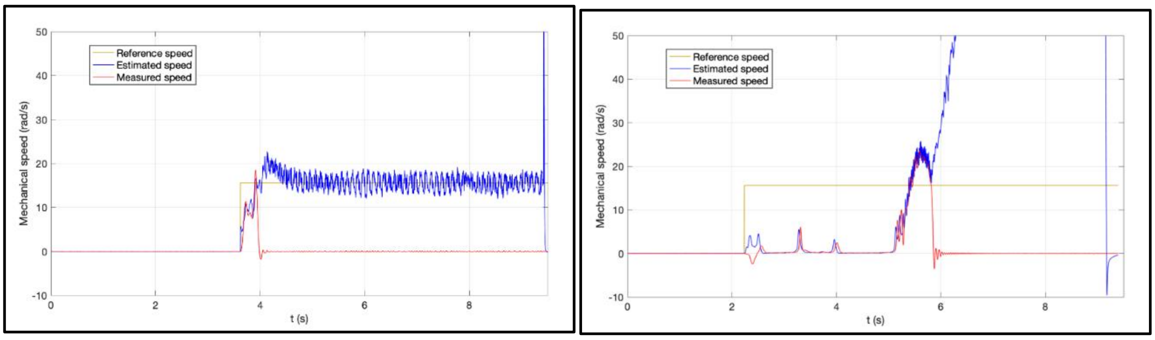

Fig. 21 (left) ELADRC (right) SMO-FACCF. Reference speed, estimated speed and measured speed during full-load starting at 3% of rated speed (Test2).

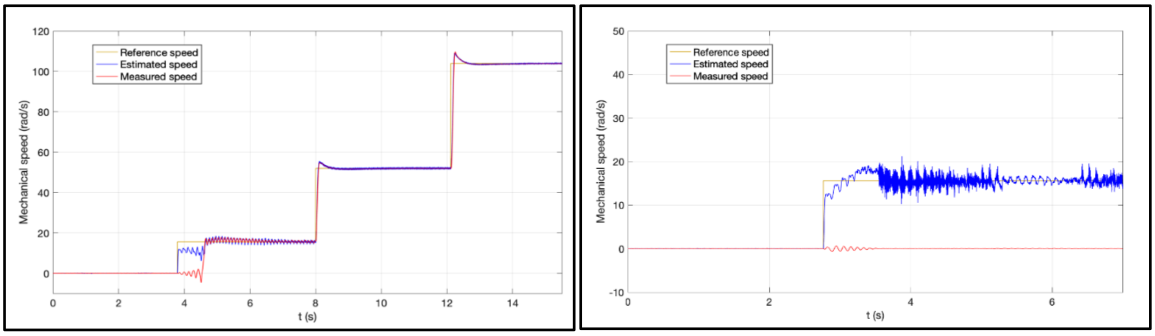

Fig. 22 (left) RFO (right) Extended-RFO. Reference speed, estimated speed and measured speed during full-load starting at 3% of rated speed (Test2).

Table 5 Algorithm performances during Test 2

	Performance during full-load starting
ELADRC	Not successful
SMO-FACCF	Not successful
RFO	Successful
Extended-RFO	Not successful

3.2.3 Test 3

Load torque steps were applied at 10% of rated speed. It was possible to apply full rated torque directly without leading to instability only with RFO and Extended-RFO. They both reacted well to a full load step (Fig. 24); in particular, RFO Algorithm returned to the previous no-load angle error value, but after a slightly longer transient.

Rated load torque was applied gradually in two steps (0%-50%-100%) to the other algorithms. ELADRC managed to keep the speed at its reference during load changes (Fig. 23 left), while there was a stability collapse for the FACCF-SMO as the load torque reached 100% of its rated value (Fig. 23 right). Table 6 shows the mean value of position error for each case and its variation with respect to the no-load condition at the same speed.

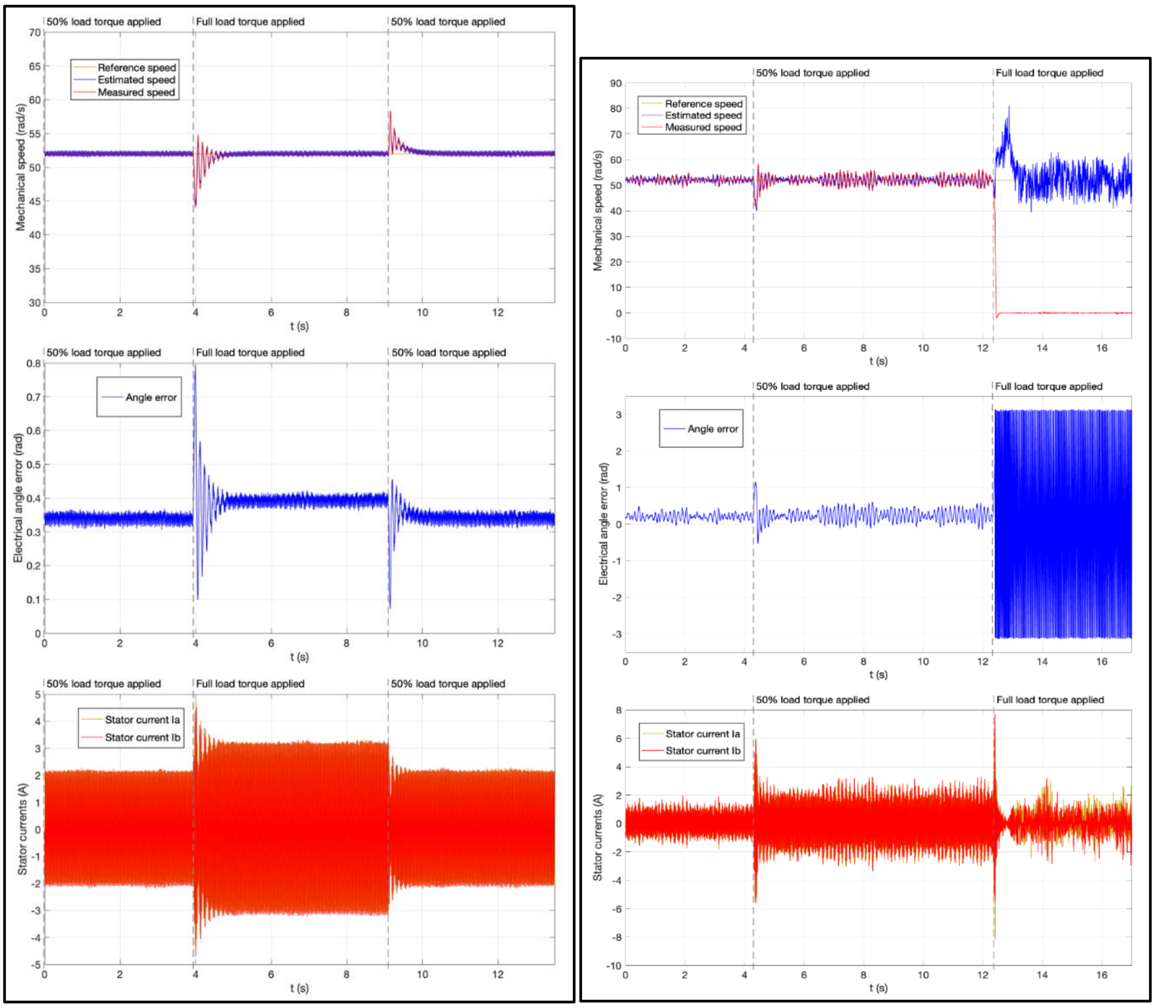

Fig. 23 (left) ELADRC (right) SMO-FACCF. Speed, angle error and measured stator currents when 50% and 100% of rated load torque is applied at 10% of rated speed (Test3).

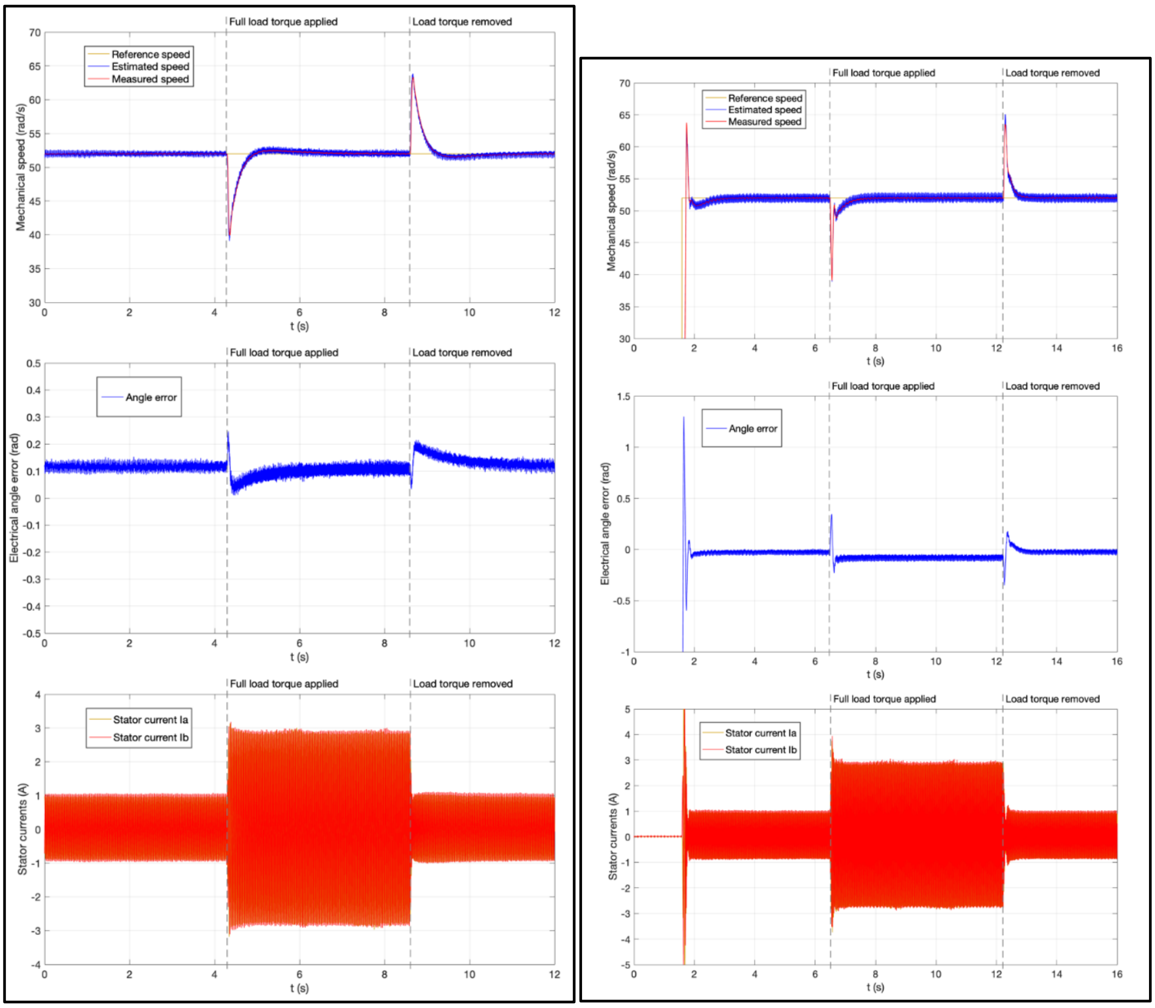

Fig. 24 (left) RFO (right) Extended-RFO. Speed, angle error and measured stator currents when full load torque is applied at 10% of rated speed (Test3).

Table 6 Position estimation errors during Test 3

Algorithm	Angle estimation error ε_θ (rad) at 10% ω_N Mean value / Variation from no-load	
	50% rated torque applied	100% rated torque applied
ELADRC	0.33 / $\Delta\varepsilon_\theta$=0.05	0.39 / $\Delta\varepsilon_\theta$=0.11
SMO-FACCF	0.25 / $\Delta\varepsilon_\theta$=0.05	Not successful
RFO	N.A.	0.12 / $\Delta\varepsilon_\theta$=0
Extended-RFO	N.A.	-0.08 / $\Delta\varepsilon_\theta$=-0.05

3.2.4 Test 4

As regards Test 4, variations in the stator inductance parameter were introduced in full load condition, except for the FACCF-SMO which could not withstand rated load torque as showed before and was therefore tested under 50% load condition. Results are listed in Table 7. Extended-RFO Algorithm showed the greatest robustness against inductance variations (Fig. 26 right). Position estimation error varied less than ± 0.1 rad with ELADRC (Fig. 25 left), while a greater variation was observed in the RFO (Fig. 26 left). FACCF-SMO became unstable when the inductance parameter was set to 9 mH (Fig. 25 right).

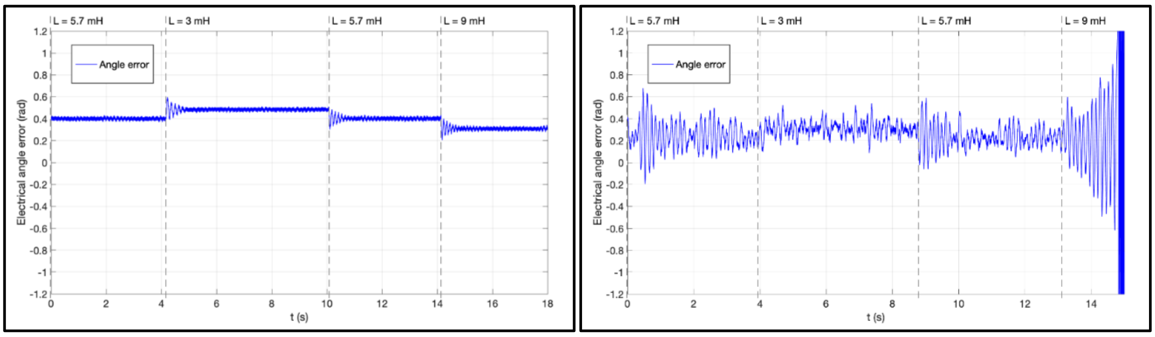

Fig. 25 (left) ELADRC (right) SMO-FACCF. Angle error when variations in the stator inductance parameter are introduced at 10% of rated speed with 50% of rated load torque applied (Test4).

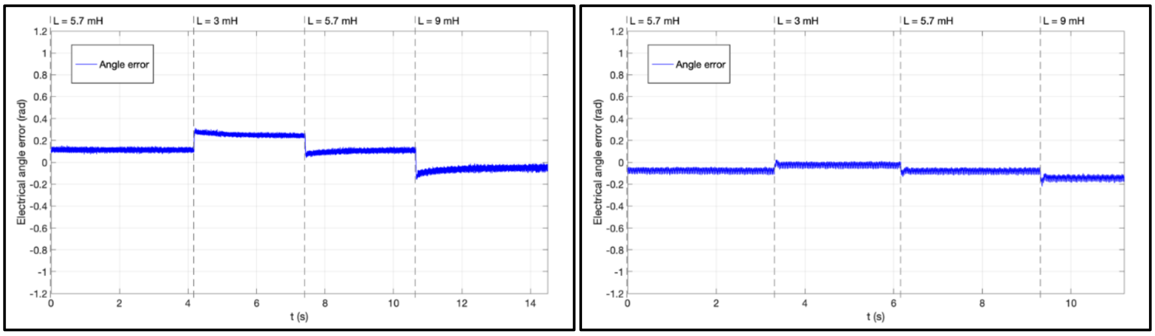

Fig. 26 (left) RFO (right) Extended-RFO. Angle error when variations in the stator inductance parameter are introduced at 10% of rated speed in full load conditions (Test4).

Table 7 Position estimation errors during Test 4

Algorithm	Angle estimation error ε_θ (rad) at 10% ω_N Mean value / Variation with respect to the real inductance condition (L = 5.7 mH)	
	L = 3 mH	L = 9 mH
ELADRC	0.48 / $\Delta\varepsilon_\theta$=0.09	0.31 / $\Delta\varepsilon_\theta$=-0.08
SMO-FACCF (half load)	0.3 / $\Delta\varepsilon_\theta$=0.05	Unstable
RFO	0.25 / $\Delta\varepsilon_\theta$=0.13	-0.05 / $\Delta\varepsilon_\theta$=-0.17
Extended-RFO	-0.03 / $\Delta\varepsilon_\theta$=0.05	-0.15 / $\Delta\varepsilon_\theta$=-0.07

3.2.5 Test 5

Test 5 was performed under full load condition, applying variations to the flux linkage constant. As summarized in Table 8, both RFO and Extended-RFO showed great robustness against changes in flux linkage value, with no appreciable error variation (Fig. 27).

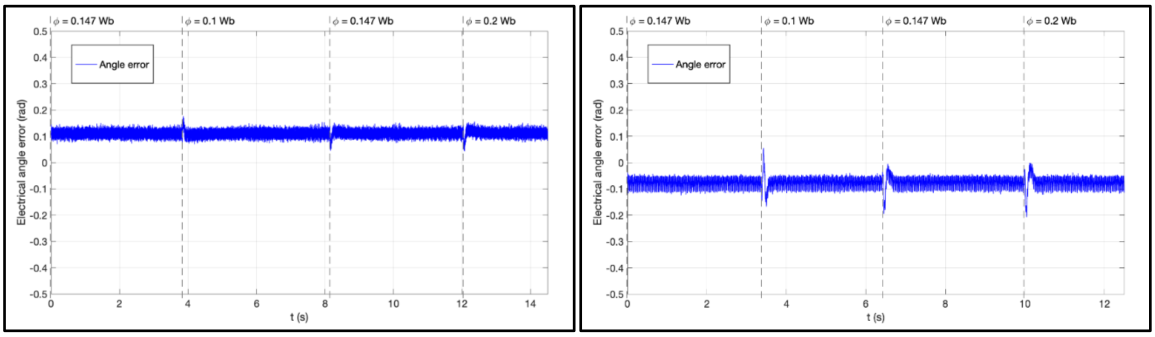

Fig. 27 (left) RFO (right) Extended-RFO. Angle error when variations in the flux linkage parameter are introduced at 10% of rated speed in full load conditions (Test5).

Table 8 Position estimation errors during Test 5

Algorithm	Angle estimation error ε_θ (rad) at 10% ω_N Mean value / Variation with respect to the real flux condition (φ_m = 0.147 Wb)	
	φ_m = 0.1 Wb	φ_m = 0.2 Wb
RFO	0.12 / $\Delta\varepsilon_\theta$=0	0.12 / $\Delta\varepsilon_\theta$=0
Extended-RFO	-0.08 / $\Delta\varepsilon_\theta$=0	-0.08 / $\Delta\varepsilon_\theta$=0

3.2.6 Test 6

As shown in Fig. 28, only the RFO was able to start the motor in presence of a 68% uncertainty in the flux linkage constant (φ_m = 0.1 Wb). Since starting without load was successful, the test was repeated in full load condition, and also in this case the performance was good. The results of Test 6 are summarized in Table 9.

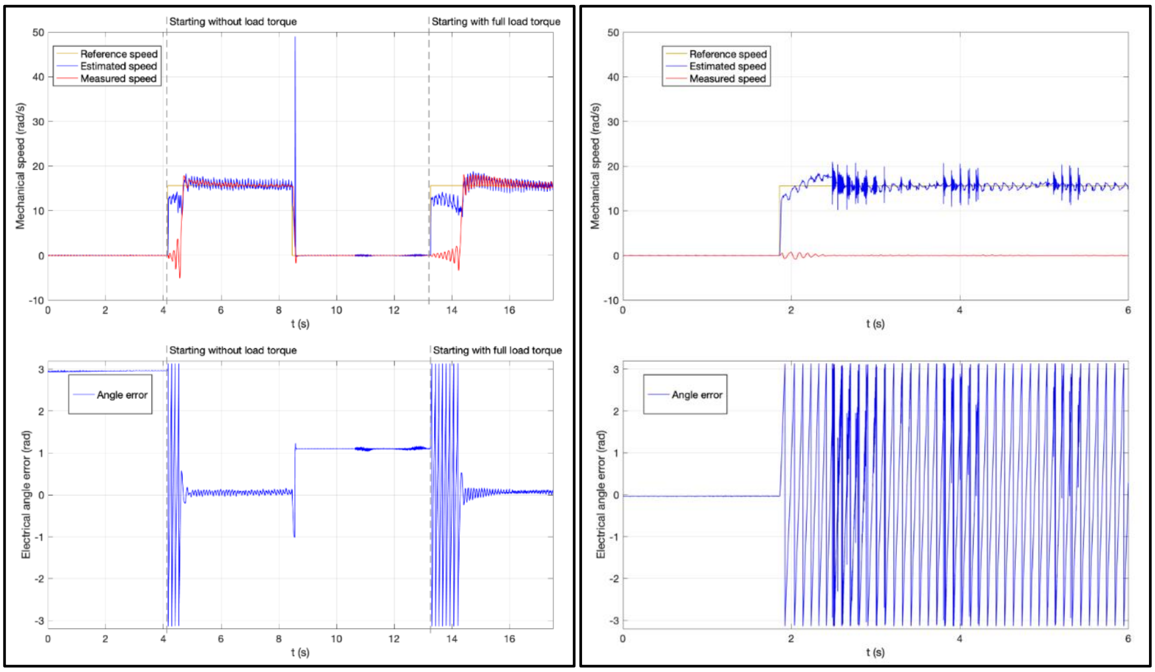

Fig. 28 (left) RFO (right) Extended-RFO. Speed and angle error during no-load starting at 3% of rated speed with a 68% variation in the flux linkage constant (Test6).

Table 9 Algorithm performances during Test 6

	Performance during starting with wrong flux value (φ_m = 0.1 Wb)
RFO	Successful
Extended-RFO	Not successful

3.3 Additional tests for RFO algorithm

Since in section 3.2 it was demonstrated that RFO algorithm is the most performing algorithm among the tested ones, several additional tests were carried out using RFO.

In particular, the Id management technique shown in section 2.6 was tested. Moreover, different speed steps, speed inversion with no-load, linear torque and constant torque were tested. Finally, the behaviour with the air-compressor test bench was analysed.

3.3.1 Tests with Id reference management technique

Reference, measured and estimated speed during transient from 180 rad/s to 5 rad/s with no-load and 29 Nm motor are shown in Fig. 29 (test without Id injection) and in Fig. 30 (the test with Id injection), figures taken from [55]. One can note the great improvement achievable with the proposed technique.

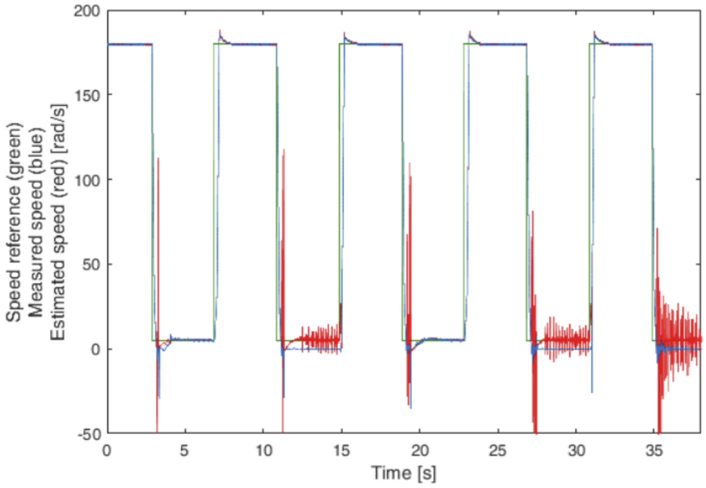

Fig. 29 Reference, measured and estimated speed during transient for 180 rad/s to 5 rad/s with no-load and 29 Nm motor, without Id injection

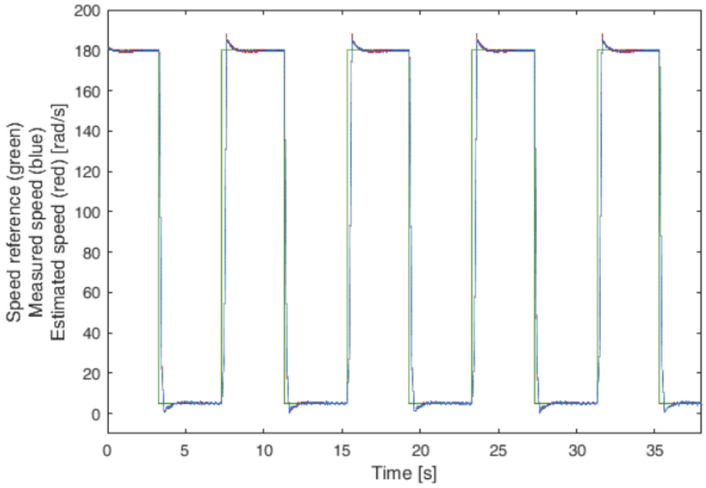

Fig. 30 Reference, measured and estimated speed during transient for 180 rad/s to 5 rad/s with no-load and 29 Nm motor, with Id injection

The benefits of the Id injection technique can be seen also in the test with speed transient from 180 rad/s to minus 180 rad/s with linear torque and 29 Nm motor. The reference, measured and estimated speed are reported in Fig. 31 (no Id injection), whereas the measured Id and Iq are shown in Fig. 32 (no Id injection). One can note that during the zero-speed crossing, the correct rotor position estimation is lost and therefore Id and Iq have high frequency components, as it can be noted in Fig. 32 left. This leads to current ripple and acoustic noise.

On the contrary, none of this problem can be noted in the test with Id injection, as it can be seen from speed plot in Fig. 33 and current plots in Fig. 34.

Please note that, since the Id injection demonstrates a great improvement, this technique will be used in all the tests shown from this point forward.

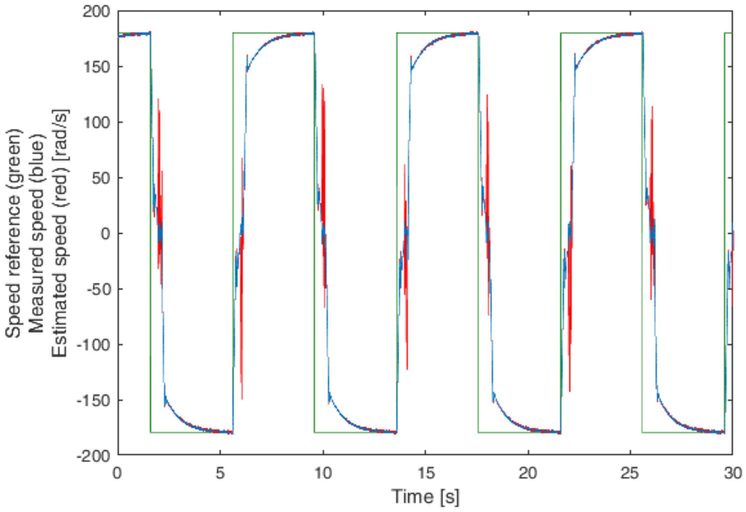

Fig. 31 Reference, measured and estimated speed during transient for 180 rad/s to -180 rad/s linear torque and 29 Nm motor, without Id injection

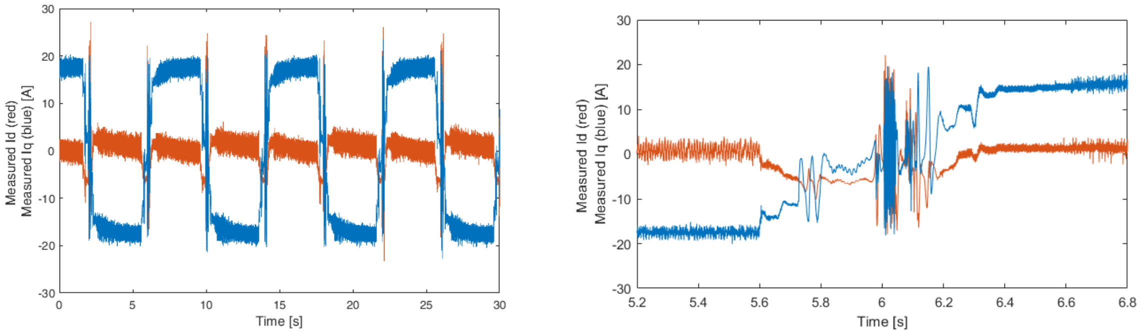

Fig. 32 Measured Id and measured Iq during transient for 180 rad/s to -180 rad/s linear torque and 29 Nm motor, without Id injection. (left) entire test (right) enlargement

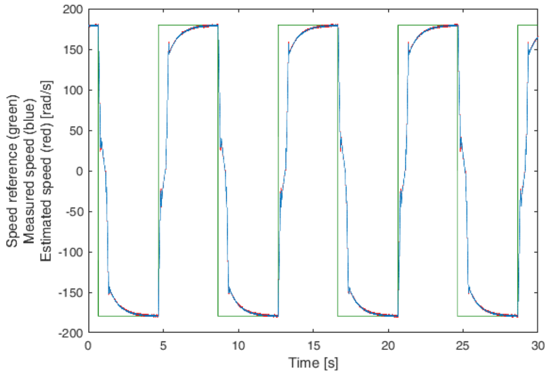

Fig. 33 Reference, measured and estimated speed during transient for 180 rad/s to -180 rad/s linear torque on 29 Nm motor, with Id injection

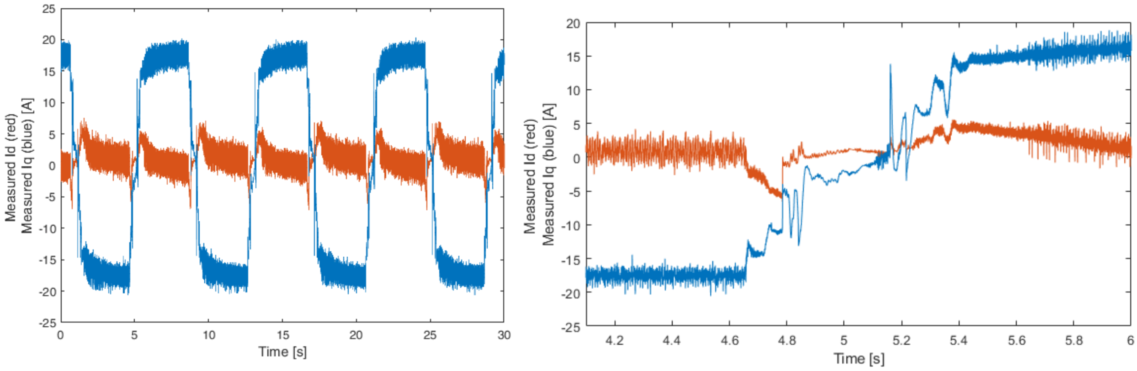

Fig. 34 Measured Id and measured Iq during transient for 180 rad/s to -180 rad/s linear torque and 29 Nm motor, with Id injection. (left) entire test (right) enlargement

3.3.2 RFO tests with additional speed and torque profiles

Additional tests were carried out with the RFO algorithm, in order to prove its validity in a wide range of working conditions. Motor starting with no-load, using the 2 Nm motor, with reference speed equal to 10 rad/s (2% of rated speed) and 180 rad/s (25% of rated speed), considering also speed inversion, is shown in Fig. 35 and same test is shown in Fig. 36 with constant torque, always with 2 Nm motor.

Additional tests were carried out also with the 29 Nm motor, considering motor starting from standstill to 180 rad/s (85% or rated speed), with no-load (Fig. 37) and linear torque, i.e., load torque proportional to motor speed, (Fig. 38).

All the tests showed a good behaviour of the RFO sensorless algorithm.

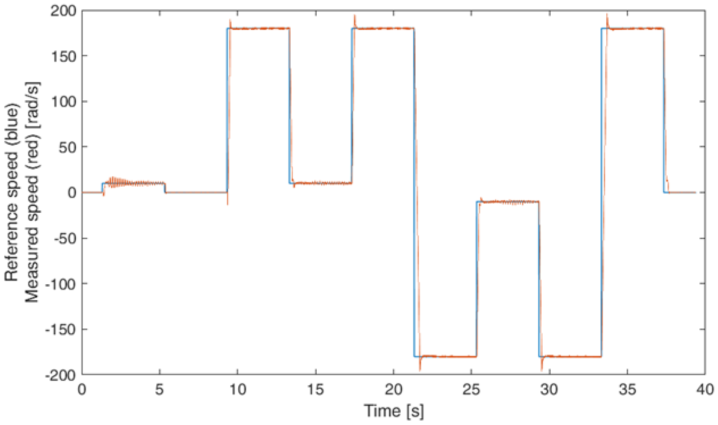

Fig. 35 0, 10, 180, -10, -180 rad/s speed steps with no-load and 2 Nm motor

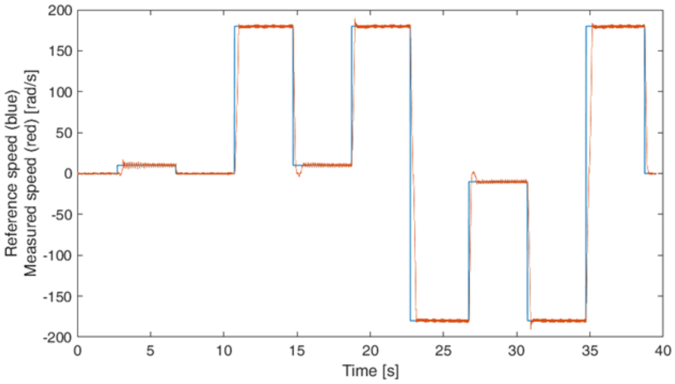

Fig. 36 0, 10, 180, -10, -180 rad/s speed steps with constant torque and 2 Nm motor

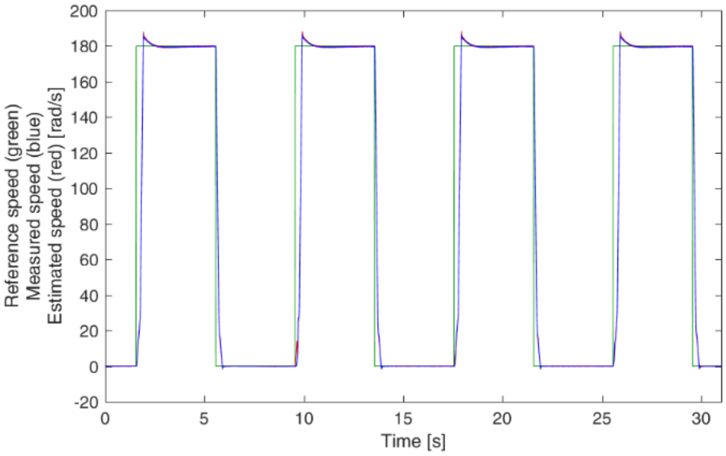

Fig. 37 Motor starting to 180 rad/s, no-load and 29 Nm motor

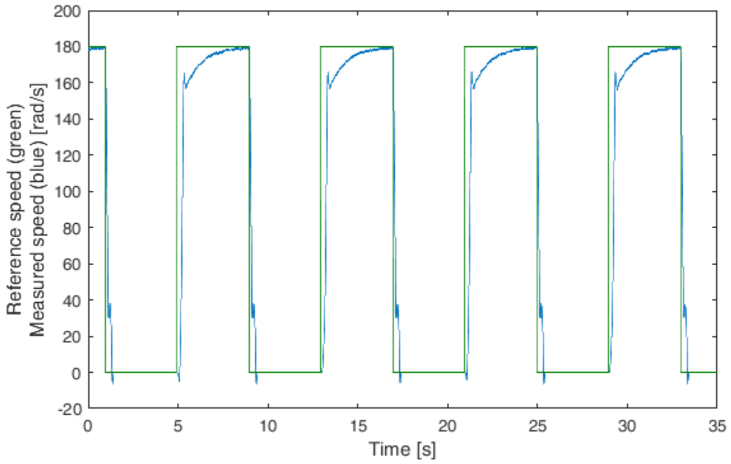

Fig. 38 Motor starting to 180 rad/s, linear torque and 29 Nm motor

3.3.3 RFO tests on air compressor test bench

The RFO was tested also on the air compressor test bench. Reference and measured speed are shown in Fig. 39. Speed steps from standstill to 10 rad/s (2.4% of rated speed) and 400 rad/s (95% of rated speed) were given as reference. As aforementioned, the compressor load is particularly demanding; as a matter of fact high torque is required at standstill and the torque is highly intermittent, as it can be noted in Fig. 40 where Iq (which is proportional to the electromagnetic torque) is plotted. Please note that the current is negative due to measurement conventions. Also in this test the proposed algorithm showed a good behaviour.

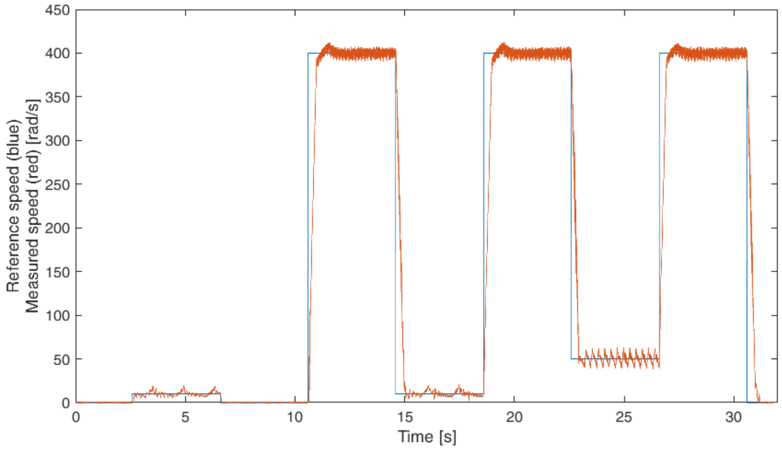

Fig. 39 0 rad/s, 10 rad/s and 400 rad/s speed steps with compressor test bench and 9.5 Nm motor

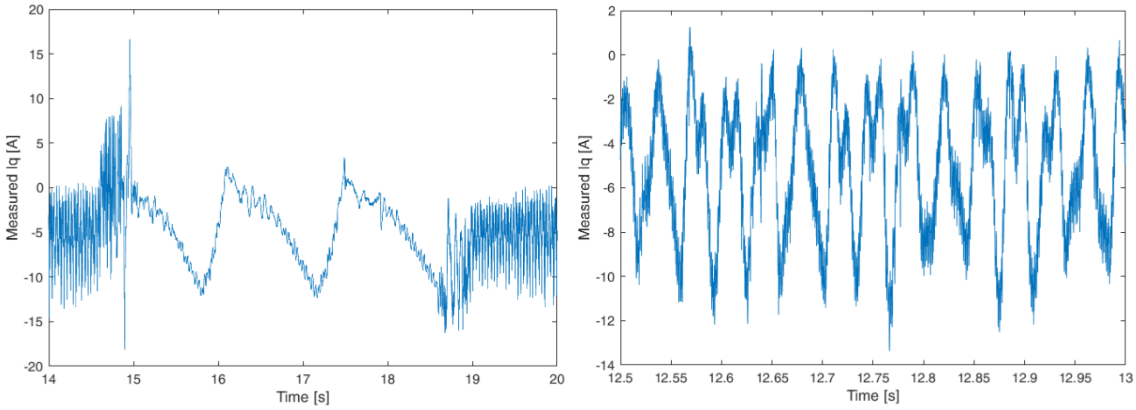

Fig. 40 Measured Iq with compressor test bench and 9.5 Nm motor, time axis is referred to the same test of Fig. 39

3.4 Self-commissioning technique

Self-commissioning technique consists in the drive ability of autotuning. Regarding the self-commissioning of RFO algorithm, stator resistance (R), stator inductance (L) and magnetic flux constant should be determined. Since the sensorless algorithm shown before modifies the initial magnet flux linkage value in order to match the real value, an approximated value for $\hat{\psi}_m$ can be derived directly from motor rated voltage and speed. Indeed, considering null currents and constant speed, from equations (2.4) one can obtain equation (3.2)

$$\hat{\psi}_m = \frac{V \cdot \sqrt{2/3}}{\omega \cdot p} \tag{3.2}$$

Where V is the rated voltage (phase-to-phase root-mean-square value), ω is the rated mechanical speed in rad/s and p is the number of pole pairs. Therefore, the self-commissioning algorithm has to identify the stator resistance (R) and the stator inductance (L). Observing equation (3.2) one can notice that R could be estimated injecting a constant voltage, whereas L injecting a sinusoidal high-frequency voltage, as shown in (3.3):

$$R = \frac{V_\alpha}{I_\alpha} \quad L = \frac{V_\alpha}{\omega I_\alpha} \tag{3.3}$$

Where V_α and I_α are the voltage and current components in the stationary Clarke transformation and ω is the voltage frequency in rad/s. ω has to be sufficiently high so that the voltage drop on stator resistance can be neglected. However, since during self-commissioning voltage is injected using the drive inverter, its nonlinearities have to be taken into account. In Fig. 41, inverter reference voltage V_α^* as a function of injected direct current I_α is shown; results were obtained with measurements on the 29 Nm motor. According to what presented in [99], stator resistance can be evaluated as the curve slope when V_α^* becomes linear (i.e. for

$i_\alpha > 5A$), using a linear regression approach. In Fig. 41 voltage error ΔU is also shown, which is defined as in equation (3.4):

$$\Delta U = V^*_\alpha - R \cdot I_\alpha \tag{3.4}$$

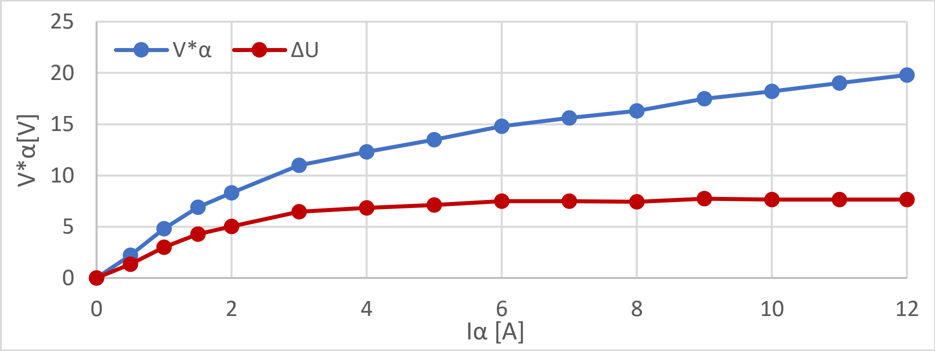

Fig. 41 and ΔU as a function of

Since voltage error becomes constant for $i_\alpha > 5A$, L can be estimated superimposing to the sinusoidal voltage in equation (9) a DC voltage so that instantaneous value of i_α is always above 5 A, as shown in [100]. In particular, current from 70% to 100% of motor rated current was injected to evaluate motor resistance and 85% DC current was injected with a 15% amplitude sinusoidal current superposed, so that instantaneous current was always above 70% of rated current. For this reason with the inverter used in the test, only motors with rated current above 7 A can be used with the self-commissioning algorithm. One has to note that the limit from which inverter voltage error becomes constant depends on inverter characteristics and was 5 A for the specific inverter used in this test.

Using a sensorless algorithm, motor parameters not only are used to perform the FOC, but also to estimate rotor position. For this reason parameter correct estimation using self-commissioning algorithm becomes a crucial point. Experimental tests demonstrated that the proposed sensorless algorithm is low sensitive to resistance error and to flux linkage constant (since the algorithm estimates the inductance correct value), therefore inductance value is the most critical parameter to be measured. The test bench with the coupled motor was used, both with the 29 Nm motor and the 2 Nm motor. For each motor six different working conditions were tested: motor starting up to 180 rad/s, motor starting up to 10 rad/s and speed reference variation between 180 rad/s and -180 rad/s, each of which both with constant rated torque and with no-load. For each condition, the minimum and the maximum value of motor inductance for which the motor can work in that specific condition (i.e. it can start and work without overcurrent protection intervention and without significant additional vibration) was evaluated. Inductance ranges in which motors can work in the various conditions are reported in Fig. 42 together with measured inductance and inductance value estimated with self-commissioning algorithm.

One can note that the inductance error range in which the sensorless control can work is significantly wider that the error of the self-commissioning technique, therefore the autotuning of the proposed sensorless control is validated.

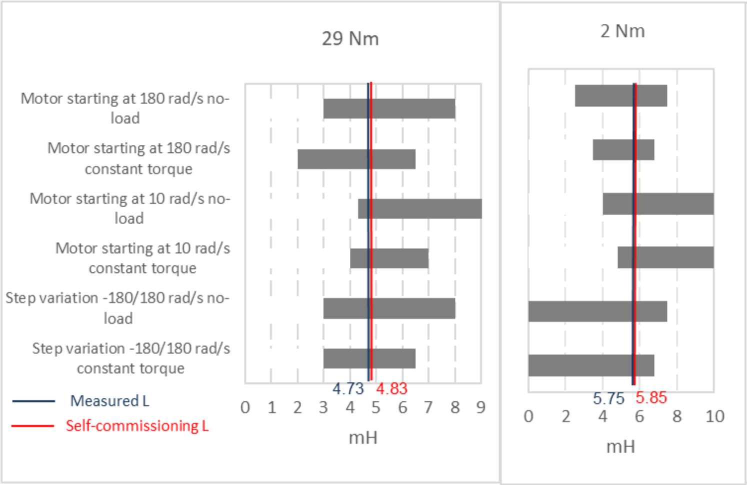

Fig. 42 Algorithm sensitiveness to inductance error

4 Industrial application with SPMSM

4.1 Experimental tests with PMC inverter on Petra Lab test benches

Since the results in section 3 were considered effective, the sensorless control was implemented on the inverter produced by PMC. The inverter is shown in Fig. 43. It has a 230 V three-phase input (133 V line-to-ground voltage) which leads to a 310 V DC-link. The 230V voltage is rectified by a diode bridge, thus the inverter is not able to fulfill regenerative braking on the grid. The rated power is 750W, therefore the rated current is about 1.9 A. An Infineon XMC4400-512 microcontroller is exploited for the control and current measures are carried out using shunt resistors. In order to avoid acoustic noise, the switching frequency is set to 20 kHz.

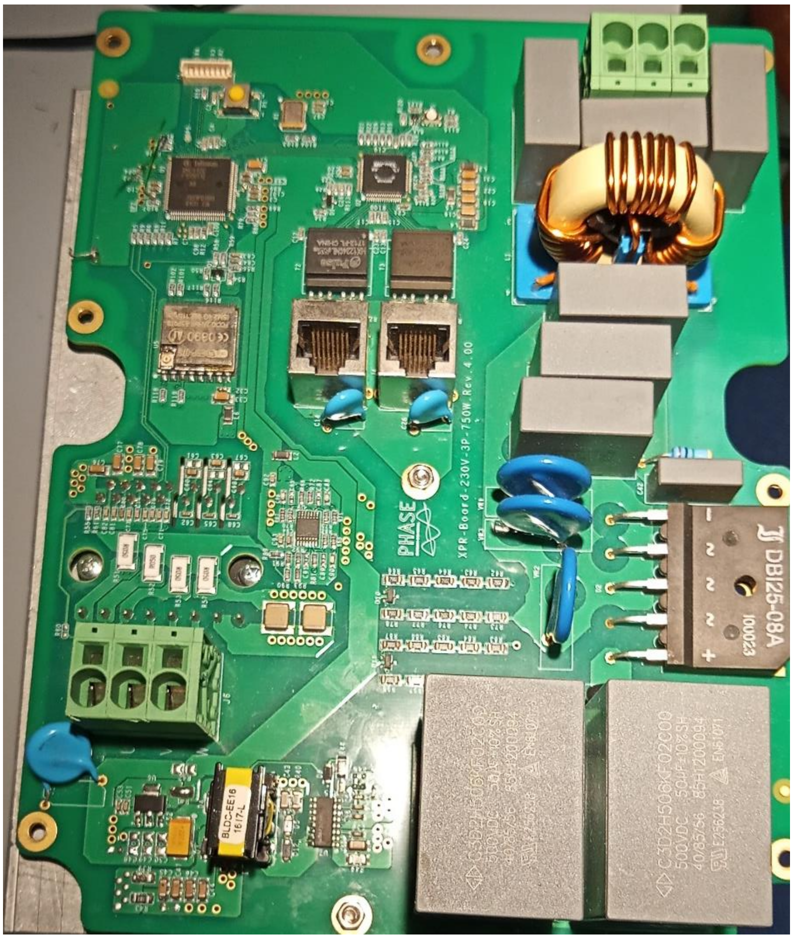

Fig. 43 PMC inverter

The RFO control algorithm was implemented in C code on the platform shown in Fig. 43.

The tests shown in section 3 were carried out using the same motor test benches but suppling the motor with the PMC inverter.

Since the rated current is about 1.9 A only the following tests were carried out:

- Test 1 of Section 3.2.1. The reference speed value was changed, in no-load conditions, from 0 to 20% of nominal speed in three consecutive steps: first it was set to 15.6 rad/s, which corresponds to 3% of the rated speed, then to 52 rad/s (10% of rated speed) and finally to 104 rad/s (20% of rated speed). Then, a rated load torque step was applied at 104 rad/s.

- Test 2 of Section 0. The motor was started from zero speed with constant rated torque applied, setting the reference speed to 3% of rated speed.
- Test 3 of Section 0. A load step from 0 to 50% of the rated torque was applied when the motor was running at 52 rad/s (10% of rated speed). Then, full torque was applied, and reduced to 50% again. When possible, full load torque was applied and removed directly.
- Test 4 of Section 3.2.4. An error in the stator inductance parameter was introduced at 52 rad/s with full load torque applied if possible. The inductance value was changed from 5.7 mH (its real value) to 3.0 mH, then to its real value again, and finally to 9.0 mH.
- Test 5 of Section 3.2.5. An error in the flux linkage constant was introduced at 52 rad/s with full load torque applied. First it was changed from 0.147 Wb (rated flux) to 0.1 Wb, then to 0.147 Wb again and finally to 0.2 Wb.
- Test 6 of Section 3.2.6. A no-load starting was performed with the flux parameter set to 0.1 Wb (68% of its real value), setting the reference speed to 3% of rated speed. If successful, a full-load starting test was then carried out.
- Test in Fig. 35. Motor starting with no-load, with reference speed equal to 10 rad/s (2% of rated speed) and 180 rad/s (25% of rated speed), considering also speed inversion
- Test in Fig. 36. Motor starting with constant torque, using the 2 Nm motor, with reference speed equal to 10 rad/s (2% of rated speed) and 180 rad/s (25% of rated speed), considering also speed inversion
- Test in Fig. 39. Air compressor load, with reference speed equal to 2.4%, 10% and 95%. The pressure of the compressor was reduced, in comparison to the results shown in section 3.3.3, in order to have a resistive torque that matched the inverter maximum current.

Since the control platform of PMC did not have a resolver/encoder interface, it was not possible to record experimental results as for the test carried out with Dspace MicroLabBox. Therefore the test were carried out only qualitatively, i.e., it was verified that the motor worked properly and that the correct speed was reached measuring stator current frequency.

All the tests listed above show positive results, confirming the correct implementation of the RFO sensorless control in PMC inverter.

4.2 Experimental tests with PMC inverter on a six meter diameter industrial fan with PNET SMPSM

After the tests described in section 4.1 were carried out, the PMC inverter was used to supply a SPMSM produced by PNET and coupled with a six meter diameter fan, as shown in Fig. 44. The motor parameters are shown in Table 10.

Fig. 44 Six meter diameter Fan supplied by Phase Motion Control inverter with RFO sensorless observer

Table 10 Motor parameter for six diameter fan

Parameter	Value
Rated speed at 230 V	52 rpm
Pole pairs	35
Rated torque at 230 V	4.0 Nm
Load inertia (approximately)	35 kgm^2
Mechanical time constant (approximately)	8.5 s

4.2.1 Rotating current-loop for fan starting

As it is possible to note from Table 10, the fan application is characterized by a very low torque-to-inertia ratio. Therefore, differently from application with a typical torque-to-inertia ratio (as the ones shown in section3), during the starting phase, the motor work near zero speed for a long time. For this reason the RFO algorithm is not able to start the motor, since it cannot estimate the angle properly at standstill.

To solve this problem, an hybrid control was developed. With the proposed hybrid control the motor starts with a current control loop, with the current vector rotating in open loop and then a soft transition to FOC is carried out.

The working principle during the fan starting is shown in Fig. 45, where motor reference speed ($\omega_{reference}$), Id reference (Id_{ref}) and angle reference (Ang_{ref}) are shown. The angle reference variable determines whether the open loop angle is used or if the angle provided by the sensorless control is exploited. Namely, if angle reference is equal to 0, the open loop angle (θ_{OL}) is used, which is calculated as in equation (4.1). On the contrary, if angle reference is equal to 1, the estimator angle (θ_{est}) is used. While the angle reference value is between 0 and 1, a weighted average is carried out to calculate the rotor angle (θ_r) as shown in equation (4.2)

$$\theta_{OL} = \int \omega_{reference}\, dt \tag{4.1}$$

$$\theta_r = Ang_{ref}\theta_{est} + (1 - Ang_{ref})\theta_{OP} \tag{4.2}$$

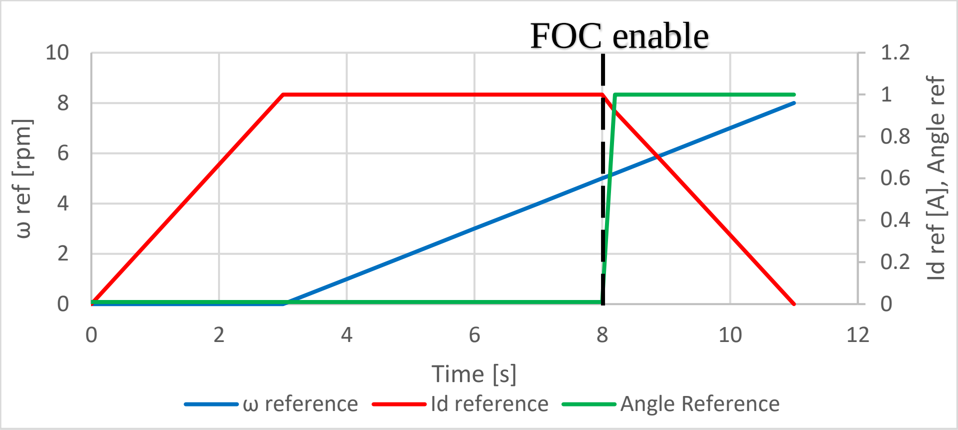

Fig. 45 Speed [rpm], Id reference [A] and angle reference during fan starting.

While the motor is at standstill a Id_{ref} ramp of 3s is injected to about 50% of rated current. Since the initial rotor position is unknown, the fan motor will move and align with the injected current vector. In order to avoid oscillation and noise, the current ramp should be sufficiently smooth and therefore 3s of ramp was imposed. When 1A of Id_{ref} is reached, $\omega_{reference}$ start to increase and therefore the current vector rotates according to equation (4.1). During this phase, the FOC controllers are kept disactivated but the sensorless estimator is activated. When $\omega_{reference}$ reaches 5 rad/s, the FOC controllers are activated, Ang_{ref} increase at the unitary value in 100 ms and the rotor angle is given by equation (4.2). The transition from open-loop to FOC takes only 100 ms, however Id_{ref} decreases in 3s, in order to avoid oscillations and noise.

4.2.2 DC bus voltage control

Since the inverter used in this application has a diode bridge to rectify the AC input, DC-bus voltage may increase significantly if a proper control is not developed. Indeed, during decelerations, the FOC control imposes a negative Iq current (or a positive Iq current if the speed is negative) and the kinetic energy is converted into electrical energy which charges the DC-bus. If the DC-bus voltage is not properly controlled the overvoltage protection intervenes. To avoid this, when the voltage raises above a certain threshold, the braking current Iq should be limited. Please note that motor losses and inverter losses can be exploited to perform an electric braking even if a regenerative braking on the grid is not possible in this application. The aim of the DC-bus voltage control is to exploit the electric braking without causing overvoltage protection intervention.

On the other hand, during voltage dips, it is useful to exploit the kinetic energy to charge the DC-bus. To do that the fan can be temporarily braked during the voltage dip in order to keep the drive switched on.

To exploit both these functions the control shown in Fig. 46 was implemented. Vdc is the measured DC-bus voltage, Vdc_high is the threshold above which the control intervene to reduce the electric braking, Vdc_low is the threshold below which the control brakes the fan to charge the DC-bus, Iq_min and Iq_max are the speed

PI limits (which are modified by the Vdc control), Iq*_min and Iq*_max are the default PI limits when the Vdc control does not intervene, Kp_high and Kp_low are the gain of the Vdc proportional control.

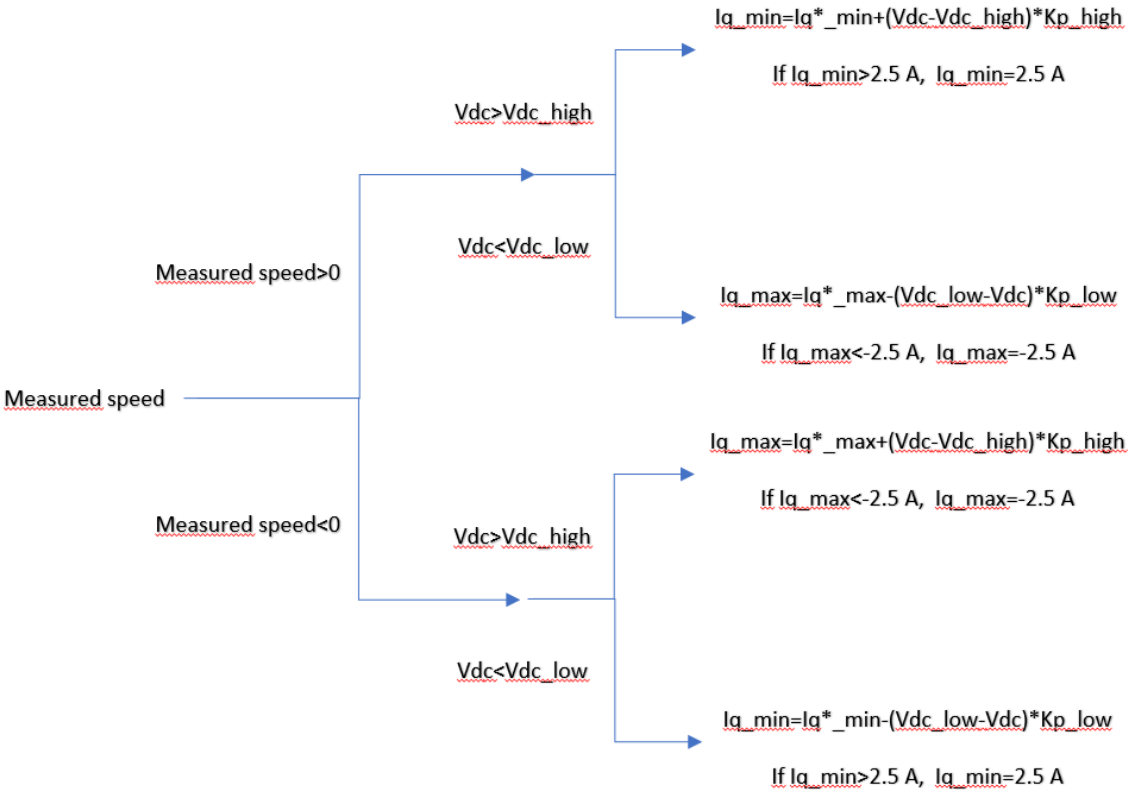

Fig. 46 Vdc control scheme

4.2.3 Experimental tests

Since the fan application did not have any position sensors, just a qualitative analysis could be developed.

In order to verify that the fan reached the desired speed, the stator current frequency was measured. The following test were carried out:

- Startup from standstill to rated speed clockwise (52 rpm).
- Startup from standstill to minimum operating speed clockwise (10 rpm).
- Deceleration from rated speed clockwise (52 rpm) to minimum operating speed clockwise (10 rpm).
- Startup from standstill to rated speed counterclockwise (-52 rpm).
- Startup from standstill to minimum operating speed counterclockwise (-10 rpm).
- Deceleration from rated speed counterclockwise (-52 rpm) to minimum operating speed counterclockwise (-10 rpm).
- Speed inversion from rated speed clockwise (52 rpm) to rated speed counterclockwise (-52 rpm)
- Speed inversion from rated speed counterclockwise (-52 rpm) to rated speed clockwise (52 rpm)
- Speed inversion from rated speed clockwise (52 rpm) to minimum operating speed counterclockwise (-10 rpm).

- Speed inversion from rated speed counterclockwise (-52 rpm) to minimum operating speed clockwise (10 rpm).
- Speed inversion from minimum operating speed clockwise (10 rpm) to minimum operating speed counterclockwise (-10).
- Speed inversion from minimum operating speed counterclockwise (-10 rpm) to minimum operating speed clockwise (10).
- Supply loss for 2 second at rated speed clockwise (52 rpm)
- Supply loss for 2 second at rated speed counterclockwise (-52 rpm)
- Supply loss for 2 second at minimum operating speed clockwise (10 rpm)
- Supply loss for 2 second at minimum operating speed counterclockwise (-10 rpm)
- Supply loss for 5 second at rated speed clockwise (52 rpm)
- Supply loss for 5 second at rated speed counterclockwise (-52 rpm)
- Supply loss for 5 second at minimum operating speed clockwise (10 rpm)
- Supply loss for 5 second at minimum operating speed counterclockwise (-10 rpm)

Each test was repeated 30 times, in order to verify the robustness of the algorithm.

The proposed control showed a good behaviour in all the tests and therefore the algorithm for the industrial fan application was validated.

5 Sensorless control for a high-power EESM

5.1 Sensorless observer and Simulink model for EESM

5.1.1 Sensorless observer for EESM

In the previous sections, the application of the RFO control to SPMSMs was presented. Differently from the PMSM, the EESM can vary the rotor flux modifying the field voltage. For this reason, the FOC of PMSM usually uses the rotor angle to perform the transformations of axes, in order to maximize the torque, whereas the FOC for EESM usually uses the stator flux angle to perform the transformations of axes. Indeed, using the stator flux angle the motor works at unitary power factor and the current is minimized. This aspect is particularly interesting for high-power motors, where a reduction of motor current implies a reduction in the drive sizing. Using the stator flux angle for the transformation, causes a flux-weakening, which would be a drawback in PMSM, but that is negligible with EESM since the flux can be adjusted modifying the field current. Since the stator flux angle is required in FOC control for EESM, the sensorless algorithm should be modified in order to estimate the stator flux rather than the rotor flux.

The stator flux is given by equation (5.1), therefore a stator flux observer can be derived from the rotor flux observer in equations (2.33) simplify neglecting the inductance voltage drop. As a consequence, the observer shown in equations (5.2) can be exploited.

$$\dot{x}_{\alpha\beta} = v_{\alpha\beta} - Ri_{\alpha\beta} \tag{5.1}$$

$$\begin{cases} \dot{q}_{\alpha\beta} = v_{\alpha\beta} - Ri_{\alpha\beta} + \Gamma_1\left(\left\|\xi_{\alpha\beta}\right\|^2 - \varphi_m^2\right), & q_{\alpha\beta}(0) = [0,\ 0]^T \\ \dot{\xi}_{\alpha\beta} = \Gamma_2\Omega(q_{\alpha\beta})\left(y(q_{\alpha\beta}) - \Omega_{\alpha\beta}(q_{\alpha\beta})^T\,\xi_{\alpha\beta}\right), & \xi_{\alpha\beta}(0) = \varphi_m\left[\cos(\theta_0);\sin(\theta_0)\right] \\ y(q_{\alpha\beta}) = \dfrac{-\alpha p}{p+\alpha}\left\|q\right\|^2, & y(0) = 0 \\ \Omega_{\alpha\beta}(q_{\alpha\beta}) = \dfrac{\alpha p}{p+\alpha}2q_{\alpha\beta}, & \Omega_{\alpha\beta}(0) = [0,0]^T \\ x_{\alpha\beta} = q_{\alpha\beta} + \xi_{\alpha\beta} & \\ \hat{\theta} = atan2\left(\dfrac{x_\beta}{x_\alpha}\right) & \end{cases} \tag{5.2}$$

5.1.2 Initial position estimation

As aforementioned, in high power applications, the high voltage injection leads to unsustainable torque ripple. However, the sensorless approach shown in section 5.1.1 cannot work at standstill and therefore a different approach should be designed to determine the initial rotor position (θ_0), which is necessary to initialize equations (5.2). Indeed, in high power applications, it is necessary to know the initial rotor angle in order to avoid oscillations during the motor starting, whereas the effects of this oscillation is negligible in low power applications, therefore the initial rotor angle is not determined in the case of PMSM shown in section 2.4.

When the rotor is excited, the increasing rotor flux induces a variation in stator currents, even if the motor is at standstill. Since, differently from PMSMs, the rotor flux can be controlled independently, a step rotor voltage variation can be performed. In this way, as shown in [101], it is possible to estimate the rotor position exploiting the stator current measures. A low-pass filter can be applied to the current measures in $\alpha\beta$ domain, obtaining two current measures with a low noise ($I_{\alpha\_LPF}, I_{\beta\_LPF}$). The initial rotor angle can be then estimated as in equation (5.3). Please note that a positive voltage step variation is considered and, therefore, the opposite of stator currents should be used in equation (5.3).

$$\theta_0 = atan2\left(-i_{\beta\_LPF};-i_{\alpha\_LPF}\right) \tag{5.3}$$

The proposed algorithm is simple and it does not cause torque ripple, since the stator windings are not supplied during the rotor voltage step variation. Since one of the main problem of this technique is the measure noise, it is difficult to validate its effectiveness with simulation. For this reason, simulations are used to verify the sensorless observer sensitiveness toward initial angle error, whereas the initial angle estimation technique is validated with experimental results only.

5.1.3 Simulink model for EESM

The observer shown in equations (5.2) was tested on a Simulink model of a high-power EESM. The Simulink model of the EESM was provided by Nidec ASI and is shown in Fig. 47. The motor model was validated by Nidec ASI in several years of experience, comparing the behaviour obtained via simulations with the behaviour in the industrial applications.

In this study, a 13.8 MW EESM was considered. The motor parameters are reported in Table 11.

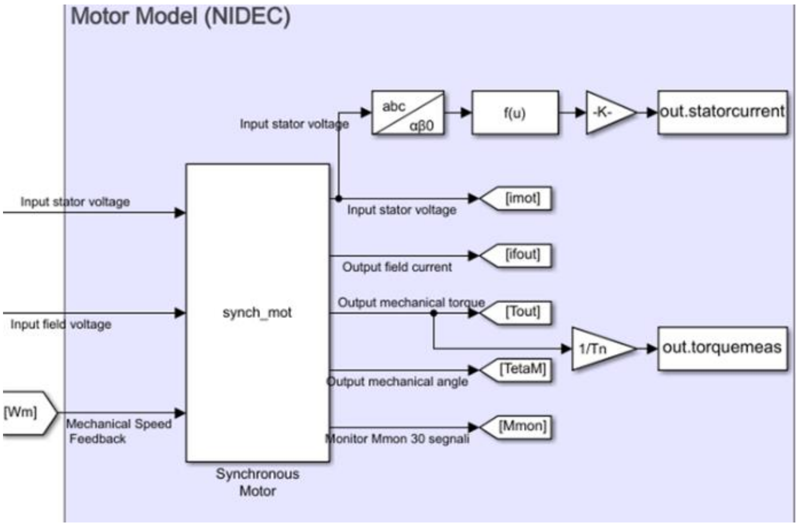

Fig. 47 EESM Simulink model provided by Nidec ASI

Table 11 13.8 MW EESM parameters

Name	Description	Value	UM
Excitation Type	Defines the type of excitation for the wound field circuit	Slip Rings	
Rated Power	Motor rated power	13810	kW
Poles	Number of motor poles	4	
Rated Voltage	Motor RMS rated voltage (Vn)	6600	V
Rated Current	Motor RMS rated current (In)	1230.2	A
Rated Speed	Motor rated speed	1800	rpm
Rated Field Voltage	Motor DC field voltage at rated speed and no-load (Vf0)	33	V
Rated Field Current	Motor DC field current at rated speed and no-load (If0)	213	A
Max Current Limit	Motor RMS current limit and threshold for the Max Current alarm	1845.3	A
Max Speed	Motor absolute maximum operative speed (1 pu)	2400	rpm
R Series	Any resistance connected in series with the motor	0.0001	Ohm
L Series	Any inductance connected in series with the motor	0.00079	H
Rsd (Rad)	Stator resistance on d axis (usually Rsd=Rsq=Ra)	0.0087	Ohm
Rsq (Raq)	Stator resistance on q axis	0.0087	Ohm
Rrd (Rkd)	Rotor (damping cage) resistance on d axis	0.055	Ohm
Rrq (Rkq)	Rotor (damping cage) resistance on q axis	0.045	Ohm
Lad Saturated	Magnetizing saturated stator inductance d axis	0.013475	H
Laq Saturated	Magnetizing saturated stator inductance q axis	0.011831	H
Lad Linear	Magnetizing linear stator inductance d axis	0.013475	H
Laq Linear	Magnetizing linear stator inductance q axis	0.011748	H
Llsd	Leakage stator inductance d axis	0.000633	H
Llsq	Leakage stator inductance q axis	0.000633	H
Llrd (Llkd)	Rotor (damping cage) leakage inductance on d axis	0.000973	H
Llrq (Llkq)	Rotor (damping cage) leakage inductance on q axis	0.001316	H
Rf	Field winding resistance (referred to stator)	0.0046	Ohm
Lf	Field winding leakage inductance	0	H
Sync Transform	Stator-field transformation coefficient	4.57	
Rated Frequency	Motor rated frequency	60	Hz
Max Frequency	Motor frequency at the maximum speed	66.67	Hz
Rated Torque	Motor rated torque	73264.32	Nm
Base Impedance	Base impedance (Zn=Vn/In)	3.097473	Ohm
Motor & Load Inertia	Motor and load inertia	842	Kg m^2
Inertia Time Constant	Base inertial time constant	~2.166	s

5.1.4 FOC for EESM

A FOC control was realized in MATLAB/Simulink environment. In particular, the following control loops were developed:

- Id current loop → Inputs: reference Id (which is set to zero) and measured Id. When the controller is reset, Vd=0. The PI controller parameters are P_Vd, I_Vd, max_Vd, min_Vd.
- Iq current loop → Inputs: reference Iq (output of speed controller) and measured Iq. A feed-forward is used in which $V_{q\_FF} = R_{sq} I_{q\_ref} + \omega_{el} \varphi_{rated}$, where V_{q_FF} is the feed-forward voltage, I_{q_ref} is the reference Iq, ω_{el} is the measured electrical speed and φ_{rated} is the rated stator flux. When the controller is reset, Vq=0. The PI controller parameters are P_Vq, I_Vq, max_Vq, min_Vq.
- Speed loop → Inputs: reference speed and measured speed. When the controller is reset, the output (reference Iq) is equal to zero. The PI controller parameters are P_Iq, I_Iq, max_Iq, min_Iq.

A field voltage control was realized in MATLAB/Simulink environment. In particular, the following control loops were developed:

- Field current (If) loop → Inputs: reference If (output of stator flux loop) and measured If. A feed-forward is used in which $V_{f\_FF} = \frac{I_{f\_ref} R_f}{n}$, where V_{f_FF} is the feed-forward field voltage, I_{f_ref} is the reference If and n is the stator-field transformation coefficient. When the controller is reset, $V_f = V_{f\_ref}$, where V_{f_ref} is a constant. The PI controller parameters are P_Vf, I_Vf, max_Vf, min_Vf.
- Stator flux loop → Inputs: reference flux (output of stator voltage loop) and estimated flux. . The PI controller parameters are P_If, I_If, max_If, min_If.
- Stator voltage loop → Inputs: rated stator voltage (peak line-to-ground value) and measure stator voltage ($V_s = \sqrt{V_d^2 + V_q^2}$). The PI controller parameters are P_flux, I_flux, max_flux, min_flux.

The FOC control was implemented in discrete time in Simulink, therefore the estimator filters and the PLL low pass filter were discretized. The estimator filter discretization is shown in equation (5.4) and α is defined in equation (5.5), whereas the PLL low-pass filter discretization in shown in equation (5.6). T_c is the sampling time, f_{cutHPF} is the cut-off frequency of the estimator high-pass filter and f_{cutPLL} is the cut-off frequency of the PLL low-pass filter.

$$\frac{\alpha p}{p+\alpha} \rightarrow \frac{\alpha(z-1)}{z-(1-\alpha T_c)} \tag{5.4}$$

$$\alpha = 2\pi f_{cutHPF} \tag{5.5}$$

$$\frac{2\pi f_{cutPLL} T_c}{z-(1-2\pi f_{cutPLL} T_c)} \tag{5.6}$$

The FOC control parameters and the estimator parameters usee to perform simulations are reported in Table 12.

Table 12 EESM sensorless FOC parameters

Parameter description	**Parameter acronym and value**
Field current PI proportional gain	P_Vf=20;
Field current PI integral gain	I_Vf=500;
Field current PI upper saturation	max_Vf=500;
Field current PI lower saturation	min_Vf=0;
Initial field voltage reference	Vf_reset=80;
Flux PI proportional gain	P_If=200;
Flux PI integral gain	I_If=900;
Flux PI upper saturation	max_If=4000;
Flux PI lower saturation	min_If=0;
Initial field current reference	Ifinit=400;
D-axis current PI proportional gain	P_Vd=1;
D-axis current PI integral gain	I_Vd=40;
D-axis current PI upper saturation	max_Vd=vsn*sqrt(2/3)*1.2;
D-axis current PI lower saturation	min_Vd=-vsn*sqrt(2/3)*1.2;
Q-axis current PI proportional gain	P_Vq=1;
Q-axis current PI integral gain	I_Vq=40;
Q-axis current PI upper saturation	max_Vq=vsn*sqrt(2/3)*1.2;
Q-axis current PI lower saturation	min_Vq=-vsn*sqrt(2/3)*1.2;
Voltage PI proportional gain	P_flux=0.0002;
Voltage PI integral gain	I_flux=0.01;
Voltage PI upper saturation	max_flux=0;
Voltage PI lower saturation	min_flux=-20;
Omega PI proportional gain	P_Iq=200;
Omega PI integral gain	I_Iq=1000;
Omega PI upper and lower limit	Imax=isn*sqrt(2)*1.5;
Inductance	L=0;
Gamma1 gain	gamma1=1.5e-4;
Gamma2 gain	gamma2=1.5e-5;
Gamma2 reduction in flux weaking	ridgamma2=0.1;
Id control (1-> Id control, 0-> Idref=0)	Idref=0;
Sample time	sampletime=820e-6;
Estimator filter gain (α)	alpha=94.25;
Kp PLL	Kp_PLL=800;
Ki PLL	Ki_PLL=10000;
PLL low pass filter cut-off frequency [Hz]	Fcut_PLL=16;

5.2 Simulation results for sensorless control of high power EESM

The Simulink model for the 13.8 MW EESM presented in section 5.1.2, together with the sensorless FOC presented in 0 was used to perform several tests. Eleven different tests were defined, together with Nidec ASI engineers, which correspond to the most frequent and critical conditions for the considered application:

- Test 1 → Motor starting with no-load to base speed (1 p.u.) with a 10s ramp, after 2s 0.8 p.u. load step, after 2s back to no-load and then -0.8 p.u. load step. No parameter uncertainties.
- Test 2 → Motor starting with no-load to base speed (1 p.u.) with a 10s ramp, after 2s 0.8 p.u. load step, after 2s back to no-load and then -0.8 p.u. load step. Parameter uncertainty Rs=150%.
- Test 3 → Motor starting with no-load to base speed (1 p.u.) with a 10s ramp, after 2s 0.8 p.u. load step, after 2s back to no-load and then -0.8 p.u. load step. Parameter uncertainty Rs=50%.
- Test 4 → Motor starting with no-load to base speed (1 p.u.) with a 10s ramp, after 2s 0.8 p.u. load step, after 2s back to no-load and then -0.8 p.u. load step. Parameter uncertainty initial stator flux=50%.
- Test 5 → Motor starting with no-load to 0.1 p.u. in 1s ramp, after 2s 0.8 p.u. load step, after 2s acceleration until maximum speed (1.33 p.u.) with a 12.33s ramp, after 2s load step to 0 p.u. No parameter uncertainties.
- Test 6 → Motor starting with no-load to 0.1 p.u. in 1s ramp, after 2s 0.8 p.u. load step, after 2s acceleration until maximum speed (1.33 p.u.) with a 12.33s ramp, after 2s load step to 0 p.u. Parameter uncertainty Rs=50%.
- Test 7 → Motor starting with no-load to 0.1 p.u. in 1s ramp, after 2s 0.8 p.u. load step, after 2s acceleration until maximum speed (1.33 p.u.) with a 12.33s ramp, after 2s load step to 0 p.u. Parameter uncertainty Rs=50% and initial rotor angle with 90° electrical angle.
- Test 8 → Motor starting with 0.8 p.u. load to 0.1 p.u. speed with 1s ramp, after 4s deceleration to minus 0.1 p.u. with a 2s ramp, after 4s back to standstill. No parameter uncertainties.
- Test 9 → Motor starting with 0.8 p.u. load to 0.1 p.u. speed with 1s ramp, after 4s deceleration to minus 0.1 p.u. with a 2s ramp, after 4s back to standstill. Parameter uncertainty Rs=50%.
- Test 10 → Motor starting with 0.8 p.u. load to 0.1 p.u. speed with 1s ramp, after 4s deceleration to minus 0.1 p.u. with a 2s ramp, after 4s back to standstill. Parameter uncertainty Rs=50% and initial rotor angle with 90° electrical angle.
- Test 11 → Motor starting with 0.8 p.u. load to 0.1 p.u. speed with 1s ramp, after 4s deceleration to minus 0.1 p.u. with a 2s ramp, after 4s back to standstill. Parameter uncertainty Rs=50% and initial rotor angle with 30° electrical angle.
- Test 12 → Motor starting with 0.8 p.u. load to 0.1 p.u. speed with 1s ramp, after 4s deceleration to minus 0.1 p.u. with a 2s ramp, after 4s back to standstill. Parameter uncertainty Rs=50% and initial rotor angle with -90° electrical angle.
- Test 13 → Motor starting with 0.8 p.u. load to 0.03 p.u. speed with a 0.3s ramp, after 4s deceleration to minus 0.03 p.u. with a 0.6s ramp, after 4s back to standstill. Parameter uncertainty Rs=50%.

In the following simulation results are shown for each test. Please note that in the torque plot, the Reference torque is intended as the Iq reference value. Therefore, it coincides with the reference torque in normal operation, whereas it is higher than the reference torque in the flux-weakening region.

5.2.1 Test 1

Motor starting with no-load to base speed (1 p.u.) with a 10s ramp, after 2s 0.8 p.u. load step, after 2s back to no-load and then -0.8 p.u. load step. No parameter uncertainties.

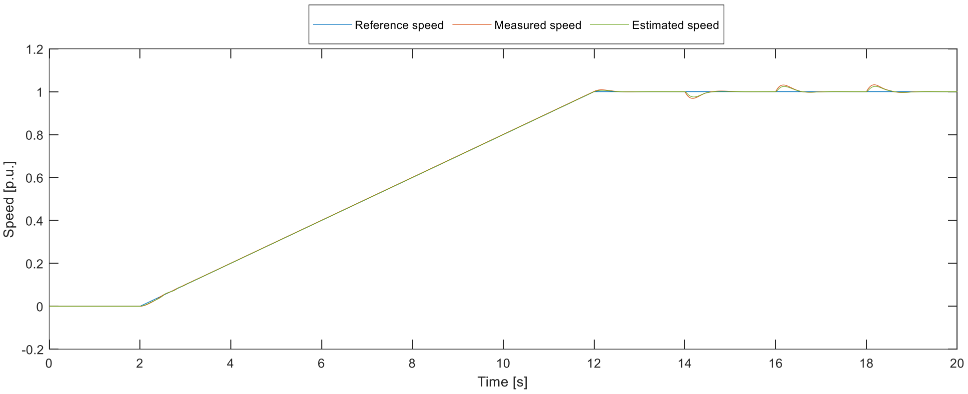

Fig. 48 Reference speed, measured speed and estimated speed. Sensorless FOC for EESM, test 1.

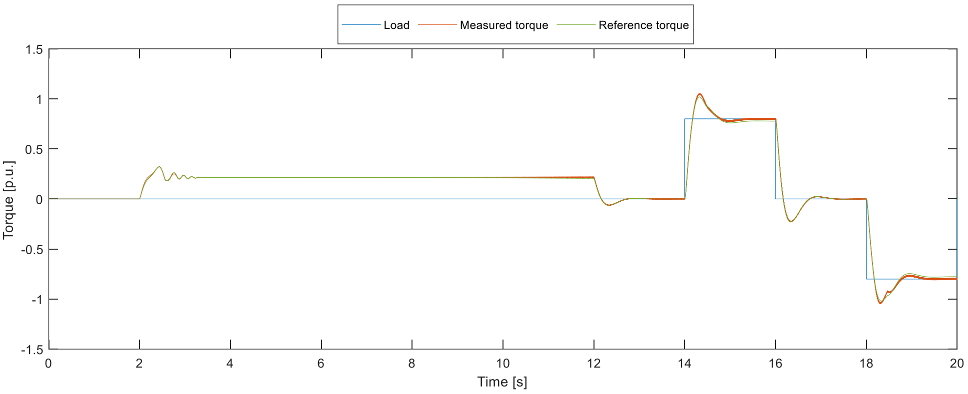

Fig. 49 Load, measured torque and reference torque. Sensorless FOC for EESM, test 1.

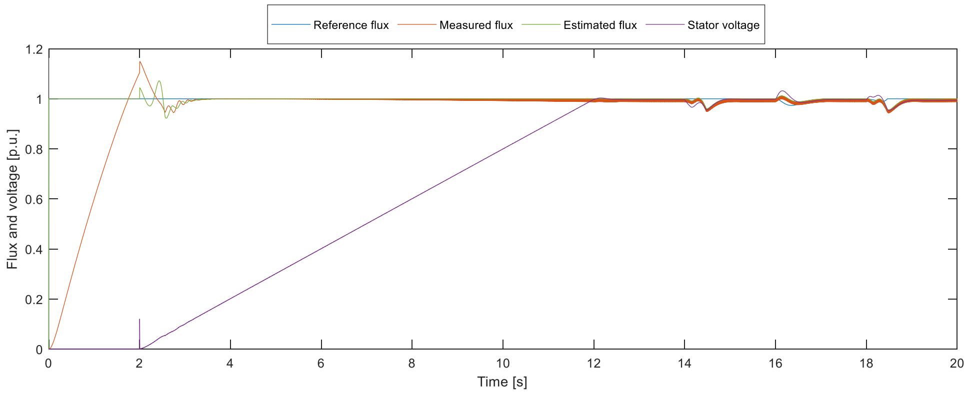

Fig. 50 Reference flux, measured flux, estimated flux and stator voltage. Sensorless FOC for EESM, test 1.

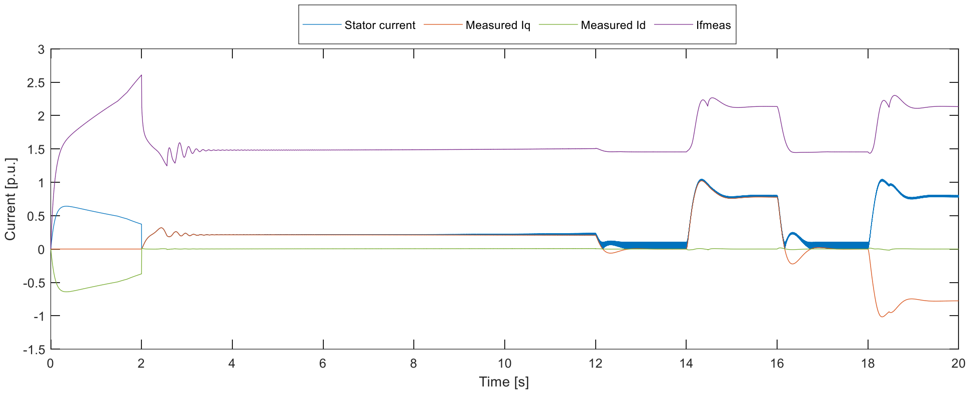

Fig. 51 Stator current, measured Iq, measured Id and measured If. Sensorless FOC for EESM, test 1.

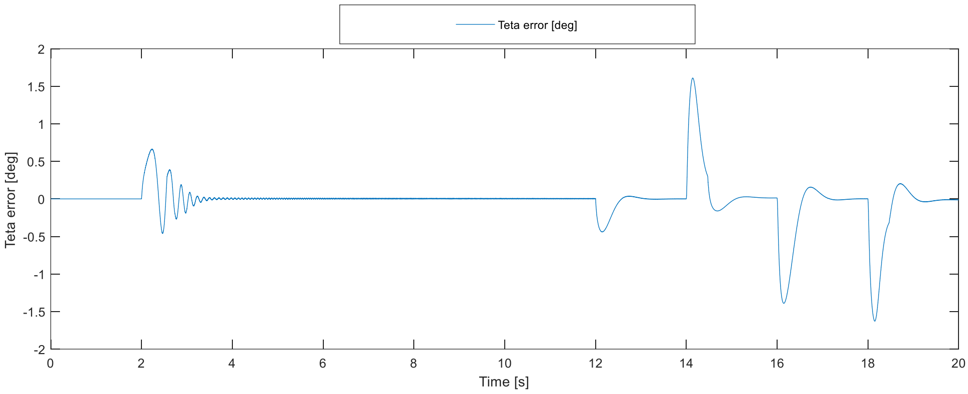

Fig. 52 Stator flux angle error. Sensorless FOC for EESM, test 1.

5.2.2 Test 2

Motor starting with no-load to base speed (1 p.u.) with a 10s ramp, after 2s 0.8 p.u. load step, after 2s back to no-load and then -0.8 p.u. load step. Parameter uncertainty Rs=150%.

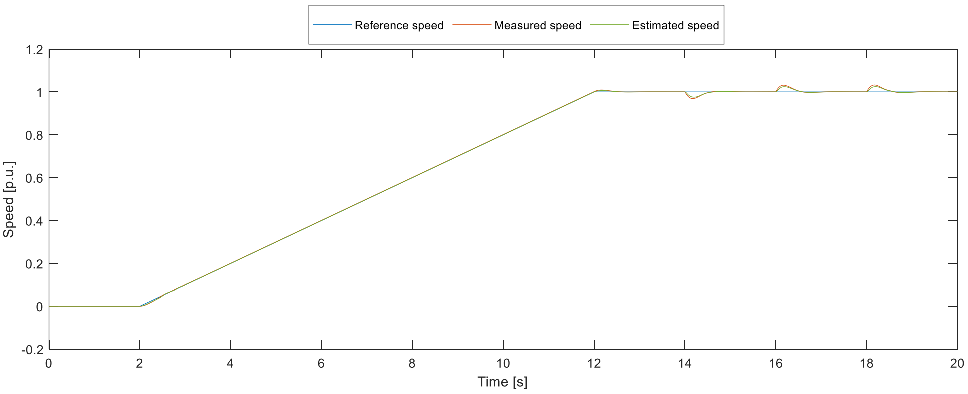

Fig. 53 Reference speed, measured speed and estimated speed. Sensorless FOC for EESM, test 2.

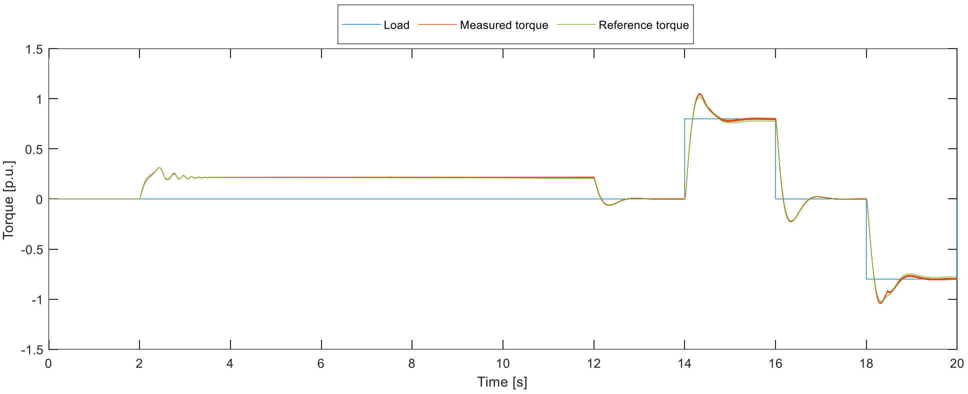

Fig. 54 Load, measured torque and reference torque. Sensorless FOC for EESM, test 2.

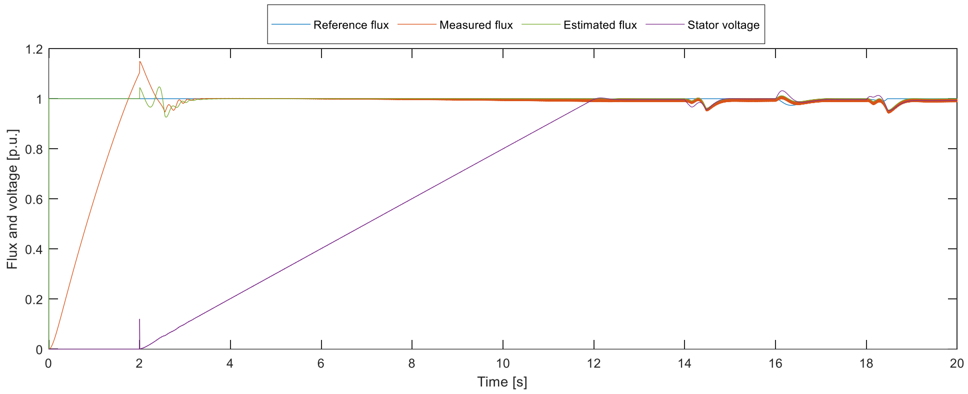

Fig. 55 Reference flux, measured flux, estimated flux and stator voltage. Sensorless FOC for EESM, test 2.

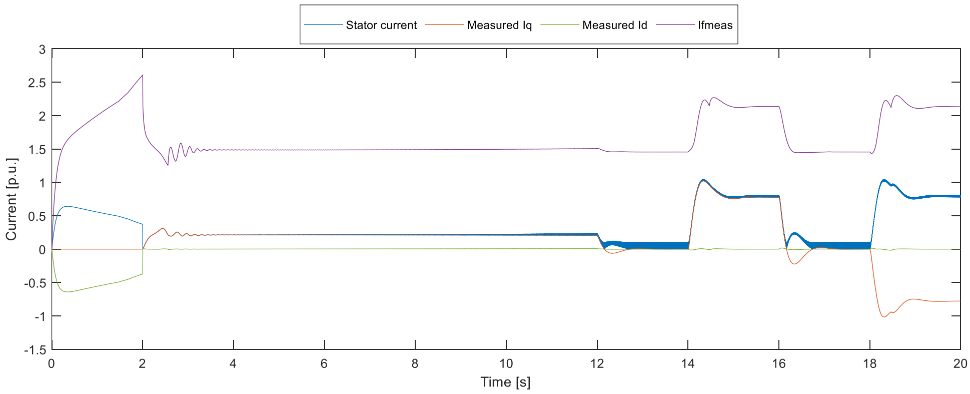

Fig. 56 Stator current, measured Iq, measured Id and measured If. Sensorless FOC for EESM, test 2.

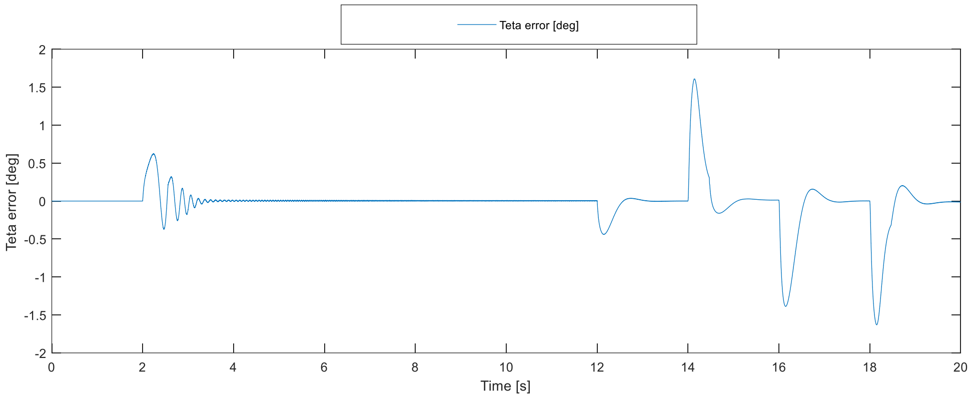

Fig. 57 Stator flux angle error. Sensorless FOC for EESM, test 2.

5.2.3 Test 3

Motor starting with no-load to base speed (1 p.u.) with a 10s ramp, after 2s 0.8 p.u. load step, after 2s back to no-load and then -0.8 p.u. load step. Parameter uncertainty Rs=50%.

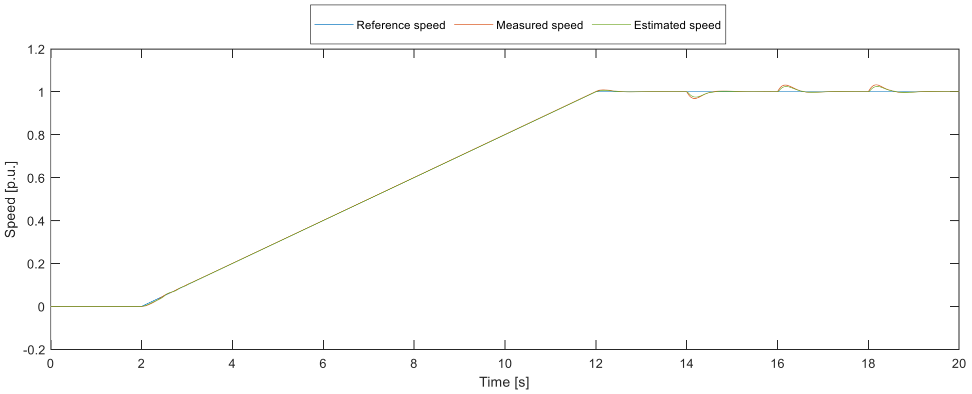

Fig. 58 Reference speed, measured speed and estimated speed. Sensorless FOC for EESM, test 3.

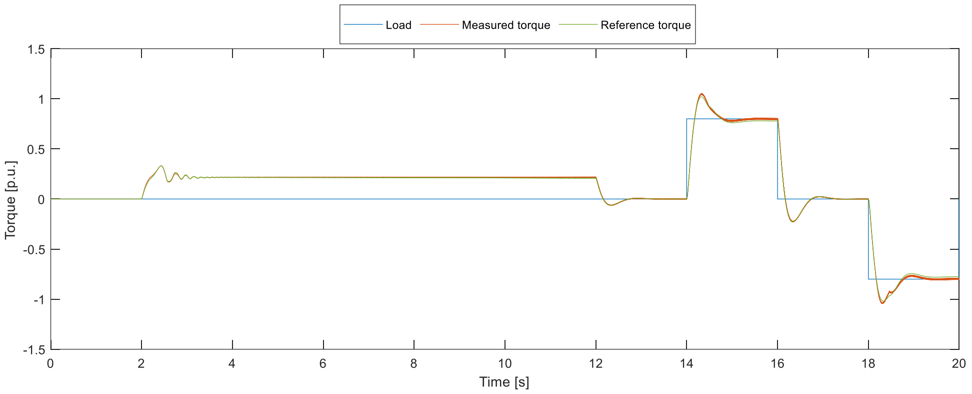

Fig. 59 Load, measured torque and reference torque. Sensorless FOC for EESM, test 3.

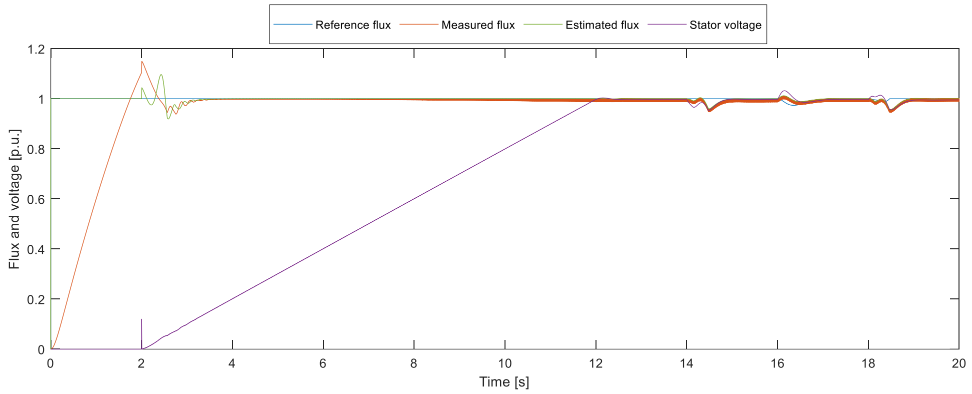

Fig. 60 Reference flux, measured flux, estimated flux and stator voltage. Sensorless FOC for EESM, test 3.

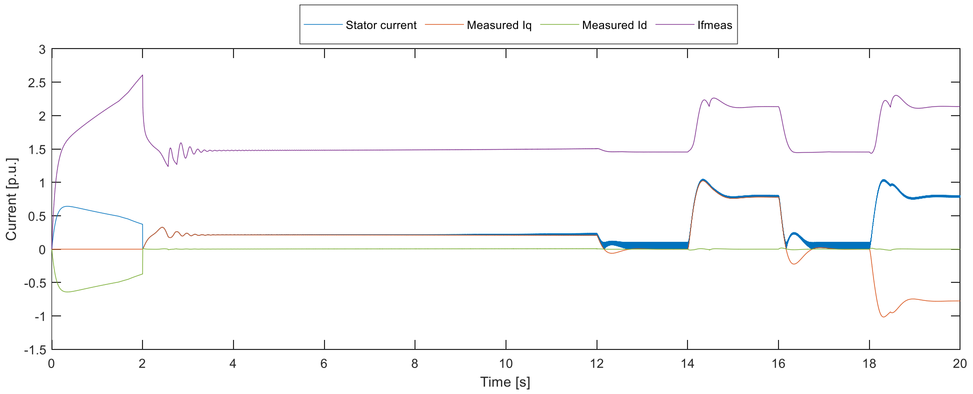

Fig. 61 Stator current, measured Iq, measured Id and measured If. Sensorless FOC for EESM, test 3.

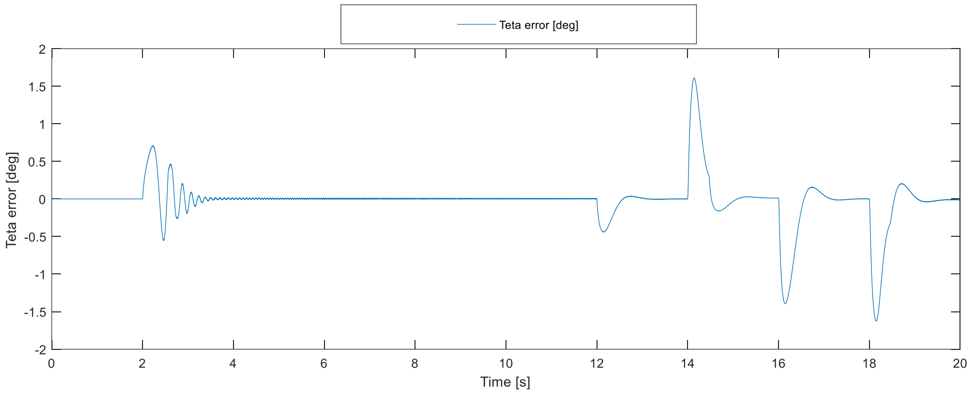

Fig. 62 Stator flux angle error. Sensorless FOC for EESM, test 3.

5.2.4 Test 4

Motor starting with no-load to base speed (1 p.u.) with a 10s ramp, after 2s 0.8 p.u. load step, after 2s back to no-load and then -0.8 p.u. load step. Parameter uncertainty initial stator flux=50%.

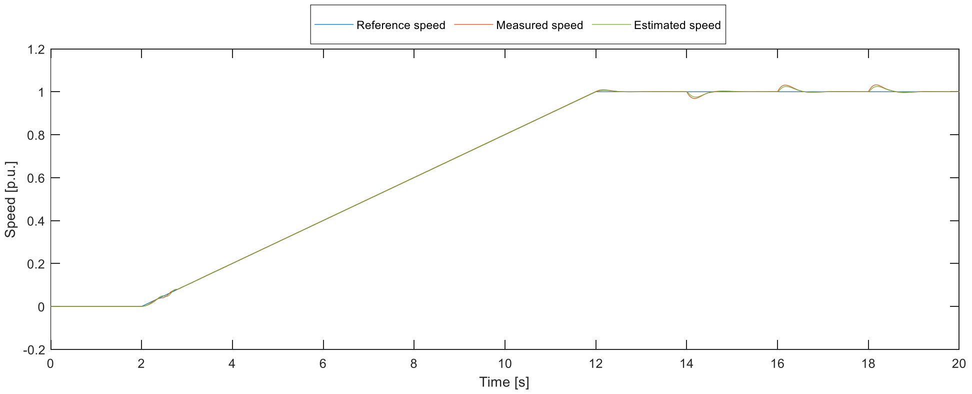

Fig. 63 Reference speed, measured speed and estimated speed. Sensorless FOC for EESM, test 4.

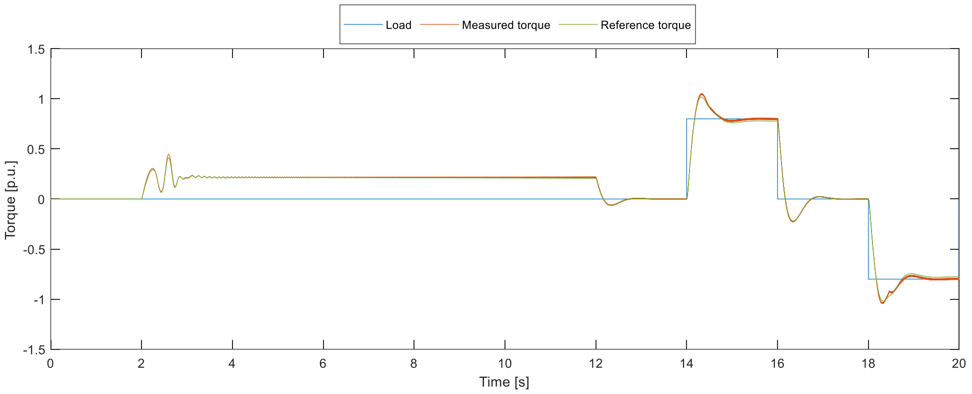

Fig. 64 Load, measured torque and reference torque. Sensorless FOC for EESM, test 4.

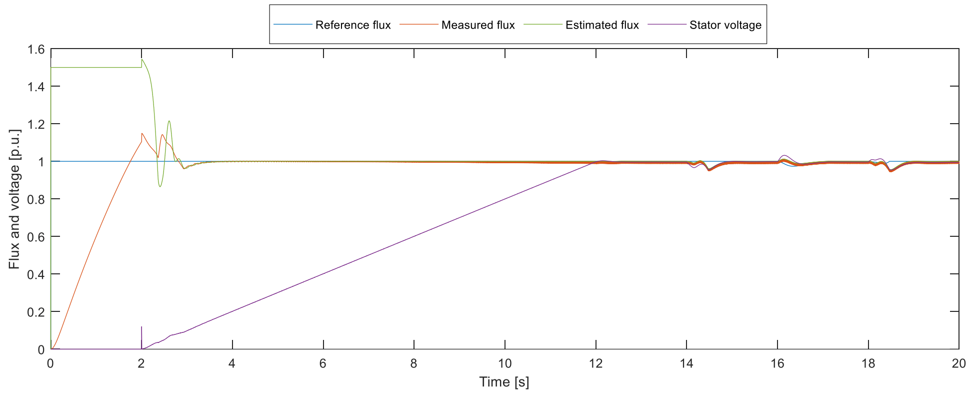

Fig. 65 Reference flux, measured flux, estimated flux and stator voltage. Sensorless FOC for EESM, test 4.

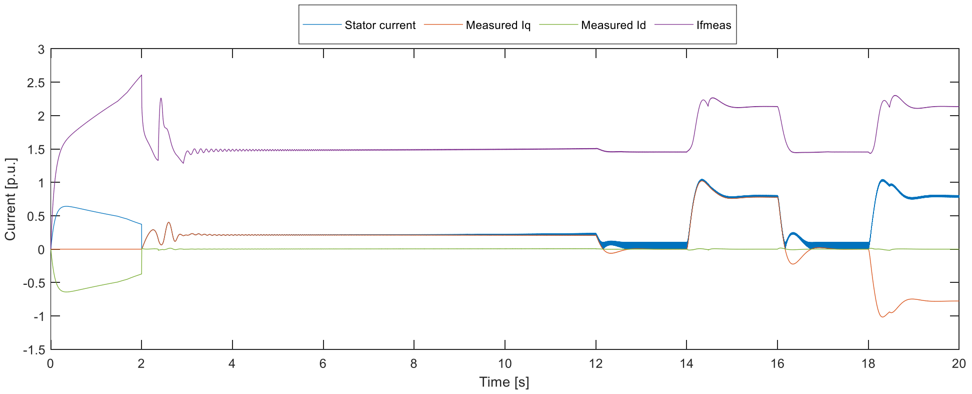

Fig. 66 Stator current, measured Iq, measured Id and measured If. Sensorless FOC for EESM, test 4.

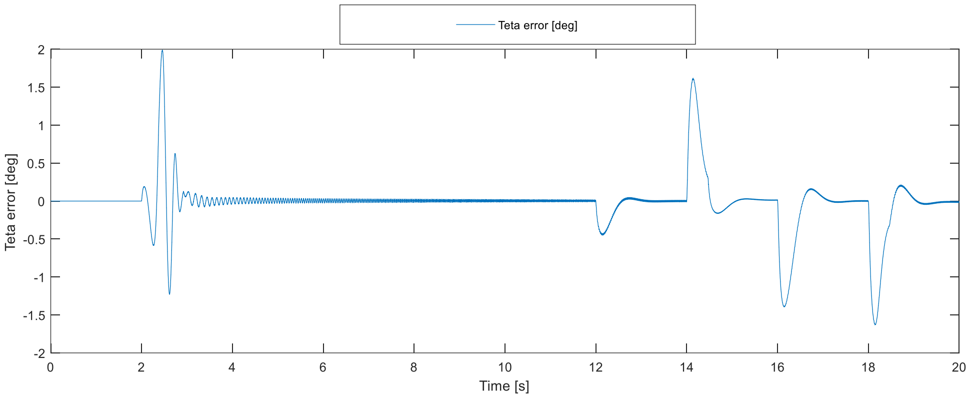

Fig. 67 Stator flux angle error. Sensorless FOC for EESM, test 4.

5.2.5 Test 5

Motor starting with no-load to 0.1 p.u. in 1s ramp, after 2s 0.8 p.u. load step, after 2s acceleration until maximum speed (1.33 p.u.) with a 12.33s ramp, after 2s load step to 0 p.u. No parameter uncertainties.

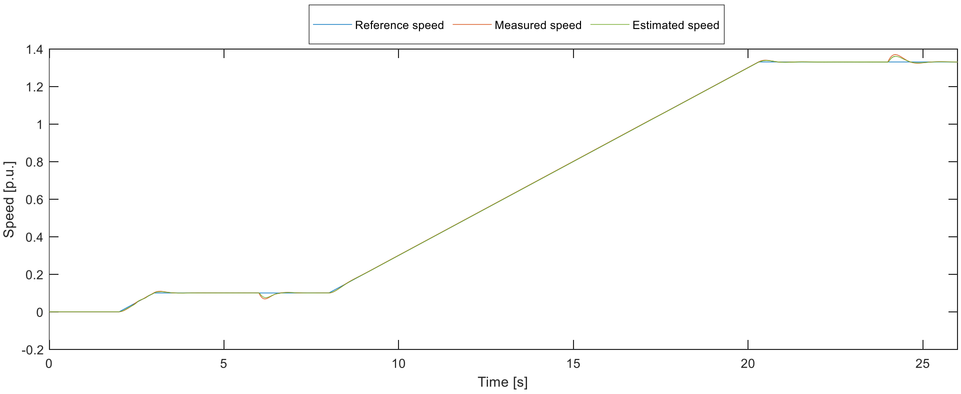

Fig. 68 Reference speed, measured speed and estimated speed. Sensorless FOC for EESM, test 5.

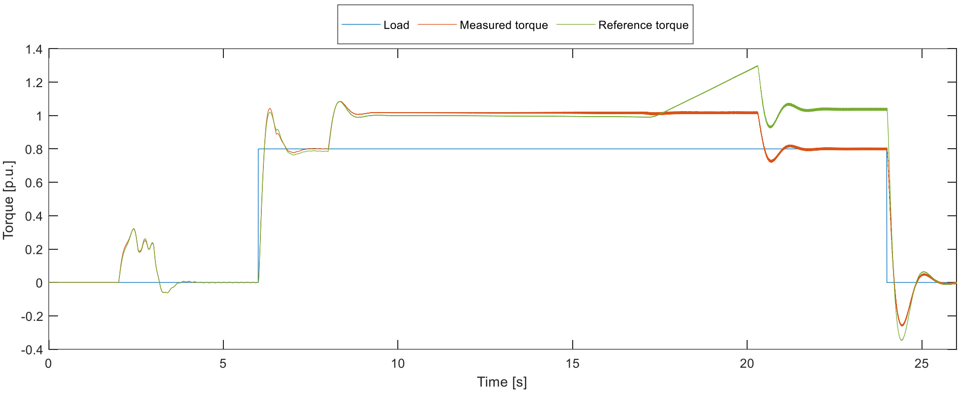

Fig. 69 Load, measured torque and reference torque. Sensorless FOC for EESM, test 5.

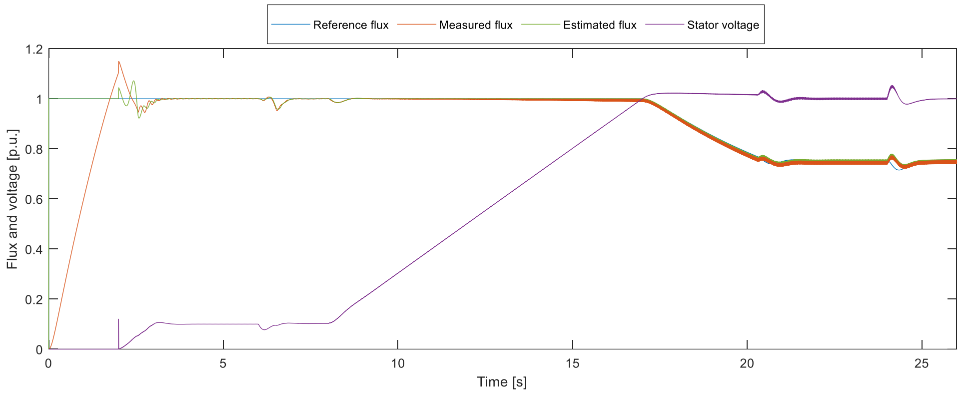

Fig. 70 Reference flux, measured flux, estimated flux and stator voltage. Sensorless FOC for EESM, test 5.

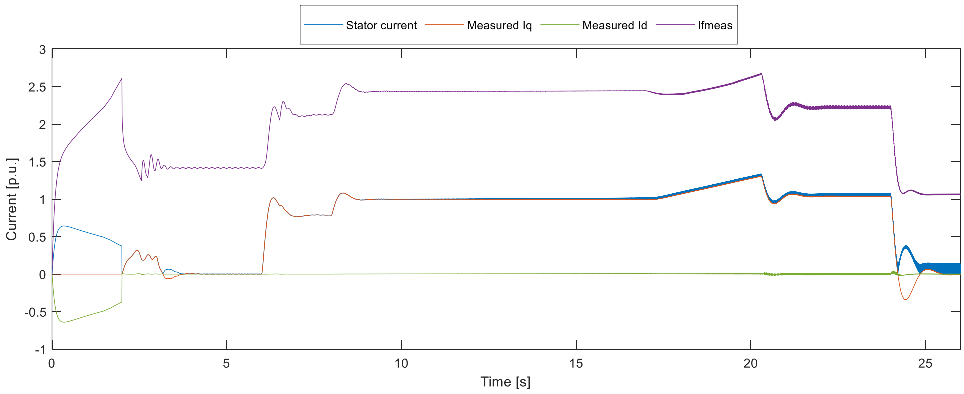

Fig. 71 Stator current, measured Iq, measured Id and measured If. Sensorless FOC for EESM, test 5.

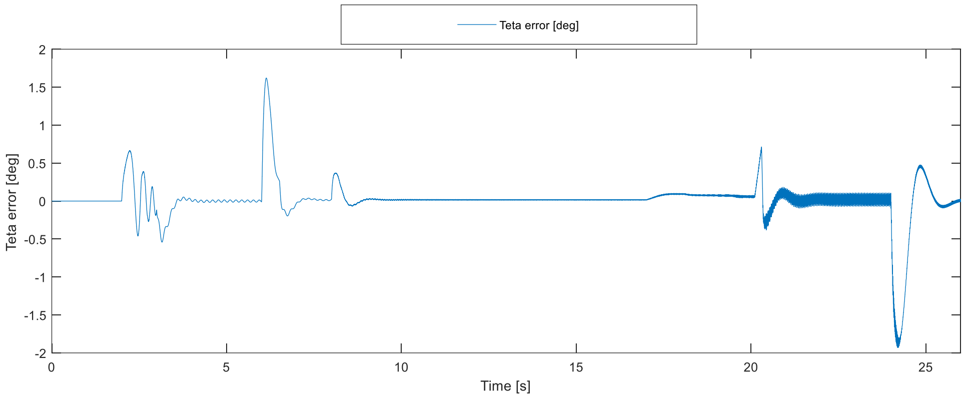

Fig. 72 Stator flux angle error. Sensorless FOC for EESM, test 5.

5.2.6 Test 6

Motor starting with no-load to 0.1 p.u. in 1s ramp, after 2s 0.8 p.u. load step, after 2s acceleration until maximum speed (1.33 p.u.) with a 12.33s ramp, after 2s load step to 0 p.u. Parameter uncertainty Rs=50%.

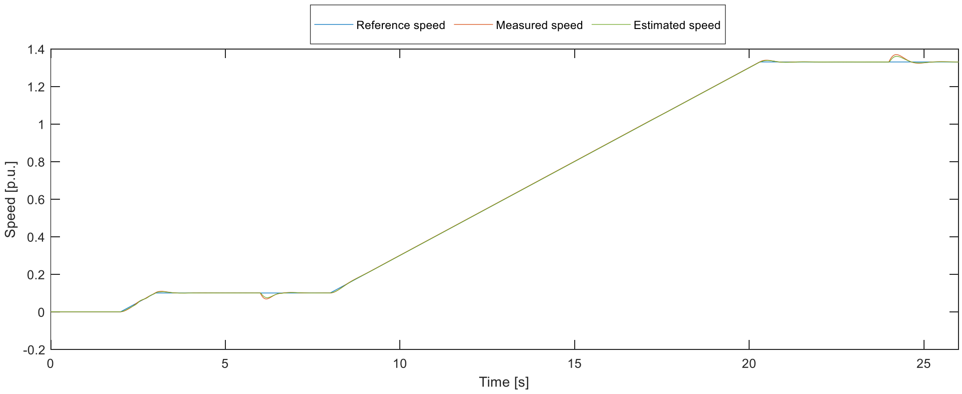

Fig. 73 Reference speed, measured speed and estimated speed. Sensorless FOC for EESM, test 6.

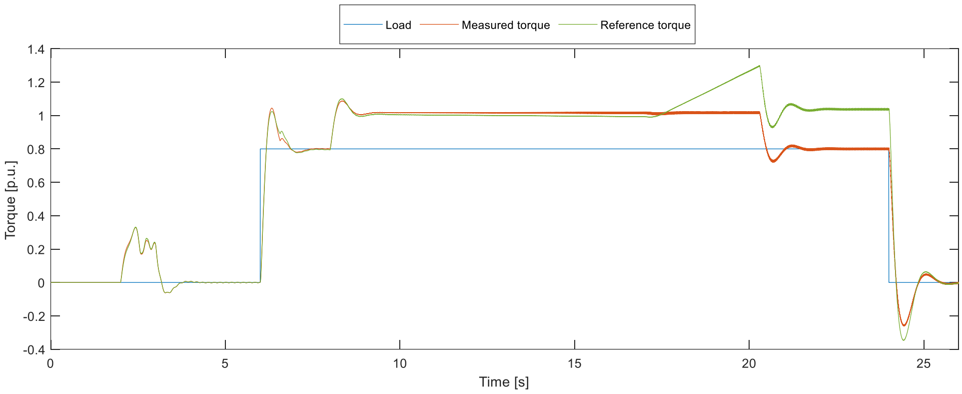

Fig. 74 Load, measured torque and reference torque. Sensorless FOC for EESM, test 6.

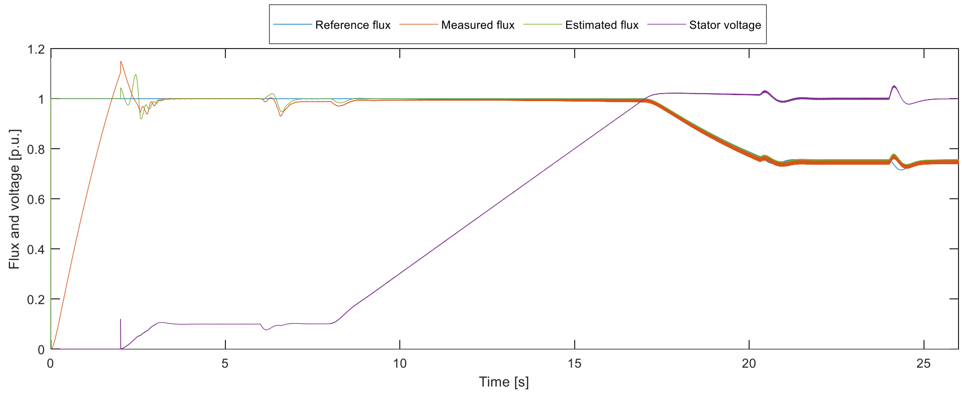

Fig. 75 Reference flux, measured flux, estimated flux and stator voltage. Sensorless FOC for EESM, test 6.

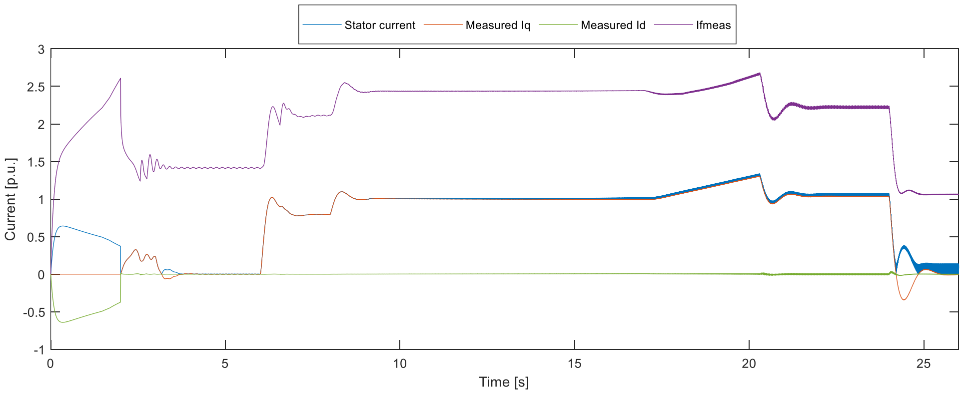

Fig. 76 Stator current, measured Iq, measured Id and measured If. Sensorless FOC for EESM, test 6.

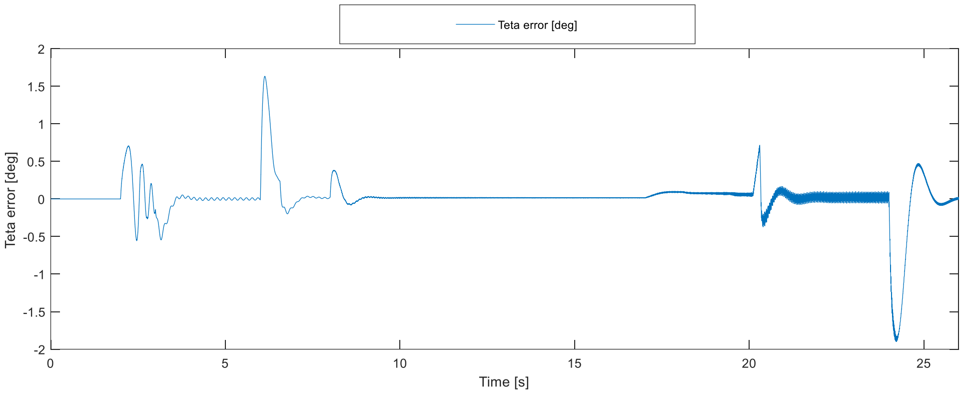

Fig. 77 Stator flux angle error. Sensorless FOC for EESM, test 6.

5.2.7 Test 7

Motor starting with no-load to 0.1 p.u. in 1s ramp, after 2s 0.8 p.u. load step, after 2s acceleration until maximum speed (1.33 p.u.) with a 12.33s ramp, after 2s load step to 0 p.u. Parameter uncertainty Rs=50% and initial rotor angle with 90° electrical angle.

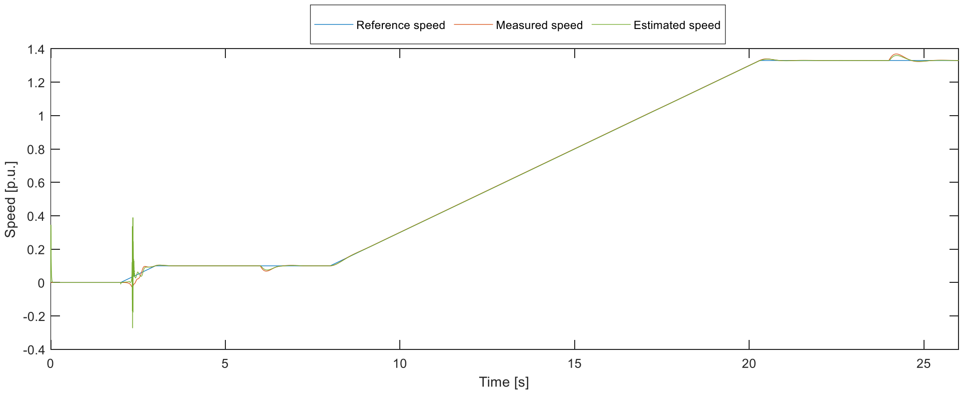

Fig. 78 Reference speed, measured speed and estimated speed. Sensorless FOC for EESM, test 7.

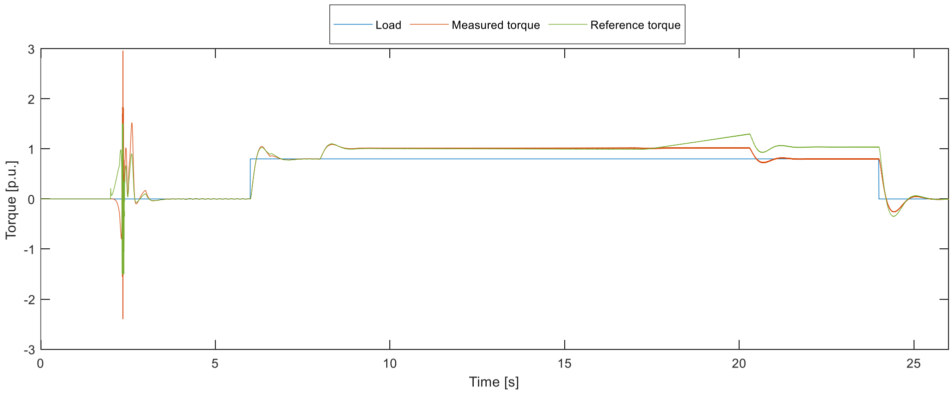

Fig. 79 Load, measured torque and reference torque. Sensorless FOC for EESM, test 7.

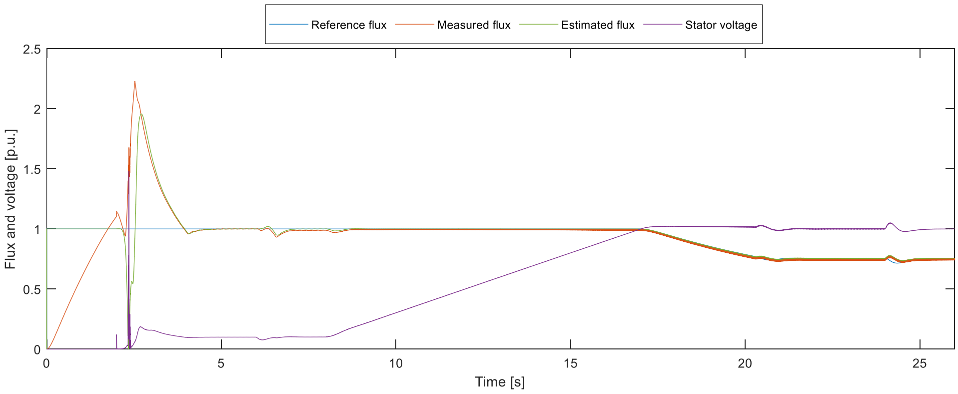

Fig. 80 Reference flux, measured flux, estimated flux and stator voltage. Sensorless FOC for EESM, test 7.

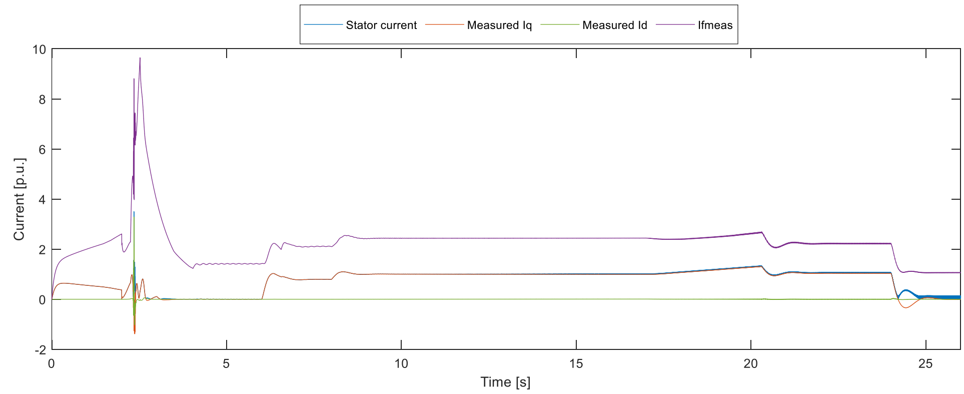

Fig. 81 Stator current, measured Iq, measured Id and measured If. Sensorless FOC for EESM, test 7.

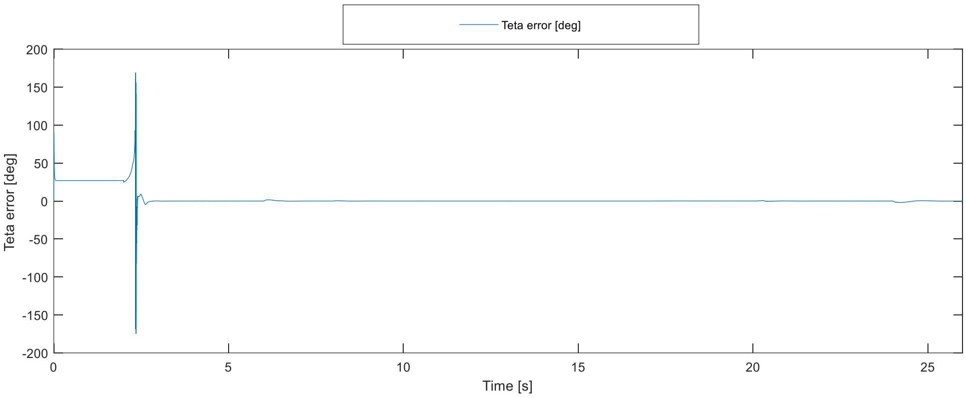

Fig. 82 Stator flux angle error. Sensorless FOC for EESM, test 7.

5.2.8 Test 8

Motor starting with 0.8 p.u. load to 0.1 p.u. speed with 1s ramp, after 4s deceleration to minus 0.1 p.u. with a 2s ramp, after 4s back to standstill. No parameter uncertainties.

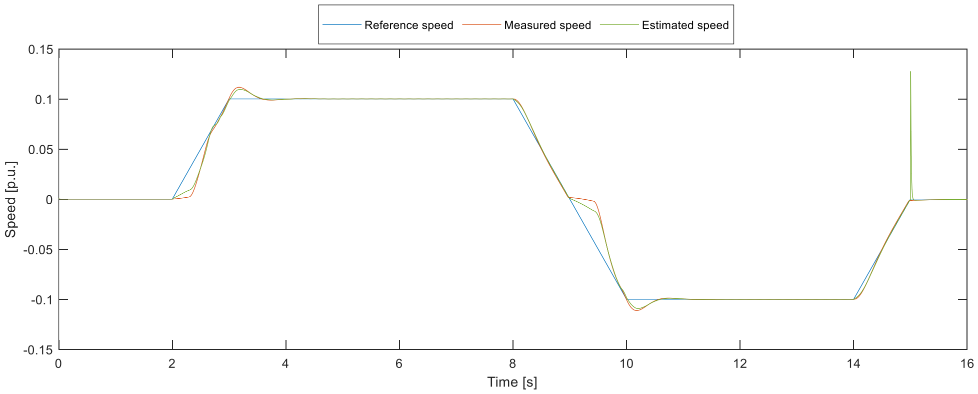

Fig. 83 Reference speed, measured speed and estimated speed. Sensorless FOC for EESM, test 8.

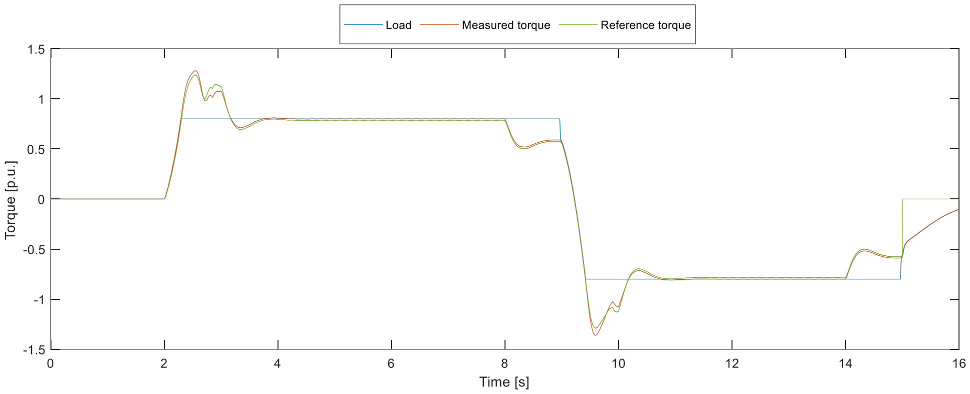

Fig. 84 Load, measured torque and reference torque. Sensorless FOC for EESM, test 8.

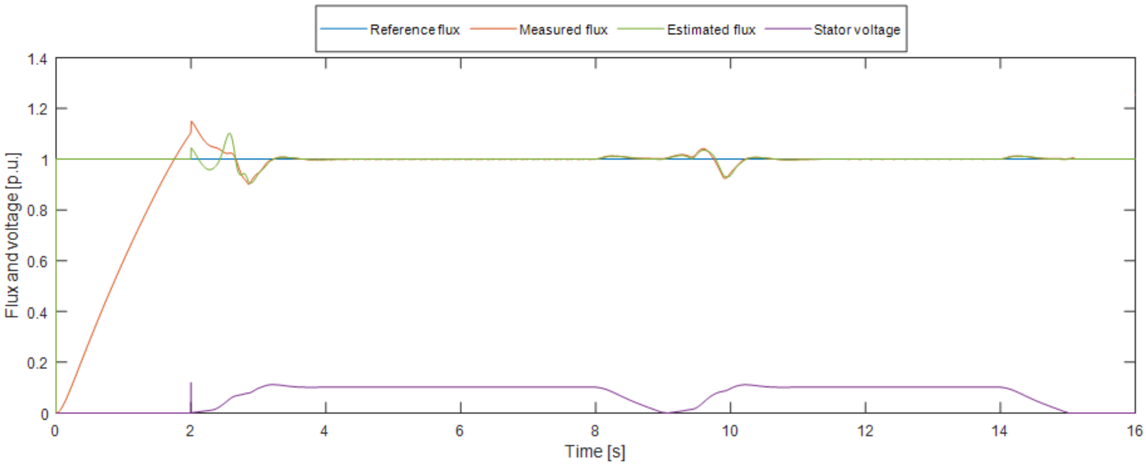

Fig. 85 Reference flux, measured flux, estimated flux and stator voltage. Sensorless FOC for EESM, test 8.

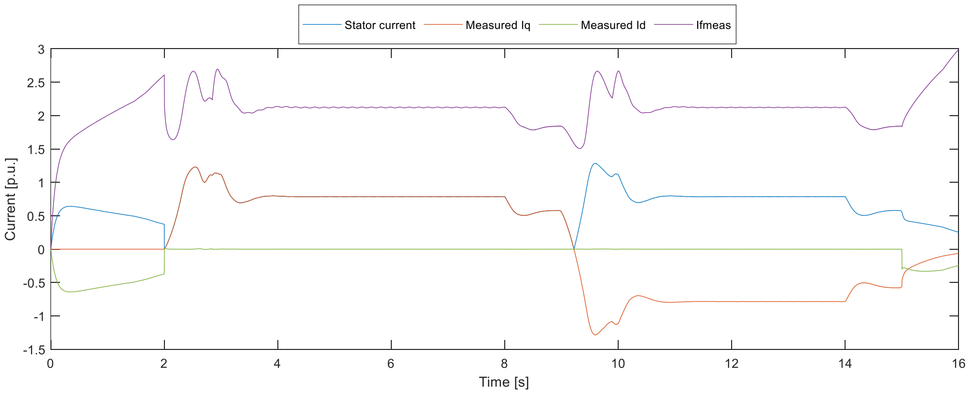

Fig. 86 Stator current, measured Iq, measured Id and measured If. Sensorless FOC for EESM, test 8.

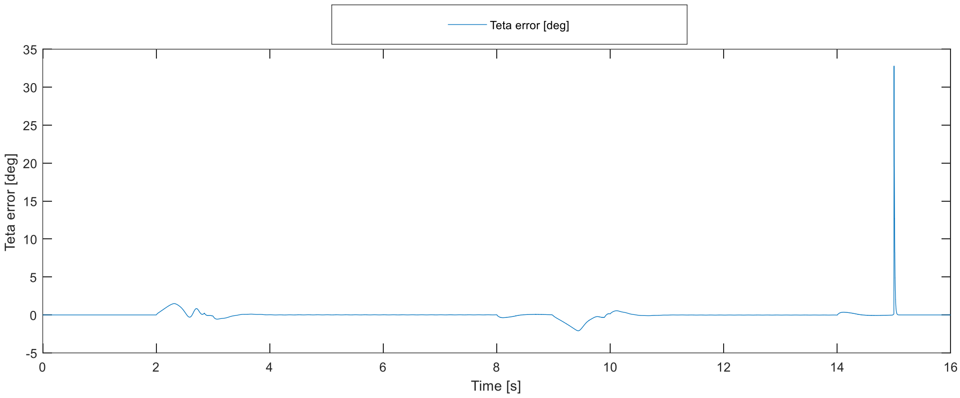

Fig. 87 Stator flux angle error. Sensorless FOC for EESM, test 8.

5.2.9 Test 9

Motor starting with 0.8 p.u. load to 0.1 p.u. speed with 1s ramp, after 4s deceleration to minus 0.1 p.u. with a 2s ramp, after 4s back to standstill. Parameter uncertainty Rs=50%.

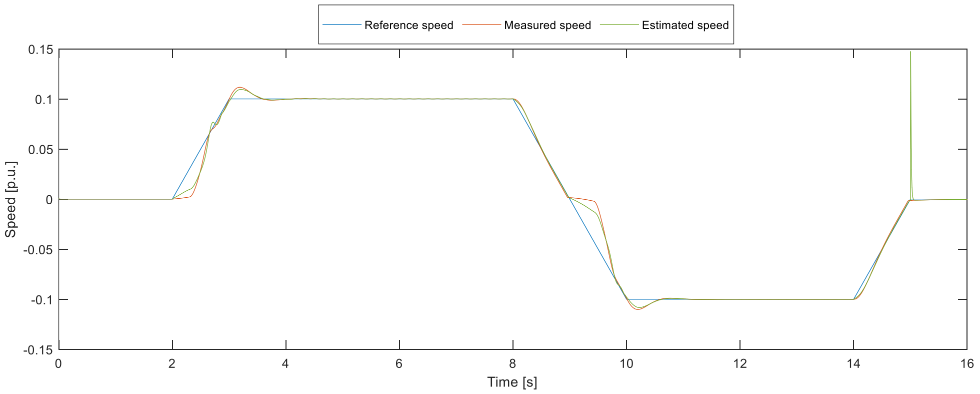

Fig. 88 Reference speed, measured speed and estimated speed. Sensorless FOC for EESM, test 9.

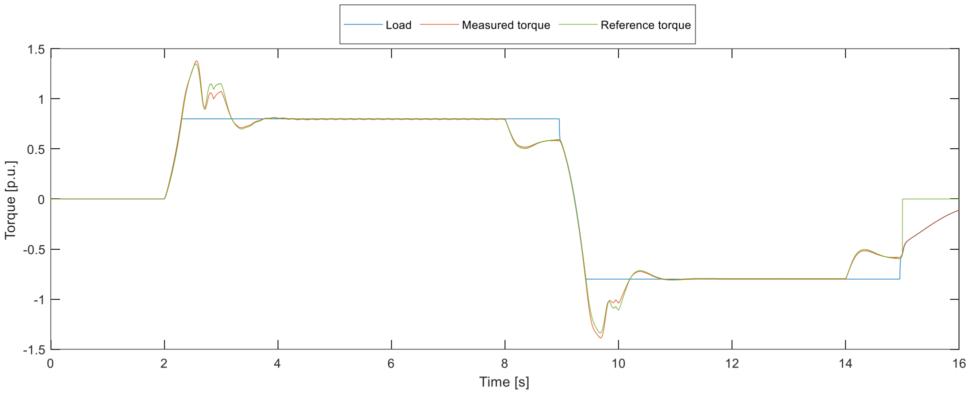

Fig. 89 Load, measured torque and reference torque. Sensorless FOC for EESM, test 9.

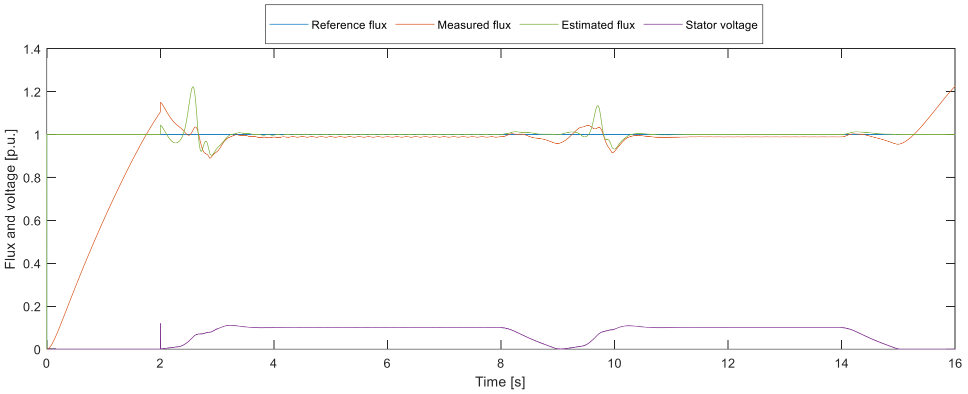

Fig. 90 Reference flux, measured flux, estimated flux and stator voltage. Sensorless FOC for EESM, test 9.

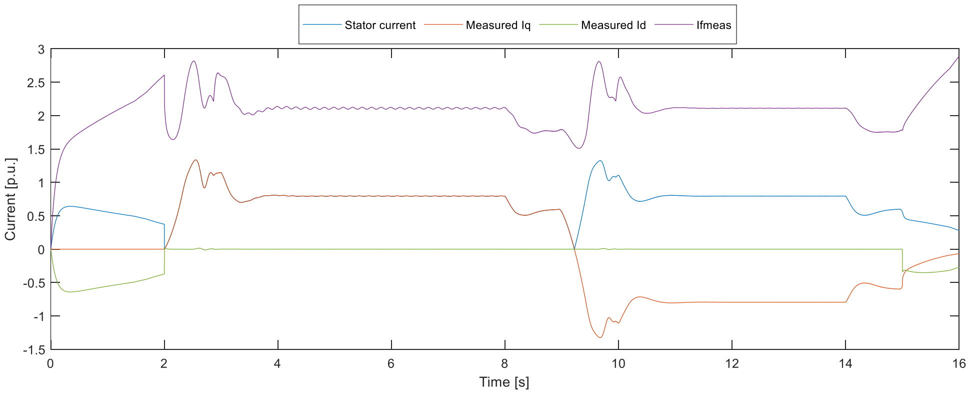

Fig. 91 Stator current, measured Iq, measured Id and measured If. Sensorless FOC for EESM, test 9.

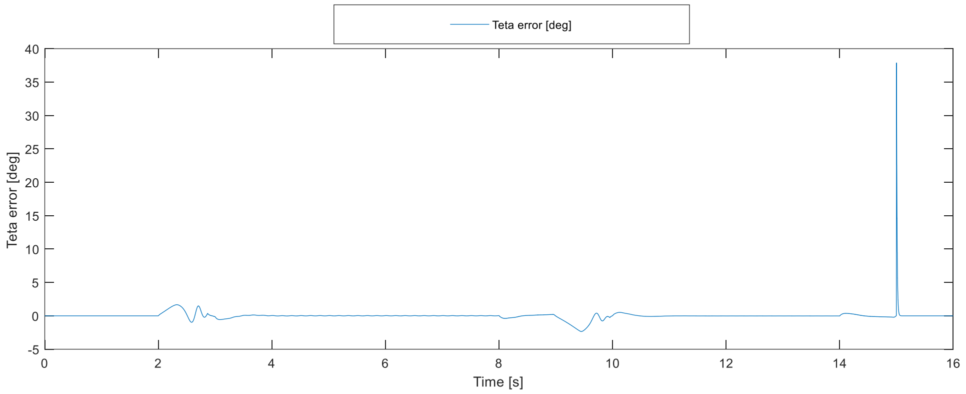

Fig. 92 Stator flux angle error. Sensorless FOC for EESM, test 9.

5.2.10 Test 10

Motor starting with 0.8 p.u. load to 0.1 p.u. speed with 1s ramp, after 4s deceleration to minus 0.1 p.u. with a 2s ramp, after 4s back to standstill. Parameter uncertainty Rs=50% and initial rotor angle with 90° electrical angle.

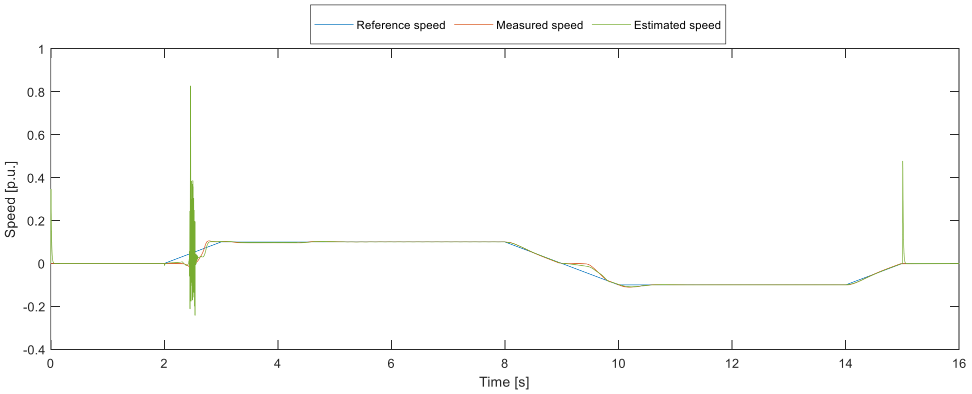

Fig. 93 Reference speed, measured speed and estimated speed. Sensorless FOC for EESM, test 10.

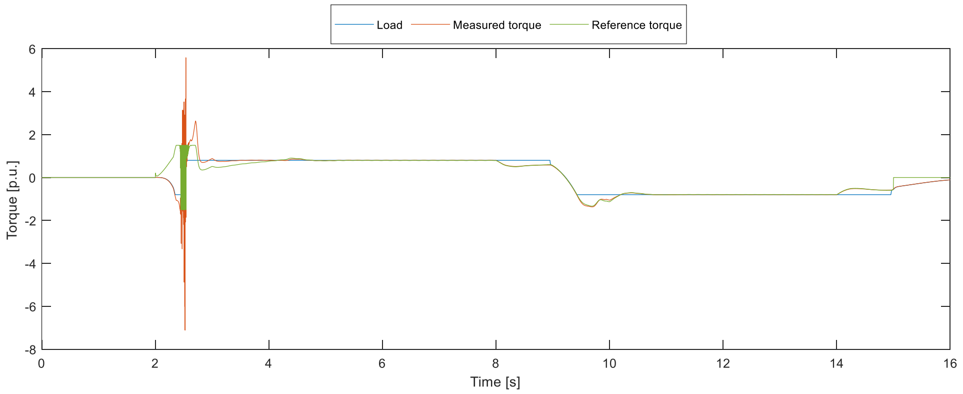

Fig. 94 Load, measured torque and reference torque. Sensorless FOC for EESM, test 10.

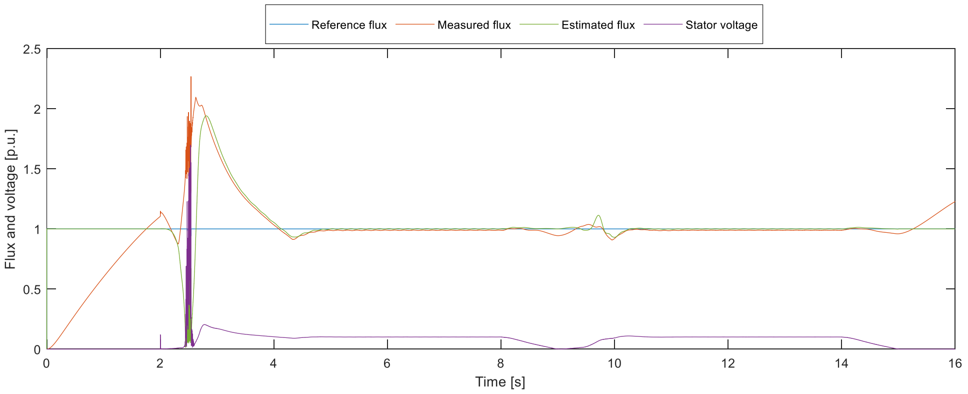

Fig. 95 Reference flux, measured flux, estimated flux and stator voltage. Sensorless FOC for EESM, test 10.

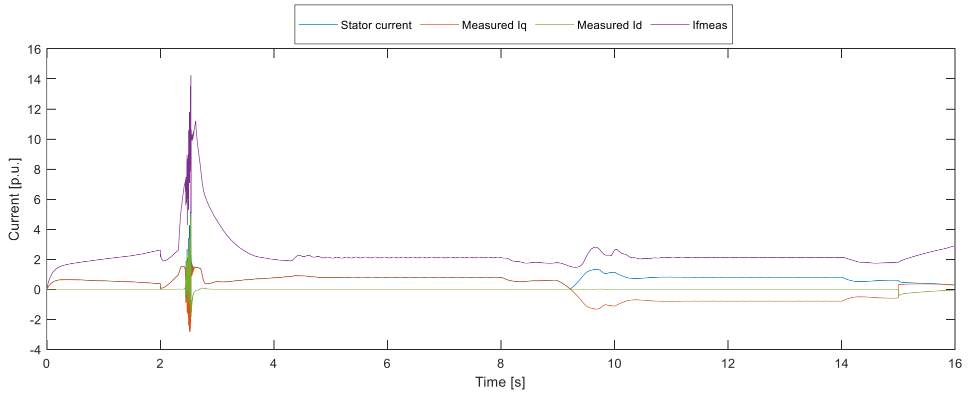

Fig. 96 Stator current, measured Iq, measured Id and measured If. Sensorless FOC for EESM, test 10.

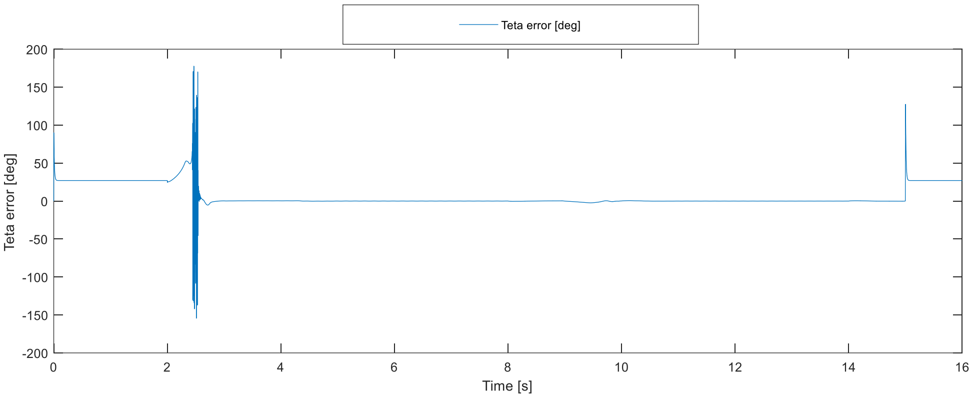

Fig. 97 Stator flux angle error. Sensorless FOC for EESM, test 10.

5.2.11 Test 11

Motor starting with 0.8 p.u. load to 0.1 p.u. speed with 1s ramp, after 4s deceleration to minus 0.1 p.u. with a 2s ramp, after 4s back to standstill. Parameter uncertainty Rs=50% and initial rotor angle with 30° electrical angle.

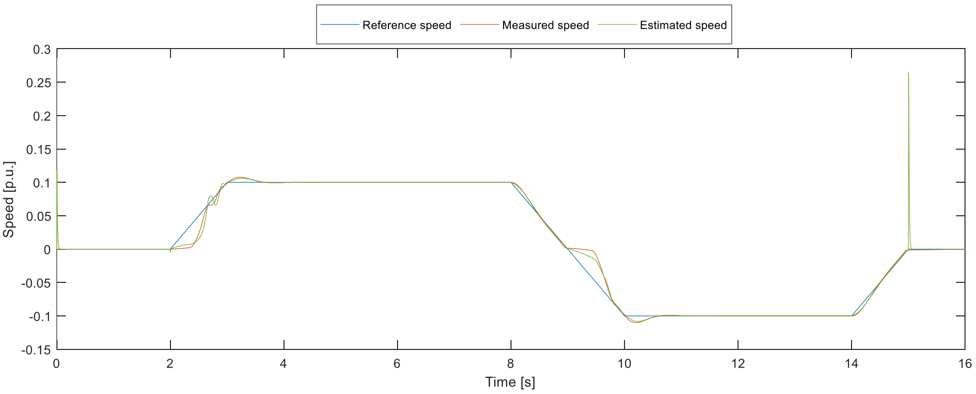

Fig. 98 Reference speed, measured speed and estimated speed. Sensorless FOC for EESM, test 11.

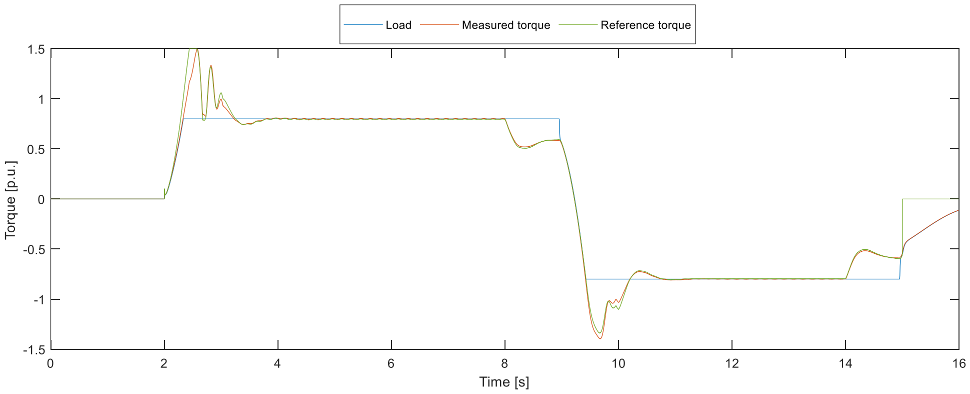

Fig. 99 Load, measured torque and reference torque. Sensorless FOC for EESM, test 11.

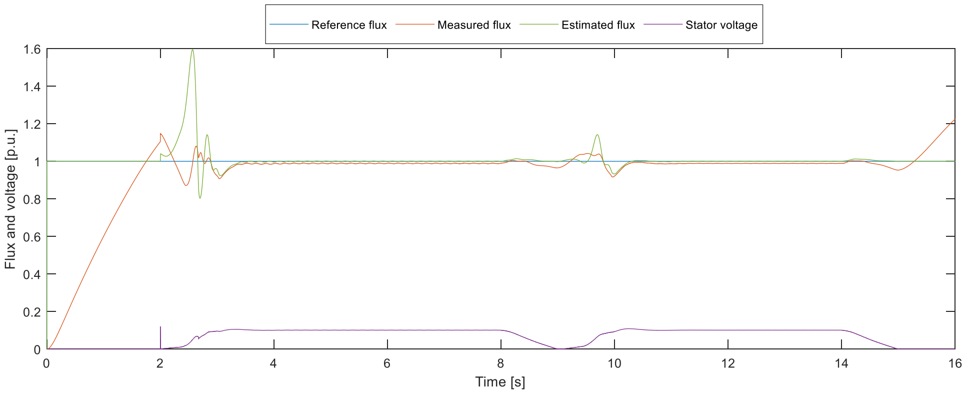

Fig. 100 Reference flux, measured flux, estimated flux and stator voltage. Sensorless FOC for EESM, test 11.

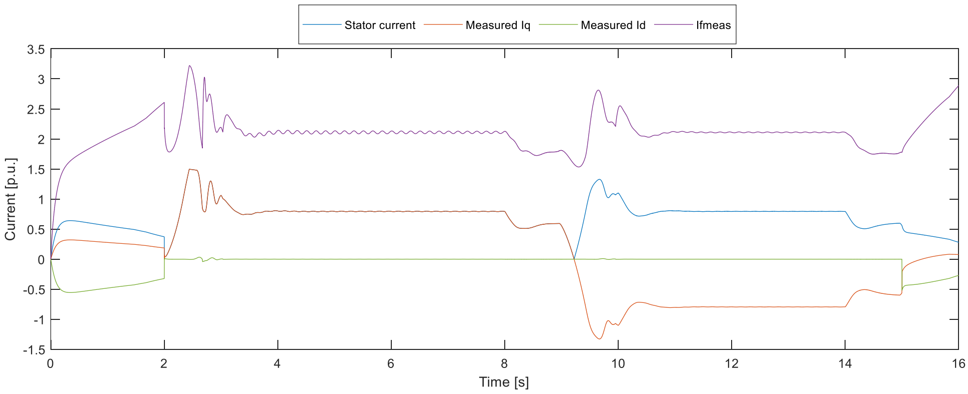

Fig. 101 Stator current, measured Iq, measured Id and measured If. Sensorless FOC for EESM, test 11.

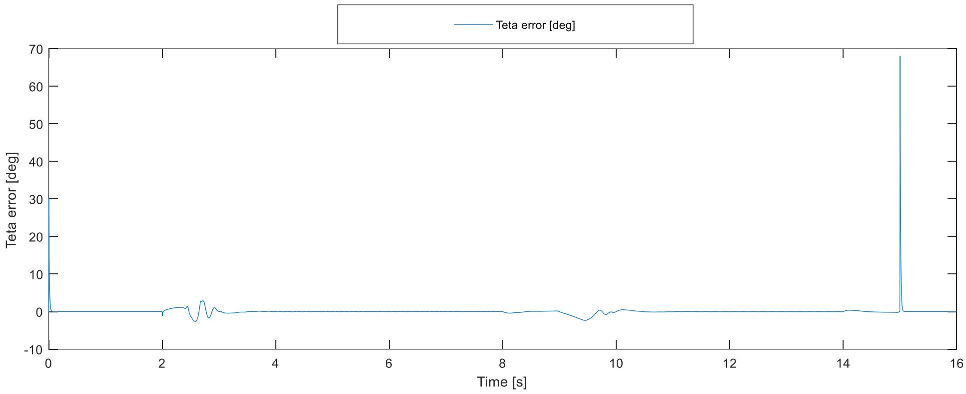

Fig. 102 Stator flux angle error. Sensorless FOC for EESM, test 11.

5.2.12 Test 12

Motor starting with 0.8 p.u. load to 0.1 p.u. speed with 1s ramp, after 4s deceleration to minus 0.1 p.u. with a 2s ramp, after 4s back to standstill. Parameter uncertainty Rs=50% and initial rotor angle with -90° electrical angle.

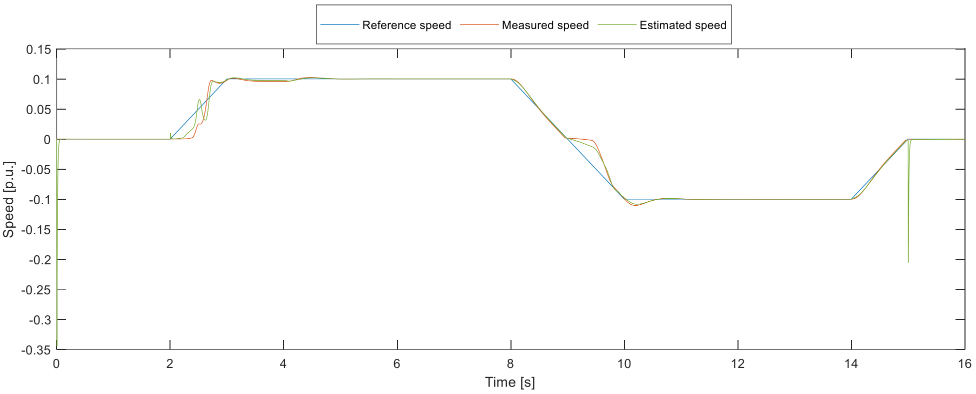

Fig. 103 Reference speed, measured speed and estimated speed. Sensorless FOC for EESM, test 12.

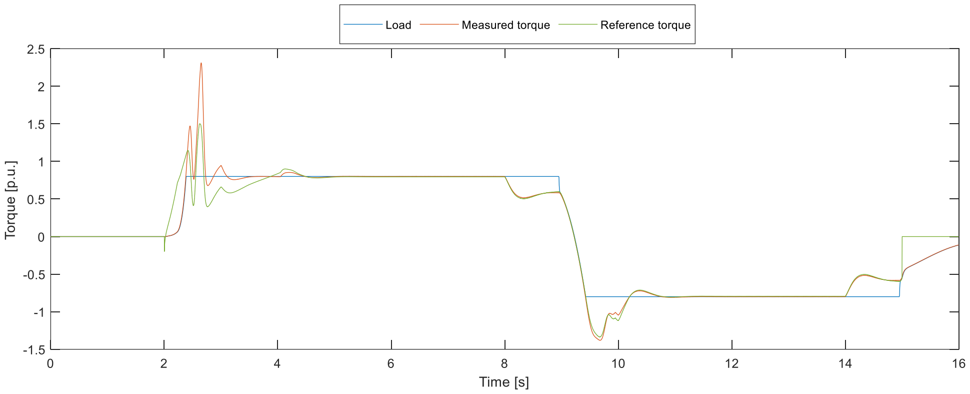

Fig. 104 Load, measured torque and reference torque. Sensorless FOC for EESM, test 12.

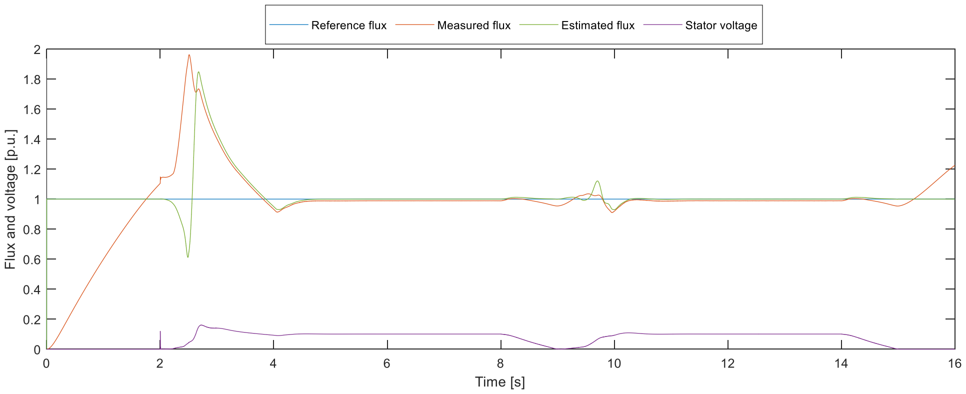

Fig. 105 Reference flux, measured flux, estimated flux and stator voltage. Sensorless FOC for EESM, test 12.

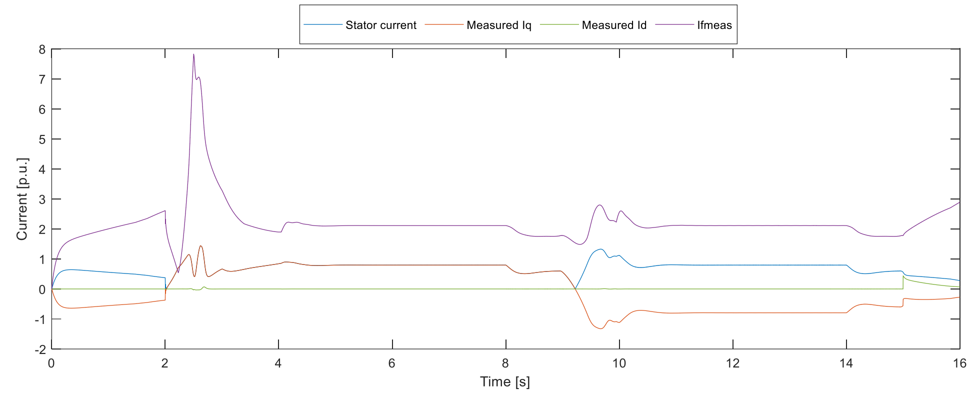

Fig. 106 Stator current, measured Iq, measured Id and measured If. Sensorless FOC for EESM, test 12.

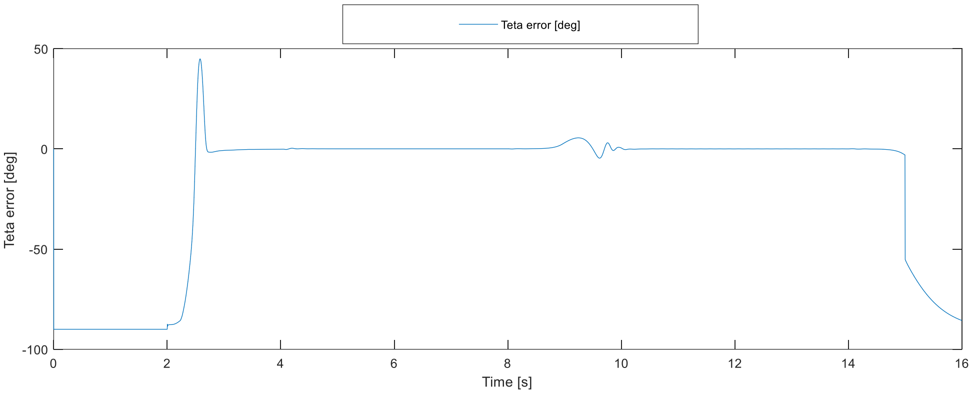

Fig. 107 Stator flux angle error. Sensorless FOC for EESM, test 12.

5.2.13 Test 13

Motor starting with 0.8 p.u. load to 0.03 p.u. speed with a 0.3s ramp, after 4s deceleration to minus 0.03 p.u. with a 0.6s ramp, after 4s back to standstill. Parameter uncertainty Rs=50%.

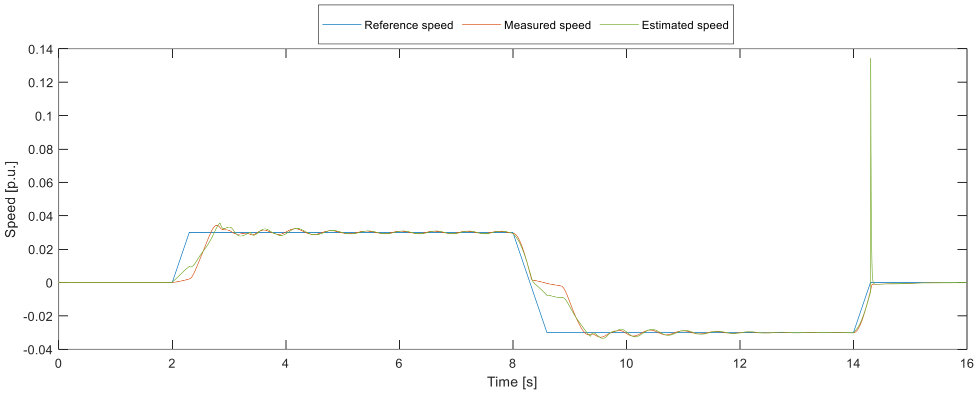

Fig. 108 Reference speed, measured speed and estimated speed. Sensorless FOC for EESM, test 13.

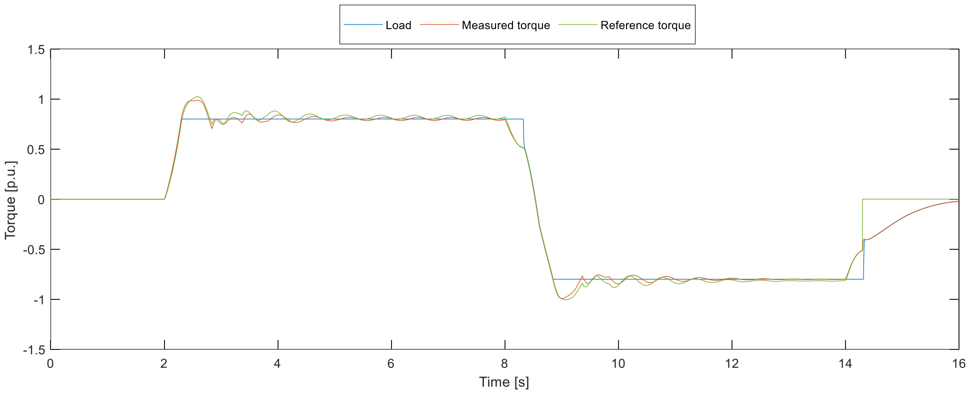

Fig. 109 Load, measured torque and reference torque. Sensorless FOC for EESM, test 13.

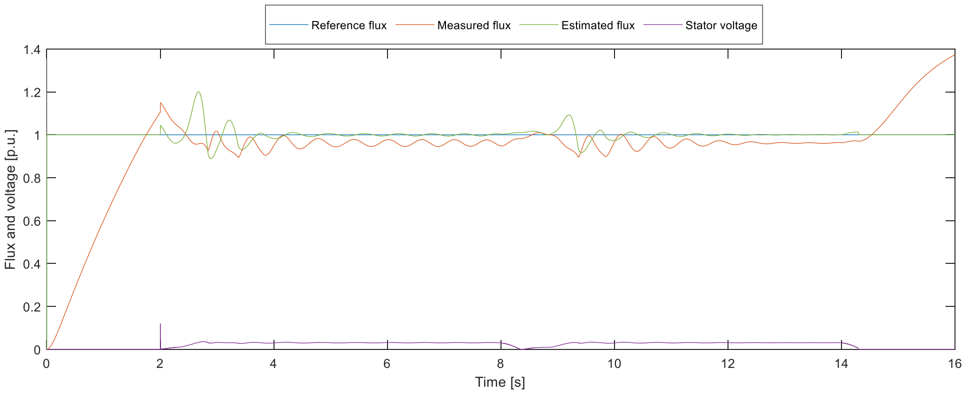

Fig. 110 Reference flux, measured flux, estimated flux and stator voltage. Sensorless FOC for EESM, test 13.

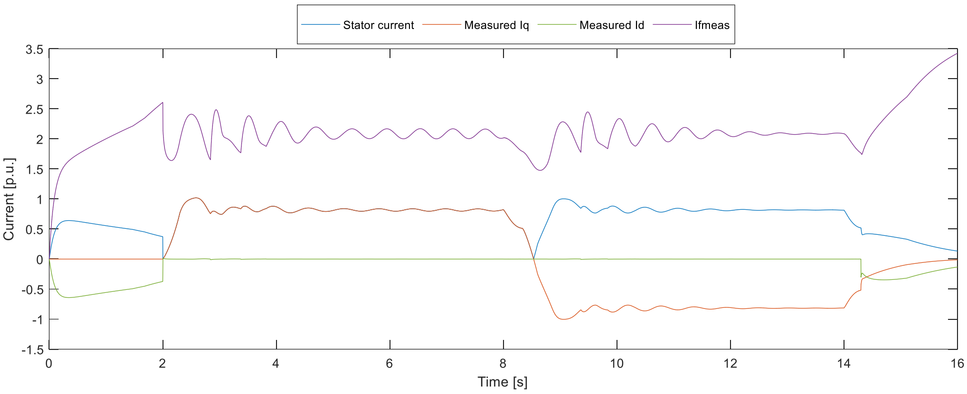

Fig. 111 Stator current, measured Iq, measured Id and measured If. Sensorless FOC for EESM, test 13.

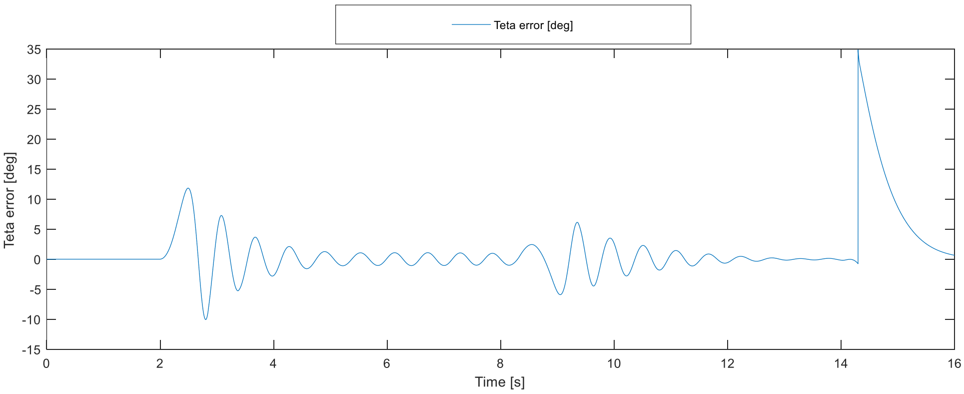

Fig. 112 Stator flux angle error. Sensorless FOC for EESM, test 13.

5.2.14 Comments on EESM simulation results

The tests shown a good algorithm behaviour in the different operating conditions. The most critical aspect concerns the knowledge of the initial rotor angle. In the test 7, with a no-load starting with an rotor angle electrical error of 90°, one can note considerable torque oscillations and, therefore, speed oscillations. These oscillations are even higher in the motor starting with 0.8 p.u. load in test 10, where the measured torque reaches the unsustainable value of 7 p.u.

In test 11, with a rotor angle electrical error of 30°, the torque oscillations are significantly lower and the measured torque reaches the maximum value of 1.5 p.u.

In test 12, one can note that with a rotor angle electrical error of -90° the motor starts with significantly lower oscillations in comparison to the positive angle.

The oscillations are negligible with a precise measure of initial rotor angle.

In test 13 one can note significantly oscillations, since the reference speed is very low (3% of the rated value).

6 Test bench and experimental results on EESM

6.1 Test bench

An experimental test bench was developed in the Petra Lab of the University of Genoa, in order to carry out some preliminary tests on EESMs. The complete test bench is shown in Fig. 113, whereas a zoom on the motor is reported in Fig. 114.

A wound rotor induction motor (which parameters are reported in Table 13) was modified in order to be used with the same behaviour of an EESM (from this point the induction motor will be referred as EESM). For the purpose, two rotor winding (phase b and phase c) were short-circuited. The rotor was supplied with a DC voltage, with the positive pole connected to phase a and the negative pole connected to phase b and c.

An optical incremental encoder with zero pulse is used to measure the real rotor position angle.

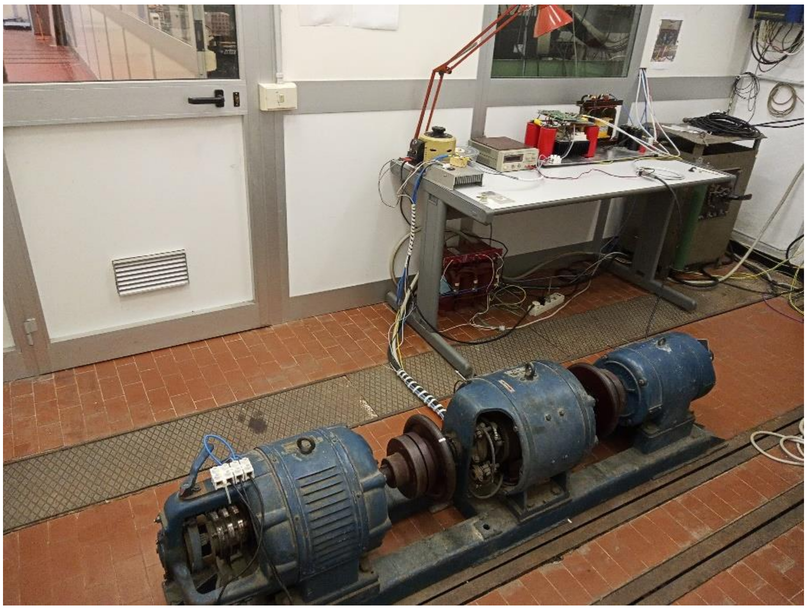

Fig. 113 EESM complete test bench

Fig. 114 Induction motor used as EESM

Table 13 Induction motor (used as EESM) parameters

Parameter	Value	Parameter	Value
Voltage	380 V / 50 Hz	Rated speed	1450 rpm
Current	15.7 A	Pole pairs	2

The motor is controlled with the same inverter shown in section 3.1 for the PMSM and using the same control platform. A DC-DC converter is used to supply the rotor winding. Also the DC-DC converter is controlled by Dspace. Other two motors are coupled to the EESM in order to simulate an inertial load.

With this configuration, the induction motor behaviour is analogous to the behaviour of an EESM. However, the rotor windings are developed with different criteria, since the motor is designed for operating in different conditions. Indeed, EESM rotors are usually supplied with relatively high voltage and low current; for this size of motor, about 1-3 A and 100-200 V. The rotor of the machine used in the proposed test bench, on the contrary, was supplied by a voltage of about 5 V and a current of about 30 A. Of course, this is because the rotor windings are not optimized for the proposed application.

The flux obtained with 30 A (which is about the rotor rated current) leads to a rated stator current of about 4 A. Above this value the load angle approaches significantly 90°, leading to instability.

For this reason, only no-load tests (using just the inertia load) were carried out. The tests have to be considered as a preliminary validation of the proposed algorithm and the development of a more proper test bench will be the topic of future works and for experimental evaluations on a high power test bench (500 kW) in Nidec ASI testing room.

The parameters of the proposed test bench can be therefore summarized as in Table 14.

Table 14 EESM test bench parameters

Parameter	Value
Stator voltage	380 V / 50 Hz
Stator current (Iq PI limit)	6 A (peak value)
Rated speed	150 rad/s
Rotor voltage	5 V
Rotor current	30 A
Inertia constant (motor+load)	5s

6.2 Experimental results for EESM

Since the test bench is characterized by a high inertia and the inverter presented in section 3.1 cannot perform regenerative braking on the grid (indeed, it has a diode rectifier as input stage), the deceleration ramp should be sufficiently smooth. In all the tests the accelerating ramp was limited to 50 rad/s^2, whereas the decelerating ramp was limited to 15 rad/s^2. The following test were performed:

- Test 1 → machine excitation (rotor voltage step variation), machine starting to 10 rad/s (6.7% of the rated speed) and deceleration to standstill.
- Test 2 → machine excitation (rotor voltage step variation), machine starting to 50 rad/s (33% of the rated speed) and deceleration to standstill.
- Test 3 → machine excitation (rotor voltage step variation), machine starting to 150 rad/s (100% of the rated speed) and deceleration to standstill.
- Test 4 → initial rotor angle identification with different rotor angle.

The results of the different tests are reported in the followings.

6.2.1 Test 1

Machine excitation (rotor voltage step variation), machine starting to 10 rad/s (6.7% of the rated speed) and deceleration to standstill.
The motor is fluxed at about 2s and the initial rotor angle estimation algorithm is carried out. For this reason one can note the step variation in the estimated angle (Fig. 117) and in the stator flux (Fig. 118). The motor starts at about 4s.

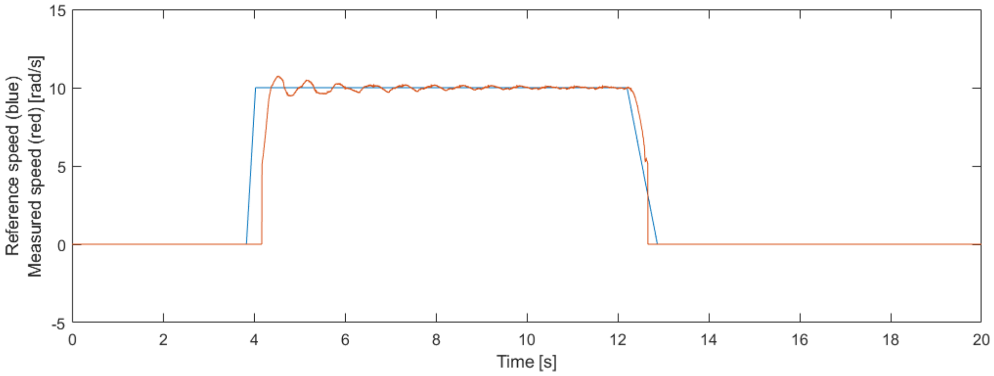

Fig. 115 Reference speed and measured speed, test 1

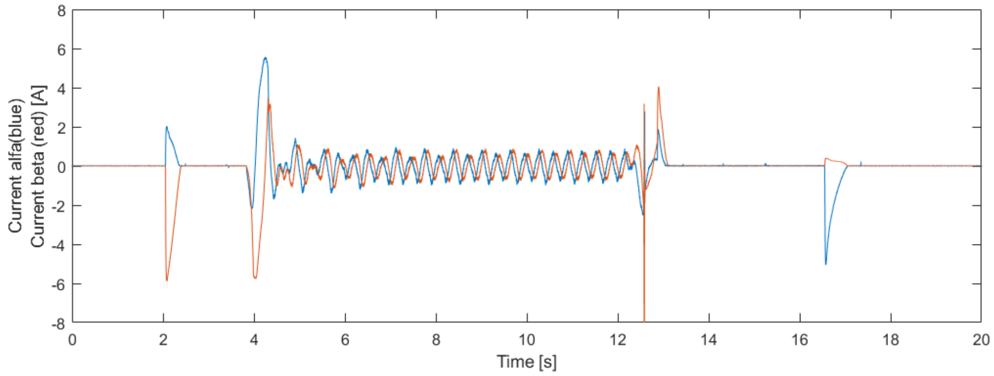

Fig. 116 Stator current alfa and stator current beta, test 1

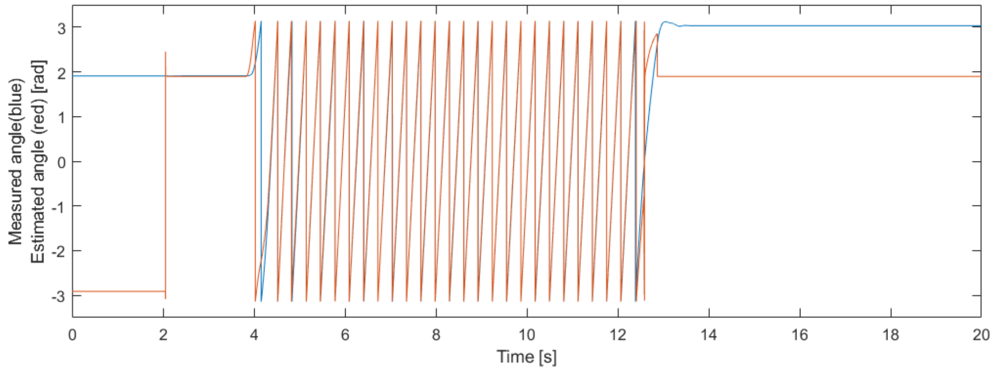

Fig. 117 Measured angle and estimated angle, test 1

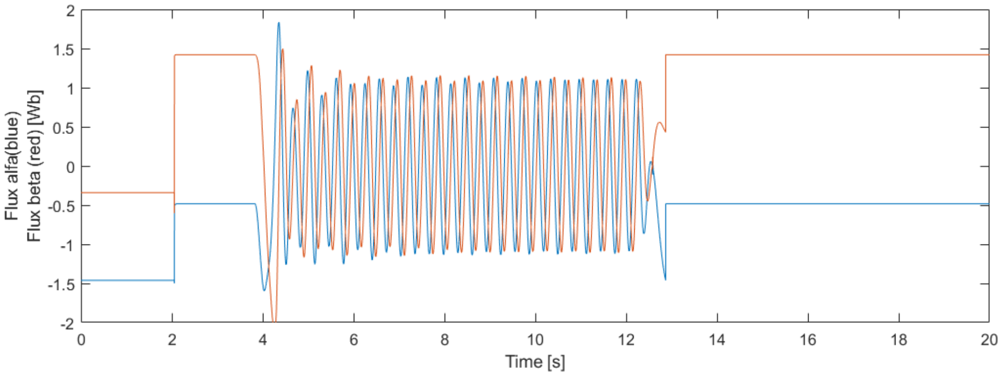

Fig. 118 Stator flux alfa and stator flux beta, test 1

6.2.2 Test 2

Machine excitation (rotor voltage step variation), machine starting to 50 rad/s (33% of the rated speed) and deceleration to standstill.
The motor is fluxed at about 2s and the initial rotor angle estimation algorithm is carried out. For this reason one can note the step variation in the estimated angle (Fig. 121) and in the stator flux (Fig. 122). The motor starts at about 4s.

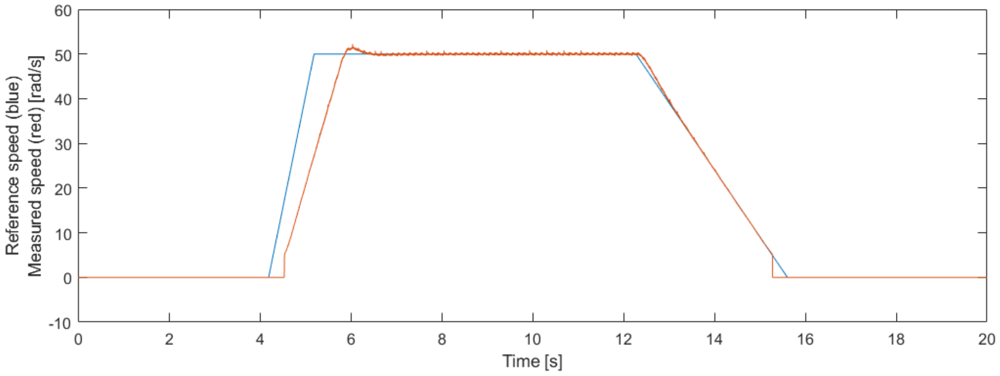

Fig. 119 Reference speed and measured speed, test 2

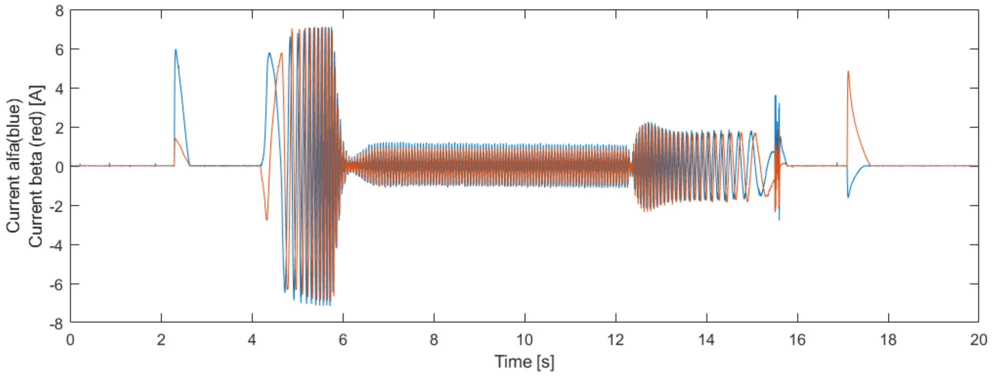

Fig. 120 Stator current alfa and stator current beta, test 2

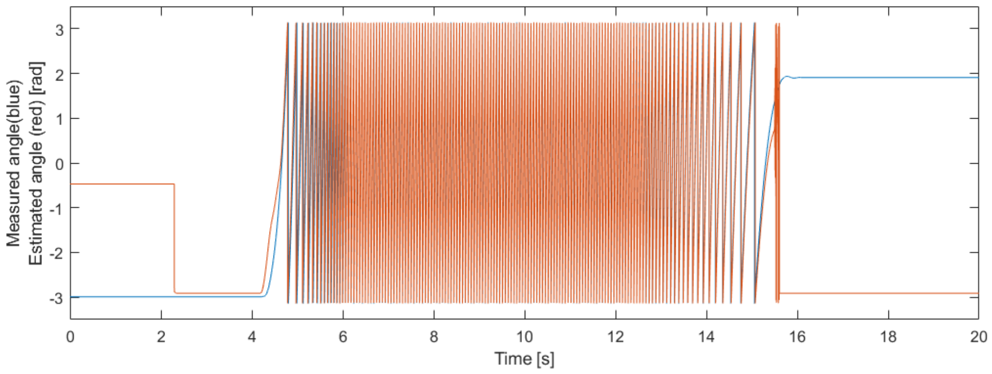

Fig. 121 Measured angle and estimated angle, test 2

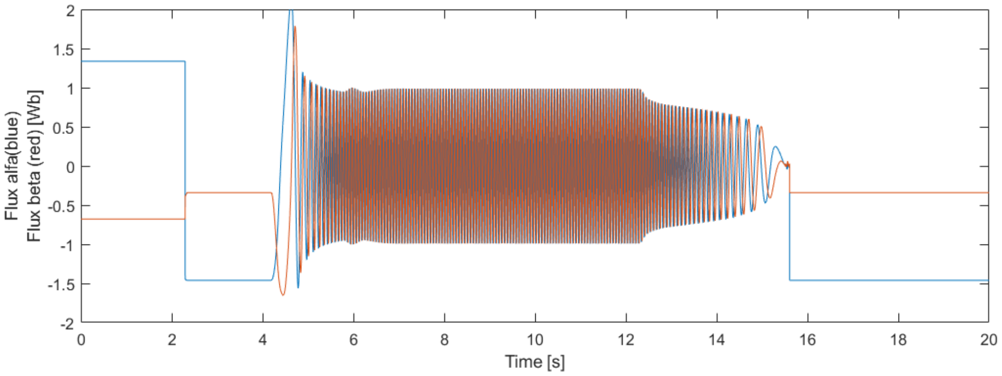

Fig. 122 Stator flux alfa and stator flux beta, test 1

6.2.3 Test 3

Machine excitation (rotor voltage step variation), machine starting to 150 rad/s (150% of the rated speed). The motor is fluxed at about 2s and the initial rotor angle estimation algorithm is carried out. For this reason one can note the step variation in the estimated angle (Fig. 125) and in the stator flux (Fig. 126). The motor starts at about 4s.

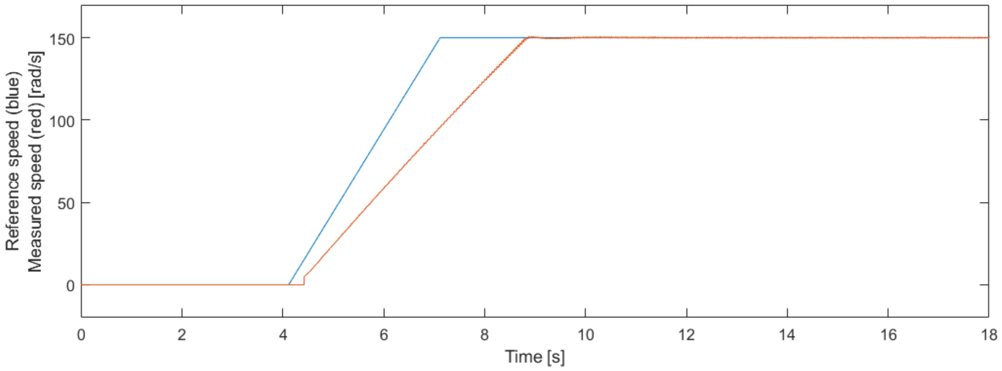

Fig. 123 Reference speed and measured speed, test 3

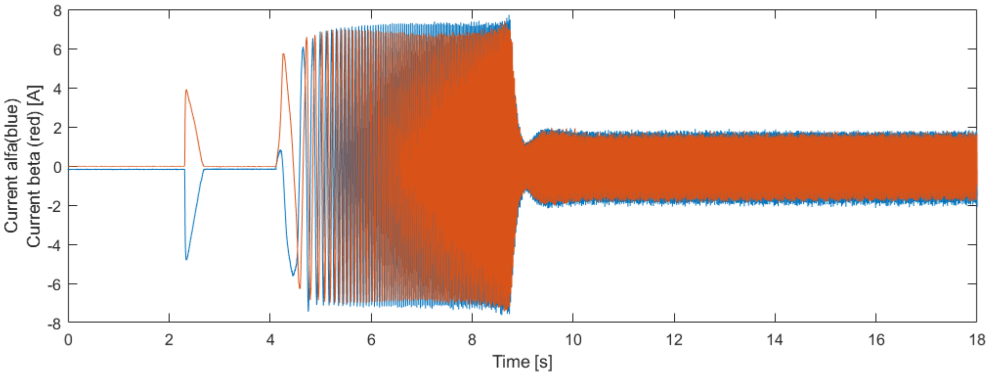

Fig. 124 Stator current alfa and stator current beta, test 3

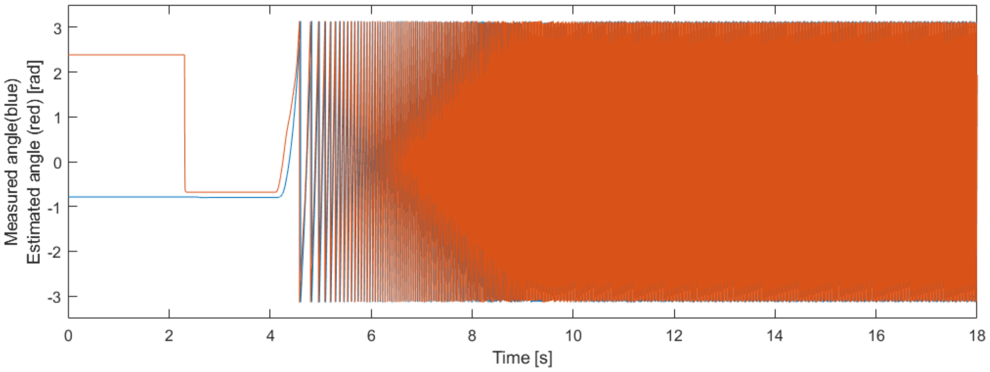

Fig. 125 Measured angle and estimated angle, test 3

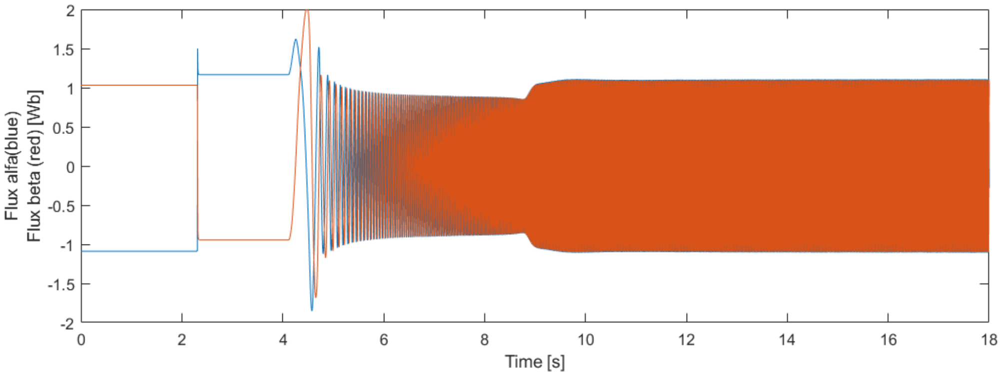

Fig. 126 Stator flux alfa and stator flux beta, test 3

6.2.4 Test 4

The purpose of this test is to evaluate the effectiveness of the initial rotor angle identification. For this reason the motor was fluxed several times, moving the rotor at each time and measuring the rotor angle error during each identification phase. The results of this test are reported in Table 15, whereas the angle plot is shown in Fig. 127. Please note that before the test starts the motor was moved in order to reset the encoder zero position.

Table 15 Test 4 results

Excitation starting time	Rotor angle	Estimation error
2.1s	53°	11°
8.8s	-121°	-19°
14.5s	-11°	7.4°
21.4s	-120°	-6.8°
27s	134°	-13°
32.5s	29°	-0.6°
37.7	-96°	-6.3°

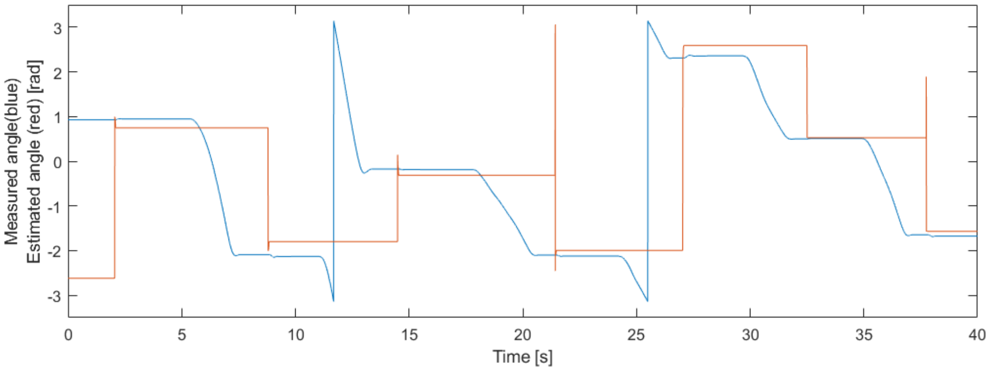

Fig. 127 Measured and estimated angle, test 4

6.2.5 Comments on EESM experimental results

Although with the proposed EESM test bench it was possible only to perform preliminary tests, the results reported in this section show the effectiveness of the proposed algorithm.

As a matter of facts, the motor was able to start and accelerate with the maximum stator current (6 A peak-value, i.e., 4.2 A rms-value). Since the initial rotor position was estimated precisely by the algorithm, the motor started without oscillations.

The initial rotor angle error was always below 19°, as it can be noticed from Test 4.

7 Conclusions and future developments

In this thesis, an in-depth study on sensorless passive algorithms for SPMSM and EESM was carried out.

Even if SPMSM and EESM are significantly different from a constructive point of view, they have in common the facts that sensorless active methods can hardly be exploited. Therefore, it is of fundamental importance to define robust sensorless passive algorithms that could work in all the speed range and with different torque profiles.

At first, four different sensorless passive algorithms, selected between the most promising ones available in the technical literature, were taken into account. These algorithms include a Enhanced Linear Active Disturbance Rejection Controller” (ELADRC), a Sliding Mode Observer with the adoption of a “Frequency-Adaptive Complex-Coefficient Filter” (SMO-FACCF), a Rotor Flux Observer based on the descend gradient method (RFO) and its extension to motors with rotor anisotropy (Extended-RFO).

The four algorithms were tested on the same test bench with different torque profiles and with different parameter uncertainties. Above the four selected algorithms, the RFO was the most performing one.

For the RFO, additional tests were carried out. In particular, the proposed sensorless algorithm was able to work from about 2% of the rated speed to the rated speed, starting the motor with different type of load (no-load, linear torque, quadratic torque and constant torque). Moreover, an air compressor was coupled to the motor, which is a significantly demanding load; indeed, it is characterized by rated torque at standstill and, in addition, the torque is highly intermittent. In all the working conditions the algorithm showed a great behaviour. In addition to that, an analytical stability analysis was carried out, in order to determine a priori the optimal observer gain values.

Furtherly, a novel technique, which modified the d-axis reference current during decelerations, improved the motor behaviour during fast transitions from high speed to low speed and during speed inversions.

Finally, a self-commissioning technique was proposed. The robustness of the sensorless algorithm towards motor parameter variations was investigated experimentally. The maximum allowed parameter variations were compared with the self-commissioning technique estimation error, in order to validate the algorithm.

After the positive tests on SPMSM, the sensorless algorithm was extended to EESM. In EESM, differently from PMSM, the angle between the α-axis and the stator flux is usually used to implement the FOC. In order to obtain the estimation of the stator flux, the voltage drop on the stator winding inductance was neglected. Moreover, a technique to estimate rotor initial position at standstill, without injecting high frequency current, was shown.

The obtained observer was used to perform various simulations on a 13.8 MW EESM. The motor model, provided by Nidec ASI, was validated in several years of experience in high-power applications.

The observer showed very interesting results via simulations and it was therefore decided to perform experimental tests on a small scale prototype in the Petra Lab of the University of Genova.

The preliminary tests showed a good behaviour of the proposed algorithm, including the definition of the initial rotor position. With the EESM test bench only no-load tests were carried out.

In the future, a more specific test bench for EESM will be developed and, in addition, higher power tests will be performed in Nidec ASI laboratories . The aim of future works will be to test the EESM sensorless control with different torque profile and in all speed working range, analogously to the tests carried out for the SPMSM.

8 References

[1] G. Wang, M. Valla, and J. Solsona, "Position Sensorless Permanent Magnet Synchronous Machine Drives—A Review," *IEEE Transactions on Industrial Electronics,* vol. 67, no. 7, pp. 5830-5842, 2020.

[2] M. Carpaneto, G. Maragliano, M. Marchesoni, and L. Vaccaro, "A new sensorless permanent magnet synchronous motor algorithm based on algebraic method," in *2009 13th European Conference on Power Electronics and Applications, EPE '09*, Barcellona, Spain, 2009.

[3] A. Formentini, G. Maragliano, M. Marchesoni, and L. Vaccaro, "A sensorless PMSM drive with inductance estimation based on FPGA," in *SPEEDAM 2012 - 21st International Symposium on Power Electronics, Electrical Drives, Automation and Motion*, 2012, pp. 1039-1044.

[4] R. Hosooka and S. Shinnaka, "New sensorless vector control of PMSM by discrete-time voltage injection of PWM carrier frequency - High-frequency current correlation method," in *Proceedings of the International Conference on Power Electronics and Drive Systems*, 2018, vol. 2017-December, pp. 913-918.

[5] J. Ji-Hoon, S. Seung-Ki, H. Jung-Ik, K. Ide, and M. Sawamura, "Sensorless drive of SMPM motor by high frequency signal injection," in *APEC. Seventeenth Annual IEEE Applied Power Electronics Conference and Exposition (Cat. No.02CH37335)*, 2002, vol. 1, pp. 279-285 vol.1.

[6] G. Wang, R. Liu, N. Zhao, D. Ding, and D. Xu, "Enhanced Linear ADRC Strategy for HF Pulse Voltage Signal Injection-Based Sensorless IPMSM Drives," *IEEE Transactions on Power Electronics,* Article vol. 34, no. 1, pp. 514-525, 2019, Art. no. 8310547.

[7] H. Zhang, W. Liu, Z. Chen, G. Luo, J. Liu, and D. Zhao, "Asymmetric Space Vector Modulation for PMSM Sensorless Drives Based on Square-Wave Voltage-Injection Method," *IEEE Transactions on Industry Applications,* Conference Paper vol. 54, no. 2, pp. 1425-1436, 2018.

[8] P. L. Xu and Z. Q. Zhu, "Carrier Signal Injection-Based Sensorless Control for Permanent-Magnet Synchronous Machine Drives Considering Machine Parameter Asymmetry," *IEEE Transactions on Industrial Electronics,* Article vol. 63, no. 5, pp. 2813-2824, 2016, Art. no. 7362210.

[9] Z. Q. Zhu and L. M. Gong, "Investigation of effectiveness of sensorless operation in carrier-signal-injection-based sensorless-control methods," *IEEE Transactions on Industrial Electronics,* Article vol. 58, no. 8, pp. 3431-3439, 2011, Art. no. 5587894.

[10] S. Y. Kim and I. J. Ha, "A new observer design method for HF signal injection sensorless control of IPMSMs," *IEEE Transactions on Industrial Electronics,* Article vol. 55, no. 6, pp. 2525-2529, 2008.

[11] A. Consoli, G. Scarcella, and A. Testa, "Industry application of zero-speed sensorless control techniques for PM synchronous motors," *IEEE Transactions on Industry Applications,* Article vol. 37, no. 2, pp. 513-521, 2001.

[12] S. Kim, J. Im, E. Song, and R. Kim, "A New Rotor Position Estimation Method of IPMSM Using All-Pass Filter on High-Frequency Rotating Voltage Signal Injection," *IEEE Transactions on Industrial Electronics,* vol. 63, no. 10, pp. 6499-6509, 2016.

[13] L. Chen, G. Götting, S. Dietrich, and I. Hahn, "Self-Sensing Control of Permanent-Magnet Synchronous Machines With Multiple Saliencies Using Pulse-Voltage-Injection," *IEEE Transactions on Industry Applications,* vol. 52, no. 4, pp. 3480-3491, 2016.

[14] S. Medjmadj, D. Diallo, M. Mostefai, C. Delpha, and A. Arias, "PMSM Drive Position Estimation: Contribution to the High-Frequency Injection Voltage Selection Issue," *IEEE Transactions on Energy Conversion,* vol. 30, no. 1, pp. 349-358, 2015.

[15] F. Gabriel, F. D. Belie, X. Neyt, and P. Lataire, "High-Frequency Issues Using Rotating Voltage Injections Intended For Position Self-Sensing," *IEEE Transactions on Industrial Electronics,* vol. 60, no. 12, pp. 5447-5457, 2013.

[16] D. Basic, F. Malrait, and P. Rouchon, "Current Controller for Low-Frequency Signal Injection and Rotor Flux Position Tracking at Low Speeds," *IEEE Transactions on Industrial Electronics,* vol. 58, no. 9, pp. 4010-4022, 2011.

[17] D. Raca, P. Garcia, D. D. Reigosa, F. Briz, and R. D. Lorenz, "Carrier-Signal Selection for Sensorless Control of PM Synchronous Machines at Zero and Very Low Speeds," *IEEE Transactions on Industry Applications,* vol. 46, no. 1, pp. 167-178, 2010.

[18] D. Raca, M. C. Harke, and R. D. Lorenz, "Robust Magnet Polarity Estimation for Initialization of PM Synchronous Machines With Near-Zero Saliency," *IEEE Transactions on Industry Applications,* vol. 44, no. 4, pp. 1199-1209, 2008.

[19] M. J. Corley and R. D. Lorenz, "Rotor position and velocity estimation for a salient-pole permanent magnet synchronous machine at standstill and high speeds," *IEEE Transactions on Industry Applications,* vol. 34, no. 4, pp. 784-789, 1998.

[20] A. H. Almarhoon, Z. Q. Zhu, and P. Xu, "Improved Rotor Position Estimation Accuracy by Rotating Carrier Signal Injection Utilizing Zero-Sequence Carrier Voltage for Dual Three-Phase PMSM," *IEEE Transactions on Industrial Electronics*, vol. 64, no. 6, pp. 4454-4462, 2017.

[21] X. Zhang, H. Li, S. Yang, and M. Ma, "Improved Initial Rotor Position Estimation for PMSM Drives Based on HF Pulsating Voltage Signal Injection," *IEEE Transactions on Industrial Electronics*, vol. 65, no. 6, pp. 4702-4713, 2018.

[22] G. Zhang, G. Wang, H. Wang, D. Xiao, L. Li, and D. Xu, "Pseudorandom-Frequency Sinusoidal Injection Based Sensorless IPMSM Drives With Tolerance for System Delays," *IEEE Transactions on Power Electronics*, vol. 34, no. 4, pp. 3623-3632, 2019.

[23] Q. Tang, A. Shen, X. Luo, and J. Xu, "PMSM Sensorless Control by Injecting HF Pulsating Carrier Signal Into ABC Frame," *IEEE Transactions on Power Electronics*, vol. 32, no. 5, pp. 3767-3776, 2017.

[24] G. Wang, H. Zhou, N. Zhao, C. Li, and D. Xu, "Sensorless Control of IPMSM Drives Using a Pseudo-Random Phase-Switching Fixed-Frequency Signal Injection Scheme," *IEEE Transactions on Industrial Electronics*, vol. 65, no. 10, pp. 7660-7671, 2018.

[25] G. Wang, D. Xiao, G. Zhang, C. Li, X. Zhang, and D. Xu, "Sensorless Control Scheme of IPMSMs Using HF Orthogonal Square-Wave Voltage Injection Into a Stationary Reference Frame," *IEEE Transactions on Power Electronics*, vol. 34, no. 3, pp. 2573-2584, 2019.

[26] C. Li, G. Wang, G. Zhang, D. Xu, and D. Xiao, "Saliency-Based Sensorless Control for SynRM Drives With Suppression of Position Estimation Error," *IEEE Transactions on Industrial Electronics*, vol. 66, no. 8, pp. 5839-5849, 2019.

[27] G. Wang, L. Yang, G. Zhang, X. Zhang, and D. Xu, "Comparative Investigation of Pseudorandom High-Frequency Signal Injection Schemes for Sensorless IPMSM Drives," *IEEE Transactions on Power Electronics*, vol. 32, no. 3, pp. 2123-2132, 2017.

[28] G. Wang, D. Xiao, N. Zhao, X. Zhang, W. Wang, and D. Xu, "Low-Frequency Pulse Voltage Injection Scheme-Based Sensorless Control of IPMSM Drives for Audible Noise Reduction," *IEEE Transactions on Industrial Electronics*, vol. 64, no. 11, pp. 8415-8426, 2017.

[29] R. Ni, D. Xu, F. Blaabjerg, K. Lu, G. Wang, and G. Zhang, "Square-Wave Voltage Injection Algorithm for PMSM Position Sensorless Control With High Robustness to Voltage Errors," *IEEE Transactions on Power Electronics*, vol. 32, no. 7, pp. 5425-5437, 2017.

[30] D. Kim, Y. Kwon, S. Sul, J. Kim, and R. Yu, "Suppression of Injection Voltage Disturbance for High-Frequency Square-Wave Injection Sensorless Drive With Regulation of Induced High-Frequency Current Ripple," *IEEE Transactions on Industry Applications*, vol. 52, no. 1, pp. 302-312, 2016.

[31] G. Wang, J. Kuang, N. Zhao, G. Zhang, and D. Xu, "Rotor Position Estimation of PMSM in Low-Speed Region and Standstill Using Zero-Voltage Vector Injection," *IEEE Transactions on Power Electronics*, vol. 33, no. 9, pp. 7948-7958, 2018.

[32] G. Xie, K. Lu, S. K. Dwivedi, R. J. Riber, and W. Wu, "Permanent Magnet Flux Online Estimation Based on Zero-Voltage Vector Injection Method," *IEEE Transactions on Power Electronics*, vol. 30, no. 12, pp. 6506-6509, 2015.

[33] G. Zhang, G. Wang, and D. Xu, "Saliency-based position sensorless control methods for PMSM drives - A review," *Chinese Journal of Electrical Engineering*, vol. 3, no. 2, pp. 14-23, 2017.

[34] L. M. Gong and Z. Q. Zhu, "Robust initial rotor position estimation of permanent magnet brushless AC machines with carrier signal injection-based sensorless control," in *2012 IEEE Energy Conversion Congress and Exposition (ECCE)*, 2012, pp. 2276-2283.

[35] Y. Li, Z. Q. Zhu, D. Howe, and C. M. Bingham, "Improved rotor position estimation in extended back-EMF based sensorless PM brushless AC drives with magnetic saliency," in *Proceedings of IEEE International Electric Machines and Drives Conference, IEMDC 2007*, 2007, vol. 1, pp. 214-219.

[36] S. Morimoto, K. Kawamoto, M. Sanada, and Y. Takeda, "Sensorless control strategy for salient-pole PMSM based on extended EMF in rotating reference frame," *IEEE Transactions on Industry Applications*, Article vol. 38, no. 4, pp. 1054-1061, 2002.

[37] S. Paitandi and M. Sengupta, "Design and implementation of sensorless vector control of surface mounted PMSM using back-EMF estimation and PLL based technique," in *2017 National Power Electronics Conference, NPEC 2017*, 2018, vol. 2018-January, pp. 129-134.

[38] C. Zhiqian, M. Tomita, S. Doki, and S. Okuma, "An extended electromotive force model for sensorless control of interior permanent-magnet synchronous motors," *IEEE Transactions on Industrial Electronics*, vol. 50, no. 2, pp. 288-295, 2003.

[39] M. Carpaneto, P. Fazio, M. Marchesoni, and G. Parodi, "Dynamic Performance Evaluation of Sensorless Permanent-Magnet Synchronous Motor Drives With Reduced Current Sensors," *IEEE Transactions on Industrial Electronics*, vol. 59, no. 12, pp. 4579-4589, 2012.

[40] S. Yang and G. Chen, "High-Speed Position-Sensorless Drive of Permanent-Magnet Machine Using Discrete-Time EMF Estimation," *IEEE Transactions on Industrial Electronics*, vol. 64, no. 6, pp. 4444-4453, 2017.

[41] J. Kim, I. Jeong, K. Nam, J. Yang, and T. Hwang, "Sensorless Control of PMSM in a High-Speed Region Considering Iron Loss," *IEEE Transactions on Industrial Electronics*, vol. 62, no. 10, pp. 6151-6159, 2015.

[42] F. Genduso, R. Miceli, C. Rando, and G. R. Galluzzo, "Back EMF Sensorless-Control Algorithm for High-Dynamic Performance PMSM," *IEEE Transactions on Industrial Electronics*, vol. 57, no. 6, pp. 2092-2100, 2010.

[43] S. Ye, "Fuzzy sliding mode observer with dual SOGI-FLL in sensorless control of PMSM drives," *ISA Transactions*, Article vol. 85, pp. 161-176, 2019.

[44] S. Chen, Y. Luo, and Y. Pi, "PMSM sensorless control with separate control strategies and smooth switch from low speed to high speed," *ISA Transactions*, Note vol. 58, pp. 650-658, 2015.

[45] Y. Chen, M. Li, Y. W. Gao, and Z. Y. Chen, "A sliding mode speed and position observer for a surface-mounted PMSM," *ISA Transactions*, Article vol. 87, pp. 17-27, 2019.

[46] C. L. Baratieri and H. Pinheiro, "New variable gain super-twisting sliding mode observer for sensorless vector control of nonsinusoidal back-EMF PMSM," *Control Engineering Practice*, vol. 52, pp. 59-69, 2016/07/01/ 2016.

[47] Y. Lee and S. Sul, "Model-Based Sensorless Control of an IPMSM With Enhanced Robustness Against Load Disturbances Based on Position and Speed Estimator Using a Speed Error," *IEEE Transactions on Industry Applications*, vol. 54, no. 2, pp. 1448-1459, 2018.

[48] G. Xiao, X. Wang, W. Tu, L. Tang, H. Zhang, and K. Yang, "A sensorless control of surface-mount permanent magnet synchronous motor based on rotor flux estimation," in *2017 20th International Conference on Electrical Machines and Systems (ICEMS)*, 2017, pp. 1-4.

[49] J. Lee, J. Hong, K. Nam, R. Ortega, L. Praly, and A. Astolfi, "Sensorless Control of Surface-Mount Permanent-Magnet Synchronous Motors Based on a Nonlinear Observer," *IEEE Transactions on Power Electronics*, vol. 25, no. 2, pp. 290-297, 2010.

[50] J. Choi, K. Nam, A. A. Bobtsov, A. Pyrkin, and R. Ortega, "Robust Adaptive Sensorless Control for Permanent-Magnet Synchronous Motors," *IEEE Transactions on Power Electronics*, vol. 32, no. 5, pp. 3989-3997, 2017.

[51] A. Khlaief, M. Bendjedia, M. Boussak, and M. Gossa, "A Nonlinear Observer for High-Performance Sensorless Speed Control of IPMSM Drive," *IEEE Transactions on Power Electronics*, vol. 27, no. 6, pp. 3028-3040, 2012.

[52] N. Henwood, J. Malaizé, and L. Praly, "A robust nonlinear Luenberger observer for the sensorless control of SM-PMSM: Rotor position and magnets flux estimation," in *IECON 2012 - 38th Annual Conference on IEEE Industrial Electronics Society*, 2012, pp. 1625-1630.

[53] M. Marchesoni, M. Passalacqua, L. Vaccaro, M. Calvini, and M. Venturini, "Performance improvement in a sensorless surface-mounted PMSM drive based on rotor flux observer," *Control Engineering Practice*, Article vol. 96, 2020, Art. no. 104276.

[54] M. Marchesoni, M. Passalacqua, L. Vaccaro, M. Calvini, and M. Venturini, "Low Speed Performance Improvement in a Self-Commissioned Sensorless PMSM Drive Based on Rotor Flux Observer," in *2019 21st European Conference on Power Electronics and Applications (EPE '19 ECCE Europe)*, 2019, pp. P.1-P.10.

[55] M. Marchesoni, M. Passalacqua, L. Vaccaro, M. Calvini, and M. Venturini, "An Improved Low-Noise Sensorless PMSM Drive able to Face Highly Intermittent Load Torque," in *2019 IEEE 10th International Symposium on Sensorless Control for Electrical Drives, SLED 2019*, 2019.

[56] Y. Zhao, Z. Zhang, W. Qiao, and L. Wu, "An Extended Flux Model-Based Rotor Position Estimator for Sensorless Control of Salient-Pole Permanent-Magnet Synchronous Machines," *IEEE Transactions on Power Electronics*, vol. 30, no. 8, pp. 4412-4422, 2015.

[57] T. Tuovinen, M. Hinkkanen, L. Harnefors, and J. Luomi, "Comparison of a Reduced-Order Observer and a Full-Order Observer for Sensorless Synchronous Motor Drives," *IEEE Transactions on Industry Applications*, vol. 48, no. 6, pp. 1959-1967, 2012.

[58] O. M. Arafa, G. A. Abdel Aziz, M. I. Abu El-Sebah, and A. A. Mansour, "Observer-based sensorless speed control of PMSM: A focus on drive's startup," *Journal of Electrical Systems and Information Technology*, vol. 3, no. 2, pp. 181-209, 2016/09/01/ 2016.

[59] S. Zossak, P. Sovicka, M. Sumega, and P. Rafajdus, "Evaluating Low Speed Limit of Back-EMF Observer for Permanent Magnet Synchronous Motor," *Transportation Research Procedia*, vol. 40, pp. 610-615, 2019/01/01/ 2019.

[60] D. Shah, G. Espinosa–Pérez, R. Ortega, and M. Hilairet, "Sensorless Speed Control of Non–salient Permanent Magnet Synchronous Motors," *IFAC Proceedings Volumes*, vol. 44, no. 1, pp. 11109-11114, 2011/01/01/ 2011.

[61] B. Du, S. Wu, S. Han, and S. Cui, "Application of Linear Active Disturbance Rejection Controller for Sensorless Control of Internal Permanent-Magnet Synchronous Motor," *IEEE Transactions on Industrial Electronics*, vol. 63, no. 5, pp. 3019-3027, 2016.

[62] L. Qu, W. Qiao, and L. Qu, "An Enhanced Linear Active Disturbance Rejection Rotor Position Sensorless Control for Permanent Magnet Synchronous Motors," *IEEE Transactions on Power Electronics*, vol. 35, no. 6, pp. 6175-6184, 2020.

[63] J. Jin-Su, B. Park, K. Tae-Sung, L. Dong Myung, and H. Dong-Seok, "Parallel reduced-order Extended Kalman Filter for PMSM sensorless drives," in *2008 34th Annual Conference of IEEE Industrial Electronics*, 2008, pp. 1326-1331.

[64] S. Bolognani, L. Tubiana, and M. Zigliotto, "Extended Kalman filter tuning in sensorless PMSM drives," *IEEE Transactions on Industry Applications*, vol. 39, no. 6, pp. 1741-1747, 2003.

[65] O. Aydogmus and S. Sünter, "Implementation of EKF based sensorless drive system using vector controlled PMSM fed by a matrix converter," *International Journal of Electrical Power & Energy Systems*, vol. 43, no. 1, pp. 736-743, 2012/12/01/ 2012.

[66] Z. Chen, L. Wang, and X. Liu, "Sensorless Direct Torque Control of PMSM using Unsected Kalman Filter*," *IFAC Proceedings Volumes*, vol. 44, no. 1, pp. 4380-4385, 2011/01/01/ 2011.

[67] N. K. Quang, N. T. Hieu, and Q. P. Ha, "FPGA-Based Sensorless PMSM Speed Control Using Reduced-Order Extended Kalman Filters," *IEEE Transactions on Industrial Electronics*, vol. 61, no. 12, pp. 6574-6582, 2014.

[68] S. Ye, "Design and performance analysis of an iterative flux sliding-mode observer for the sensorless control of PMSM drives," *ISA Transactions*, vol. 94, pp. 255-264, 2019/11/01/ 2019.

[69] S. Ye, "A novel fuzzy flux sliding-mode observer for the sensorless speed and position tracking of PMSMs," *Optik*, vol. 171, pp. 319-325, 2018/10/01/ 2018.

[70] S. Lin and W. Zhang, "An adaptive sliding-mode observer with a tangent function-based PLL structure for position sensorless PMSM drives," *International Journal of Electrical Power & Energy Systems*, vol. 88, pp. 63-74, 2017/06/01/ 2017.

[71] M. M. Gaballah, M. El Bardini, and M. Sharaf, "Chattering-free sliding mode observer for speed sensorless control of PMSM," *Applied Computing and Informatics*, vol. 13, no. 2, pp. 169-174, 2017/07/01/ 2017.

[72] Y. Zhang and V. Utkin, "Sliding mode observers for electric machines-an overview," in *IEEE 2002 28th Annual Conference of the Industrial Electronics Society. IECON 02*, 2002, vol. 3, pp. 1842-1847 vol.3.

[73] S. Chi, Z. Zhang, and L. Xu, "Sliding-Mode Sensorless Control of Direct-Drive PM Synchronous Motors for Washing Machine Applications," *IEEE Transactions on Industry Applications*, vol. 45, no. 2, pp. 582-590, 2009.

[74] H. Kim, J. Son, and J. Lee, "A High-Speed Sliding-Mode Observer for the Sensorless Speed Control of a PMSM," *IEEE Transactions on Industrial Electronics*, vol. 58, no. 9, pp. 4069-4077, 2011.

[75] Z. Qiao, T. Shi, Y. Wang, Y. Yan, C. Xia, and X. He, "New Sliding-Mode Observer for Position Sensorless Control of Permanent-Magnet Synchronous Motor," *IEEE Transactions on Industrial Electronics*, vol. 60, no. 2, pp. 710-719, 2013.

[76] D. Liang, J. Li, and R. Qu, "Sensorless Control of Permanent Magnet Synchronous Machine Based on Second-Order Sliding-Mode Observer With Online Resistance Estimation," *IEEE Transactions on Industry Applications*, vol. 53, no. 4, pp. 3672-3682, 2017.

[77] Q. An, J. Zhang, Q. An, X. Liu, A. Shamekov, and K. Bi, "Frequency-Adaptive Complex-Coefficient Filter-Based Enhanced Sliding Mode Observer for Sensorless Control of Permanent Magnet Synchronous Motor Drives," *IEEE Transactions on Industry Applications*, vol. 56, no. 1, pp. 335-343, 2020.

[78] A. Hosseyni, R. Trabelsi, M. F. Mimouni, A. Iqbal, and R. Alammari, "Sensorless sliding mode observer for a five-phase permanent magnet synchronous motor drive," *ISA Transactions*, vol. 58, pp. 462-473, 2015/09/01/ 2015.

[79] Y. Imaeda, S. Doki, M. Hasegawa, K. Matsui, M. Tomita, and T. Ohnuma, "PMSM position sensorless control with extended flux observer," in *IECON 2011 - 37th Annual Conference of the IEEE Industrial Electronics Society*, 2011, pp. 4721-4726.

[80] R. Ortega, L. Praly, A. Astolfi, J. Lee, and K. Nam, "Estimation of Rotor Position and Speed of Permanent Magnet Synchronous Motors With Guaranteed Stability," *IEEE Transactions on Control Systems Technology*, vol. 19, no. 3, pp. 601-614, 2011.

[81] A. A. Bobtsov, A. A. Pyrkin, R. Ortega, S. N. Vukosavic, A. M. Stankovic, and E. V. Panteley, "A robust globally convergent position observer for the permanent magnet synchronous motor," *Automatica*, Article vol. 61, pp. 47-54, 2015.

[82] J. Choi, K. Nam, A. A. Bobtsov, and R. Ortega, "Sensorless Control of IPMSM Based on Regression Model," *IEEE Transactions on Power Electronics*, vol. 34, no. 9, pp. 9191-9201, 2019.

[83] U. Rieder, M. Schroedl, and A. Ebner, "Sensorless control of an external rotor PMSM in the whole speed range including standstill using DC-link measurements only," in *2004 IEEE 35th Annual Power Electronics Specialists Conference (IEEE Cat. No.04CH37551)*, 2004, vol. 2, pp. 1280-1285 Vol.2.

[84] J. Lara, A. Chandra, and J. Xu, "Integration of HFSI and extended-EMF based techniques for PMSM sensorless control in HEV/EV applications," in *IECON 2012 - 38th Annual Conference on IEEE Industrial Electronics Society*, 2012, pp. 3688-3693.

[85] C. Silva, G. M. Asher, and M. Sumner, "Hybrid rotor position observer for wide speed-range sensorless PM motor drives including zero speed," *IEEE Transactions on Industrial Electronics*, vol. 53, no. 2, pp. 373-378, 2006.

[86] M. Seilmeier and B. Piepenbreier, "Sensorless Control of PMSM for the Whole Speed Range Using Two-Degree-of-Freedom Current Control and HF Test Current Injection for Low-Speed Range," *IEEE Transactions on Power Electronics*, vol. 30, no. 8, pp. 4394-4403, 2015.

[87] M. Fatu, R. Teodorescu, I. Boldea, G. Andreescu, and F. Blaabjerg, "I-F starting method with smooth transition to EMF based motion-sensorless vector control of PM synchronous motor/generator," in *2008 IEEE Power Electronics Specialists Conference*, 2008, pp. 1481-1487.

[88] H. Li, X. Zhang, S. Liu, and C. Xu, "Hybrid Sensorless Control Based on I/F and Sliding Mode Observer Using Current Nonlinear Regulation for PMSM Drives," in *2019 22nd International Conference on Electrical Machines and Systems (ICEMS)*, 2019, pp. 1-5.

[89] S. V. Nair, K. Hatua, N. D. Prasad, and D. K. Reddy, "A Smooth and Stable Open-Loop I-F Control for a Surface Mount PMSM Drive by Ensuring Controlled Starting Torque," in *IECON 2018 - 44th Annual Conference of the IEEE Industrial Electronics Society*, 2018, pp. 355-360.

[90] M. Wang, Y. Xu, J. Zou, and H. Lan, "An optimized I-F startup method for BEMF-based sensorless control of SPMSM," in *2017 IEEE Transportation Electrification Conference and Expo, Asia-Pacific (ITEC Asia-Pacific)*, 2017, pp. 1-6.

[91] J. Kou, Q. Gao, Y. Teng, J. Ye, and D. Xu, "An Envelope-Prediction-Based Sensorless Rotor Position Observation Scheme for LCI-Fed EESM at Zero and Low Speed," *IEEE Transactions on Power Electronics*, vol. 35, no. 7, pp. 7356-7365, 2020.

[92] J. Kou, Q. Gao, K. Xu, and D. Xu, "A Sensorless Rotor Position Estimation Method Based on the Field Current Harmonic for an LCI-Fed EESM," *IEEE Transactions on Industrial Electronics*, vol. 66, no. 4, pp. 2561-2569, 2019.

[93] Y. Zhou and S. Long, "Sensorless Direct Torque Control for Electrically Excited Synchronous Motor Based on Injecting High-Frequency Ripple Current Into Rotor Winding," *IEEE Transactions on Energy Conversion*, vol. 30, no. 1, pp. 246-253, 2015.

[94] H. B. Chung and R. Kennel, "PWM-based Sensorless Control of Electrically Excited Synchronous Machine Using Mutual Inductance," in *2020 International Symposium on Power Electronics, Electrical Drives, Automation and Motion (SPEEDAM)*, 2020, pp. 232-236.

[95] S. Feuersänger and M. Pacas, "Rotor position identification in synchronous machines by using the excitation machine as a sensor," in *2016 IEEE Symposium on Sensorless Control for Electrical Drives (SLED)*, 2016, pp. 1-6.

[96] M. Koteich, A. Messali, and S. Daurelle, "Self-sensing control of the externally-excited synchronous machine for electric vehicle traction application," in *2017 IEEE International Symposium on Sensorless Control for Electrical Drives (SLED)*, 2017, pp. 91-96.

[97] C. Jongwon, J. Ilsu, N. Kwanghee, and J. Sungyoon, "Sensorless control for electrically energized synchronous motor based on signal injection to field winding," in *IECON 2013 - 39th Annual Conference of the IEEE Industrial Electronics Society*, 2013, pp. 3120-3129.

[98] P. Dai, Y. Lv, N. Xu, and H. Xie, "Speed sensorless control of electrically excited synchronous motor based on the reduce-order state observer flux observation," in *2016 IEEE 11th Conference on Industrial Electronics and Applications (ICIEA)*, 2016, pp. 2009-2014.

[99] Y. Park and S. Sul, "A Novel Method Utilizing Trapezoidal Voltage to Compensate for Inverter Nonlinearity," *IEEE Transactions on Power Electronics*, vol. 27, no. 12, pp. 4837-4846, 2012.

[100] G. Wang *et al.*, "Self-Commissioning of Permanent Magnet Synchronous Machine Drives at Standstill Considering Inverter Nonlinearities," *IEEE Transactions on Power Electronics*, vol. 29, no. 12, pp. 6615-6627, 2014.

[101] M. Fadel, S. Caux, G. Borghetti, and G. Postiglione, "Sensorless Starting of Wound Rotor Synchronous Machines," in *2019 21st European Conference on Power Electronics and Applications (EPE '19 ECCE Europe)*, 2019, pp. P.1-P.6.